Dipl.-Ing. Herbert Hackl, BSc

On the Simulation of Radiated Emission of Integrated Circuits According the CISPR 25 ALSE Test

DISSERTATION

zur Erlangung des akademischen Grades

Doktor der technischen Wissenschaften

eingereicht an der

Technischen Universität Graz

Betreuer

Univ.-Prof. Dipl.-Ing. Dr.techn. Bernd Deutschmann
Institut für Elektronik

Zweitgutachter

Prof. Dr.-Ing. Stephan Frei
Technische Universität Dortmund

Graz, April 2019

EIDESSTATTLICHE ERKLÄRUNG

AFFIDAVIT

Ich erkläre an Eides statt, dass ich die vorliegende Arbeit selbstständig verfasst, andere als die angegebenen Quellen/Hilfsmittel nicht benutzt, und die den benutzten Quellen wörtlich und inhaltlich entnommenen Stellen als solche kenntlich gemacht habe. Das in TUGRAZonline hochgeladene Textdokument ist mit der vorliegenden Dissertation identisch.

I declare that I have authored this thesis independently, that I have not used other than the declared sources/resources, and that I have explicitly indicated all material which has been quoted either literally or by content from the sources used. The text document uploaded to TUGRAZonline is identical to the present doctoral dissertation.

Datum / Date

Unterschrift / Signature

Acknowledgments

The results presented in this thesis were gathered during my employment at NXP Semiconductors Austria. Namely, I´m grateful to my managers Dennis Jeurissen, Bernhard Spieß and Robert Kofler for the opportunity to do research in this remarkable company. My position was partially financed from the project eRamp, which was co-funded by grants from ENIAC Joint Undertaking and from Austria, Germany, the Netherlands, Romania, Slovakia and the UK. Financial support by the Austrian Research Promotion Agency (FFG) under Grant Nr. 843743 is gratefully acknowledged.
I thank my supervisor from the Institute of Electronics of Graz University of Technology, Prof. Bernd Deutschmann, for providing my insights to the academic way of working, his constant motivation and his contributions to my scientific work.
Likewise I am indebted to my colleagues from the Institute of Electronics and from worldwide NXP for the good cooperation, shared experiences and many hours of valuable technical discussions.
Finally, I thank Prof. Dr.-Ing. Stephan Frei of TU Dortmund University for agreeing to being member of my graduation committee and for his valued review of my written work.

Kurzfassung

Elektromagnetische Verträglichkeit (EMV) von elektronischen Systemen bezeichnet das Vermögen unbeeinflusst von äußeren Störungen zu funktionieren, aber auch die Notwendigkeit andere elektrische Systeme und Komponenten im Betrieb nicht zu stören. Heutzutage ist EMV von elektrischen Komponenten ein entscheidender Verkaufsfaktor, denn Hersteller von Gesamtsystemen können es nicht riskieren störempfindliche oder störungsverursachende Komponenten einzusetzen. Daher sind Produzenten von integrierten Schaltkreisen (integrated circuit, IC) bemüht die elektromagnetischen Eigenschaften ihrer Produkte schon während der Konzeptphase zu evaluieren, vorzugsweise ohne Bedarf an Prototypen, sondern ausschließlich per Simulation. Jedoch sind die damit beauftragten Schaltungsentwickler zumeist wenig vertraut mit den anzuwenden Richtlinien und den EMV Tests die mit dem Endprodukt durchgeführt werden. Die existierenden Ansätze setzen aber häufig genau dieses Wissen voraus. Um EMV Simulationen dennoch effizient durchzuführen, benötigt es Konzepte und Modelle, welche die Komplexität auf das Notwendigste reduzieren und elektromagnetische Prozesse auf Schaltungsebene zugänglich machen. Motivation für diese Arbeit ist die Frage, ob es für Komponentenhersteller überhaupt möglich ist, Ergebnisse von EMV Tests, die am Gesamtsystem durchgeführt werden, vorherzusagen, insbesondere da Details zum System üblicherweise nicht bekannt sind. Für die Vermessung von Funkstörstrahlung (radiated emission, RE) ausgehend von Kabelbäumen im Automobil wird beispielsweise der absorber lined shielded enclosure (ALSE) Test angewendet, welcher im automobilen Standard CISPR 25 spezifiziert ist. Inhalt dieser Arbeit ist die wissenschaftliche Untersuchung und Beurteilung aller Effekte, welche sich auf das entsprechende Messergebnis auswirken, insbesondere für Frequenzen kleiner $30\,\mathrm{MHz}$, da diese für moderne niederfrequente Systeme wie kontaktloses Laden (wireless power charging, WLPC) oder schlüssellose Entriegelung (passive keyless entry & start, PKE, PEPS) besonders relevant sind. Ausgehend von grundlegenden elektrostatischen analytischen Betrachtungen wird der Einfluss von verschiedenen Parametern des tatsächlichen Testaufbaus auf das Messergebnis beleuchtet und Möglichkeiten zur Berücksichtigung in der Simulation diskutiert. Schließlich wird eine Faustformel abgeleitet, welche den Schaltungsentwickler befähigt, niederfrequente Abstrahlungen, welche von einer (integrierten) Schaltung verursacht werden würden, unmittelbar abzuschätzen. Zusätzlich wird ein in seiner Universalität neuartiges Simulationsmodell vorgestellt, das für den Einsatz während der Schaltungssimulation geeignet ist und Entwicklern einen Einblick in potentielle Koppelpfade bzw. Abstrahlungsmechanismen gibt. Das Modell bildet nicht nur die elektromagnetische Kopplung zwischen dem zu testenden Gerät bzw. Schaltung und der Empfangsantenne ab, sondern beinhaltet zusätzlich eine Option zur Nachbearbeitung des Simulationsergebnisses, welche die Arbeitsweise eines realen EMV-Funkstörempfängers nachempfindet. Erst dadurch können Simulationen direkt mit tatsächlichen Messergebnissen verglichen werden. Zu diesem Zweck werden außerdem mathematische Methoden aufgezeigt, mit deren Hilfe insbesondere die Emissionen aufgrund von Datenübertragungen besonders effizient ermittelt werden können. Dies hilft, Schaltungssimulationszeiten zu minimieren. Die präsentierten Ergebnisse werden mit einer Vielzahl von realen Messergebnissen, die mit verschiedensten wissenschaftli-

chen und doch praxisnahen Versuchsaufbauten gewonnen wurden (durchgeführt im EMV Labor des Instituts für Elektronik der technischen Universität Graz), sowie 2D und 3D elektromagnetischen Simulationen gestützt. Um deren Praxistauglichkeit zu beweisen, werden sie an anwendungsnahen Beispielen demonstriert und mit herkömmlichen Methoden verglichen.

Abstract

Electromagnetic compatibility (EMC) of integrated circuits (ICs) is the capability to operate despite exterior disturbances (electromagnetic immunity) and at the same time to operate without disturbing other devices, hence to keep electromagnetic emissions low. Because modern electronic systems are getting more and more complex while being minimized in size, electromagnetic compatibility (EMC) of ICs takes on higher significance for competitiveness. IC manufacturers are increasingly interested in evaluating the EMC performance of new products as soon as during the very first design phase, best without the need of prototypes, i.e. by simulation only. Unfortunately, the IC designer in person is typically no EMC expert, not used to specialized tools for electromagnetic (EM) analysis and does often not know all details of the EMC tests which will be conducted on the final product. Though, most existing solutions for EMC simulation require this knowledge. To nonetheless enable efficient IC level simulation of system level EMC problems, novel methods and approaches are needed, which reduce the problem's complexity and make it accessible from within the native circuit design environment. A main scientific research question investigated in this thesis is whether and how component manufacturers can predict EMC test results of systems where their product is only a (small) part of, especially if parts of the overall system are unknown. Under consideration is the automotive absorber lined shielded enclosure (ALSE) test standardized by CISPR 25 that is used to evaluate the radiated emission (RE) of a cable harness attached to an IC. Objective of this work is the scientific investigation and assessment of effects on and contributors to the so captured RE for frequencies below $30\,\mathrm{MHz}$ which are relevant for e.g. wireless power charging (WLPC) or car access system (passive keyless entry (PKE) or passive entry passive start (PEPS)). Starting with fundamental electrostatic theory the influence of different parameters of the ALSE test setup on the emission reading are analytically derived and possibilities for consideration during circuit simulation are discussed. Eventually, a rule of thumb is deduced which enables the IC designer to very easily approximate the RE produced by a device. Additionally, an universal circuit level simulation model is developed with novel possibilities of adjustment to a certain ALSE setup. It highlights different propagation paths between device output and receiver antenna input and therewith helps to raise awareness of possible coupling mechanisms and consequences on RE. Furthermore, the model allows post-processing of the simulation data to display the emission reading in the way an electromagnetic interference (EMI) receiver does it. Only then simulation results can be directly compared to measurements. To minimize simulation times especially of data transmitting devices, mathematical approaches are presented which help to very efficiently depict the emission spectrum of data streams. All results are backed up with different scientific experiments and numerous real measurements (conducted in the EMC lab of the Institute of Electronics at Graz University of Technology), as well as 2D and 3D EM simulations. The useability of the introduced method is demonstrated with application-near examples and their performance is compared to existing solutions.

Contents

Abbreviations

ALSE absorber lined shielded enclosure

AM amplitude modulation

AN artificial network

AVG Average (detector of the EMI receiver)

BB broadband (signal)

BBS broadband SPICE

CA coherent attenuation

CM common-mode

CVP capacitive voltage probe

DFT discrete Fourier transformation

DM differential-mode

DUT device under test (IC mounted on PCB, if not otherwise stated)

ECBM equivalent cable bundle method

EM electromagnetic (field)

EMC electromagnetic compatibility

EMI electromagnetic interference

EUT equipment under test (DUT + cable harness + loads)

FFT fast Fourier transformation

IC integrated circuit

IF intermediate frequency (filter)

IIR1 infinite impulse response filter of first order

LF low frequency (used for frequencies below $3\,\mathrm{MHz}$)

MTL multiconductor transmission line

MW medium wave

NB narrowband (signal)

OATS open area test site

PCB printed circuit board

PEPS	passive entry passive start
PKE	passive keyless entry
PK	Peak (detector of the EMI receiver)
PRF	pulse repetition frequency
QP	Quasi-Peak (detector of the EMI receiver)
RBW	(frequency) resolution bandwidth
RE	radiated emission
STFT	short time Fourier transformation
TEM	transverse electromagnetic (mode propagation)
TF	transmission factor
TWP	twisted wire pair
WLPC	wireless power charging

1. Motivation and Research Questions

An IC manufacturer has full knowledge of the internal behavior of his device. The IC manufacturer's costumer, i.e. the system supplier knows how the system works which the IC is a (small) part of. When the system fails to meet the EMC requirements sometimes a specific IC can be identified to cause issues. To solve such problems, close cooperation between system and IC supplier and a lot of time is required. The motivation behind this thesis was to speed up such processes or even prevent them. The IC designer should be able to obtain system level EMC test results by simulation from within the native design environment. Therefore a good understanding of the 'exterior world', i.e. everything that is connected to the pins of the IC, is needed. Fig. 1.1 visualizes the main parts of a test setup to measure electromagnetic emissions. The DUT includes the IC mounted on a printed circuit board (PCB) and everything that is needed to operate it. The modeling and simulation of all parts of an IC, like e.g. transistors, die, bonding and package, as well as PCBs was scope of many other works before and will not be described in this work. The DUT is a black box sourcing a signal which is transmitted to the electromagnetic interference (EMI) receiver. Under consideration are the transmission path which describes how the output of the DUT is alternated by propagation to the input of the EMI receiver. Eventually, the IC designer needs both, a model of the transmission path and one of the EMI receiver, to predict the emission reading which yields the desired EMC test result.

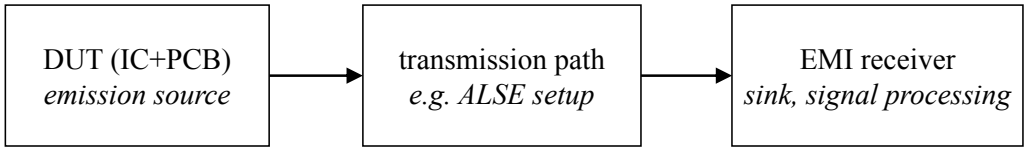

Figure 1.1.: Generalized schematic view of a test setup for electromagnetic emission: The device under test (DUT) is source of emissions which couple via a transmission path, e.g. radiated or conducted, to the EMI receiver which processes and visualizes the incoming disturbances. To assess the electromagnetic compliance of a device purely by simulation, models for all three blocks of this figure are needed.

Tests on electromagnetic emission can be distinguished into such by conducted or radiated means. This work deals with the later, namely radiated emission (RE) originating from long cable harnesses attached to the output of a DUT measured according the absorber lined shielded enclosure (ALSE) test specification given in the automotive CISPR 25 standard. The scientific research questions are:

1. For frequencies below $30\,\mathrm{MHz}$, is it possible to simulate the system level emission captured with the vertical rod antenna from component level view, without detailed knowledge of the overall system, specifically without proper definition of cable harness and ALSE?
2. How accurate could such a simulation be? What are the limiting factors?
3. What are the main radiation mechanisms and how does the ALSE test result relate to output quantities observable by the IC designer?

4. Speaking of data transmitting devices and extremely long transient test data streams, it is in many cases neither feasible nor necessary to simulate the complete transient IC output for EMC analysis. How can circuit simulation times be decreased? How are the outputs of the EMI receiver‘s Peak, Quasi-Peak and Average detectors affected by modifying the transmitted data stream?

Following introduction will present the state of the art regarding above research questions, as well as the middle and right block of Fig. 1.1 and introduce problems that will be given attention in the other chapters of this thesis.

2. Introduction

The electromagnetic compatibility (EMC) of integrated circuits (ICs) is nowadays of high significance for competitiveness. With increasing complexity of electronic systems and especially vehicles that tend to be more electric than mechanic, ICs need to withstand more electromagnetic distortions from the environment and emit less electromagnetic energy. Meeting the EMC requirements given by the system manufacturer is absolutely necessary to launch a new product. Providing better EMC performance than the competitors can be a critical selling point. As a consequence, IC manufacturers are increasingly interested in evaluating the EMC performance of their products as soon as during the very first product definition or design phase, without the need of prototypes. For this tools are needed that enable the circuit or IC designer to verify a design against EMC limits with as low effort as possible. Considering the segmentation as sketched in Fig. 1.1 and assuming that the designer is already capable of modeling and simulating the behavior of the IC itself in required detail, respective tools needed to describe the EMC test setup and the used measurement instrument(s) (i.e. the middle and right blocks of the figure).

The ALSE method (or ALSE test) is one of the component or module EMC test procedures defined in the automotive CISPR 25 standard [1]. Within an ALSE the radiated emission (RE) originating from a long cable harness connected to the device or equipment under test (DUT or EUT)[1] is captured with a receiver antenna and compared to standardized emission limits. The ALSE method is regarded as highly relevant to ensure that a component will not disturb other modules or on-board receivers in the final application, because in vehicles it is very common that modules are connected by long cables, which may act as sender antennas[2].
Although the ALSE test is termed a *component* test in the CISPR 25 standard it must not be mistaken with *IC component* test standards like IEC 61967 [2]. EMC tests for integrated circuits aim to characterize the IC itself with as less impact of the environment as possible. For this purpose evaluation setups are used that often do not reflect a typical use-case. The CISPR 25 standard on the other hand intends to evaluate the radio disturbance characteristics of a *system component* within a vehicle. The DUT can be a part of the vehicle electronics but also electrical motors or ignitions systems. During the measurement it needs to be operated in a typical configuration. In case of an IC this means that it should be mounted on the final application board (printed circuit board, PCB) together with all the application typical circuitry and it must drive a typical load. It should be noted at this point, that CISPR 25 assumes that the DUT and the load itself are not intentionally radiating.
Fig. 2.1 describes the properties of the ALSE test setup which are relevant for this work. The standard gives some recommendations for the test setup, but eventually it should represent the real application case. Actually, many vehicle and equipment manufacturers

[1] In this thesis DUT is used as short term for only the IC mounted on a PCB (similar to Fig. 2.1(a)), whereas the more general term EUT includes the DUT and also the complete equipment attached to it, like cable harness and load(s).

[2] Of course long cables may also act as receiver antennas. This is scope of radiated *immunity* tests, which are not covered in this work.

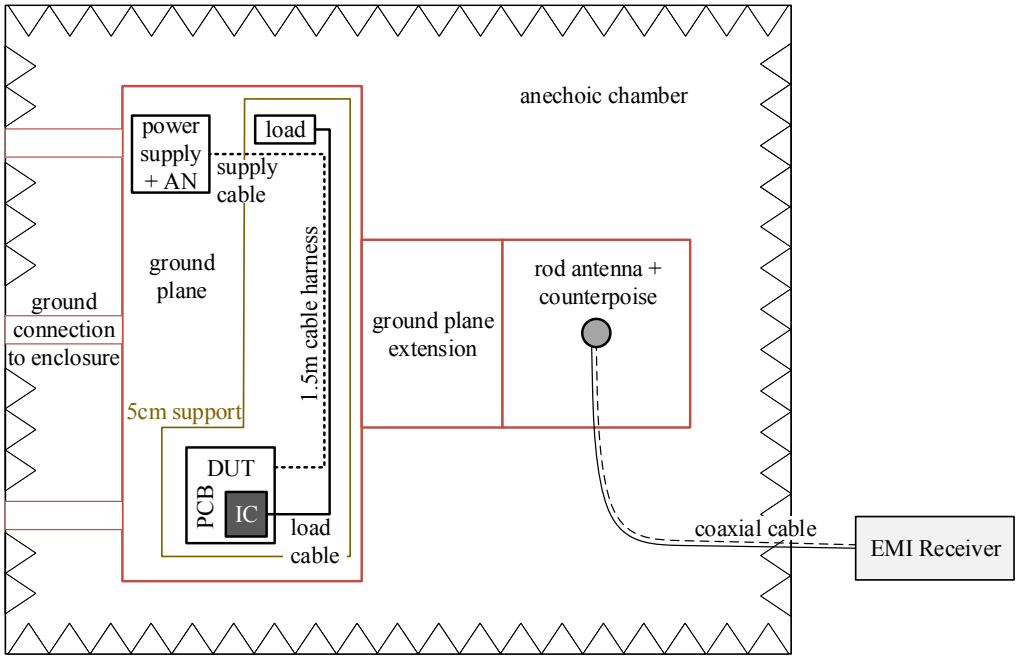

(a) Top view showing the composition of the cable harness. The power supply leads are connected to the power supply (often a car battery) through an artificial network (AN). This is a passive circuit providing a load impedance and supply isolation typical to the application. The ground plane extension should be as wide as the counterpoise.

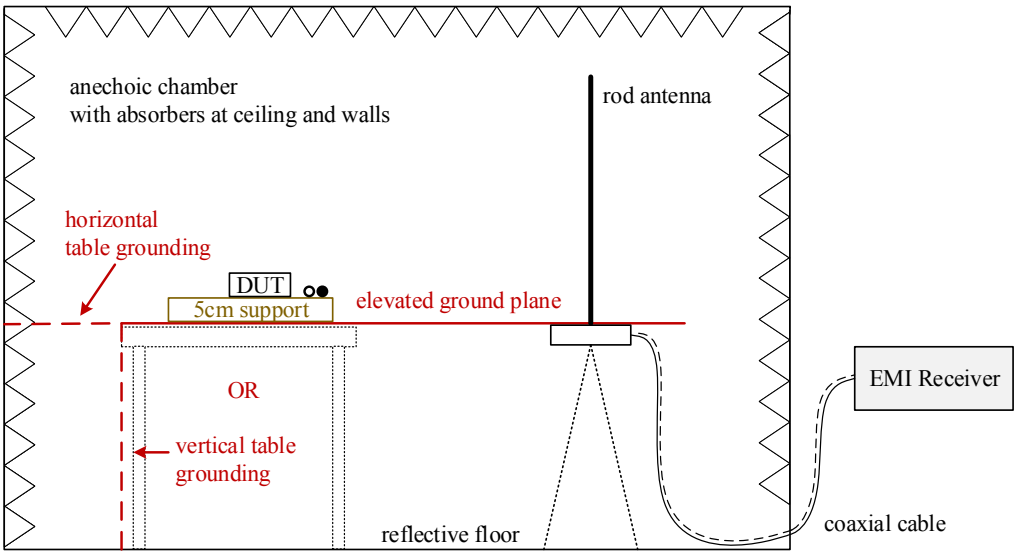

(b) Side view showing possible grounding schemes. The reference ground plane can be either horizontally or vertically bonded to the shielded enclosure. The length and the layout of the coaxial cable connecting the EMI receiver outside of the chamber is not defined. The cable may be non-supported resting on the chamber floor.

Figure 2.1.: Sketch of the ALSE test setup according CISPR 25 (simplified and not to scale). Depicted is the configuration for measurements from 150 kHz to 30 MHz where a 1 m vertical rod antenna is used to measure the electric field at 1 m distance from the harness. The DUT, the harness and the load are placed on a low permittivity support 5 cm above an elevated grounded plane.

prescribe a slightly different setup which might for instance differ in the allowed cable lengths. Commonly, radiated emission (RE) are measured from $150\,\mathrm{kHz}$ to $2.5\,\mathrm{GHz}$. In dependance of the frequency range the use of different receiver antennas is recommended, so for instance a $1\,\mathrm{m}$ vertical monopole antenna (also termed rod antenna) for the lowest frequency band from $150\,\mathrm{kHz}$ to $30\,\mathrm{MHz}$ (CISPR Band B) or a biconical antenna for the range $30\,\mathrm{MHz}$ to $300\,\mathrm{MHz}$ (CISPR Band C). Although generally speaking the trend goes towards higher and higher frequencies, low-frequency applications are still widely used in the automotive sector, for instance by wireless (vehicle) power charging ($10\,\mathrm{kHz}$ to $600\,\mathrm{kHz}$ [3]) and car access systems (PKE or PEPS, typically operating at $125\,\mathrm{kHz}$ or $134\,\mathrm{kHz}$ [4, 5]). For those applications the dominant harmonic emissions are likely to exist in the medium wave (MW) radio band from $530\,\mathrm{kHz}$ to $1.8\,\mathrm{MHz}$ used for amplitude modulation (AM) radio broadcasting. Hence, emission limit violations observed when using the vertical rod antenna are the main concern.

The prediction of ALSE test results has been scope of numerous investigations over the last decades. That is also due to the fact that the military standard MIL-STD-461 [6] (and other standards) defines a measurement procedure for radiated emission which is very similar[3] to that of CISPR 25. Starting with the anechoic chamber the equipment needed to perform a certified test is often not available or expensive. Manufacturers want to minimize the time and money needed to verify if their products comply with the EMC requirements. Some approaches target to omit the need for an anechoic chamber and forecast the ALSE test results by measurements on a prototype in a simple shielded room, e.g. [7, 8]. Others forecast the radiated emission by simulation, using measured voltages or currents as input for the simulation models, e.g. [9]. And yet others want to totally avoid the need for a manufactured prototype by predicting the electromagnetic compliance already during the design phase, based on simulated near field [10] or harness voltages and/or currents, e.g. [11, 12, 13]. Scope of this thesis is the latter.
The approaches in literature to predict RE captured with the ALSE test by simulation can be categorized as below. Generally speaking, the majority of publications attend to frequencies higher than $30\,\mathrm{MHz}$.

(a) purely analytical models, e.g. [14] [15]
(b) pure (numerical) simulations of various complexity based on analytical models, e.g. [16], often featuring commercial 3D EM simulations software or hybrid approaches, e.g. [17] [11] [13] [18]
(c) implementations of a measured transfer function between EUT and receiver obtained on a real ALSE setup, e.g. [19]

[3] Publications describing the simulation of radiated emission or repeatability problems with MIL-STD-461E are generally also applicable to the CISPR 25 setup and often there is no difference made in literature published before 2007. For the measurement with the rod antenna, however, the release MIL-STD-461F (2007) superseding MIL-STD-461E (1999) describes a reworked setup where the rod counterpoise is solely grounded to the chamber floor via the coaxial cable shield, i.e. in contrast to the CISPR 25 setup the table ground plane is not extended towards the rod antenna!

(d) prediction of the field at the receiver's position by near-field measurement or simulation close to the harness, e.g. [11] [7] [10]
(e) equivalent circuit models that describe the coupling path(s) between EUT and receiver, e.g. [20] [21] [12] [8] [22]

Table 2.1 summarizes the pros and cons of the above simulation approaches from IC designer point of view, given that no prototype of the IC is available. The table does not consider simulation times, as those are very dependent on a specific software and algorithms. (There are publications for virtually each of the given approaches demonstrating smart procedures to minimize processing times.)

Table 2.1.: ALSE simulation approaches from IC designer point of view

Approach	Pros	Cons
analytic	comprehensible	post-processing only needs export of much data requires accurate simulation model
3D EM simulation	accurate nice pictures	post-processing only non-familiar tools software licenses
transfer function	familiar accurate broadband	result depends on solver engine hazardous for transient simulation non-physical black box
equivalent circuit	familiar physical meaning comprehensible	narrowband inaccurate

The analytical predictions mostly focus on the far field only and do not consider coupling effects in the near field. The Hertzian dipole model is applied, requiring data of the current distribution at the harness. To obtain such by simulation needs a precise harness model and a suitable testbench to extract all the data needed for the calculation in a post-processing step.
Besides analytical models, 3D EM simulators are often used to investigate EMC issues. Their accuracy and reliability is generally limited by the quality of the input data given to the solver. The detailed knowledge of the test setup that is crucial to run trustworthy simulations is usually incomplete. Furthermore, experience with the respective simulation tool and additional software licenses are required. The interface to the IC design environment (e.g. Cadence Virtuoso or Mentor Pyxis) typically has limitations (if one is provided at all). The IC designers in person are usually no EMC experts and therefore not used to the respective tools. To enable them to evaluate the EMC performance of a circuit, an approach is needed which can be operated from within the native circuit design environment. Useability is a major requirement. It should be possible to obtain the RE reading easily and fast.

Accordingly, only the last two listed approaches remain feasible.
A common way to include detailed information of dependencies between nodes (ports) is the use of network parameters, typically in form of scattering parameters (S-parameters). Those models can be extracted from (3D) EM simulations or from measurements on the real setup. They constitute a transfer function in frequency domain. For time domain transient simulations it is typically necessary to generate equivalent circuit models (e.g. Broad Band Spice, bbspice or BBS) which map the behaviour of the input data, but usually have no physical meaning. Unfortunately, depending on parameter pre-processing, fitting algorithms and circuit solvers (like Spice, Keysight ADS, versions of Cadence spectre) the same set of S-parameters can yield very different results. As a consequence, circuit designers often prefer lumped element circuits to S-parameter black boxes, although the latter offer better accuracy and a more complete picture of the real-world behaviour.
For the transient simulation of the ALSE RE at low frequencies (i.e. with the rod monopole antenna) equivalent circuits were presented already in 1988 by Dawson [20] and recently by Lafon [21], both applying transmission line theory, Schneider [8], who estimated the circuit component values, and Carobbi [22] who obtained it from 3D EM simulation. Also in this work a circuit model will be developed, because of the above mentioned disadvantages of S-parameter based models which limit their suitability for the universal use by designers working with a broad range of different design environments. However, equivalent circuit models depict - with reasonable model generation effort - only a small number of real-life effects. Understanding the spectral composition of ALSE test results is essential. As an introduction to the model generation process the impact of the measurement chamber itself is discussed in the following section.

2.1. ALSE Parameters Influencing the Radiated Emission

Measurements carried out in an open area test site (OATS) are the standardized way to capture the 'real' undisturbed radiated field of a device, as in an OATS no obstacles (but the receiver antenna) are in the vicinity of the DUT and other radiators are far enough to not affect the measured RE. As a consequence, OATS require a lot of space free from exterior electromagnetic fields, are therefore rare and expensive to use. As an alternative, RE measurements are conducted in an ALSE. The shielding keeps exterior fields out, while the absorbers (should) prevent reflections at the chamber walls and dampen cavity resonances. In the interior of an ALSE certified for standard-compliant RE measurements, a field propagation similar to that obtained by OATS reference measurements has to be guaranteed. However, the chamber itself and, above all, the specific test setup always influence the emission reading. Many publications raised issues regarding bad repeatability and comparability of measurements carried out in different certified ALSEs and furthermore the lax certification criteria for laboratories. Lafon [23] and Turnbull [24] named the main parameters influencing the test results below $30\,\mathrm{MHz}$ to be the ground connections of the

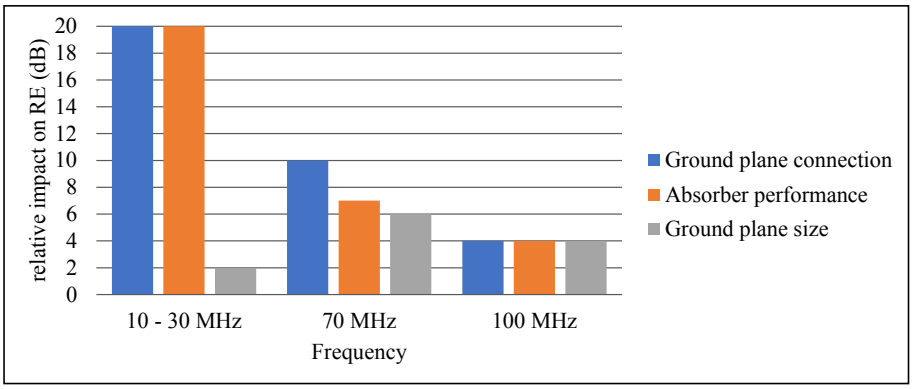

Figure 2.2.: Chamber and setup parameter's influence on ALSE test result over frequency according [23] and [1]. In [25] the influence of combined parameters was added.

elevated bench and the rod antenna counterpoise as well as the absorber's performance. A summary of Lafon's findings is illustrated by Fig. 2.2.

The new Edition 4 of the CISPR 25 standard [1] published in 2016 respects the claims for better comparability between chambers by introducing the proposals of Bongartz [26] and Turnbull [24]. Chamber calibration measurements below $30\,\mathrm{MHz}$ now have to be carried out with the emission source and rod receiver on the chamber floor. This approach effectively obviates all influences of the elevated test bench and therefor makes it easier to define and verify the compliance of the semi-anechoic chamber itself. The discussions regarding the 'correct' grounding scheme of the bench and the rod antenna counterpoise are prevented. A chamber is standard compliant if $90\,\%$ of calibration measurements points are within $\pm 6\,\mathrm{dB}$ of the reference data given in Annex J of CISPR 25 Ed.4.

Fig. 2.3 compares transmission factors (TFs) obtained with the complete test setup in two different compliant ALSEs and one simple shielded room. The transmission factor TF is defined as the ratio between voltage amplitude received by the measurement antenna A_{rec} and voltage amplitude at the cable harness A_{harness} (2.1).

$$\mathrm{TF} = \frac{A_{\mathrm{rec}}}{A_{\mathrm{harness}}} \tag{2.1}$$

The given TFs are extracted from results of capacitive voltage probe (CVP) measurements given in Jia's PHD thesis [27] and from measurements of the author. Jia demonstrated the impact of the elevated bench on the RE readings by placing the test setup directly on the chamber floor analog to the above described CISPR 25 chamber calibration procedure (with DUT, harness and load on a $5\,\mathrm{cm}$ support). The author of this work conducted measurements in a standard compliant ALSE, Fig. 2.4, and a shielded room without absorbers, Fig. 2.5. The graph in Fig. 2.3 illustrates three important points:
First, that measurements conducted on the chamber floor cannot be compared to such with elevated setups. The results obtained with the test setup on the chamber floor show an

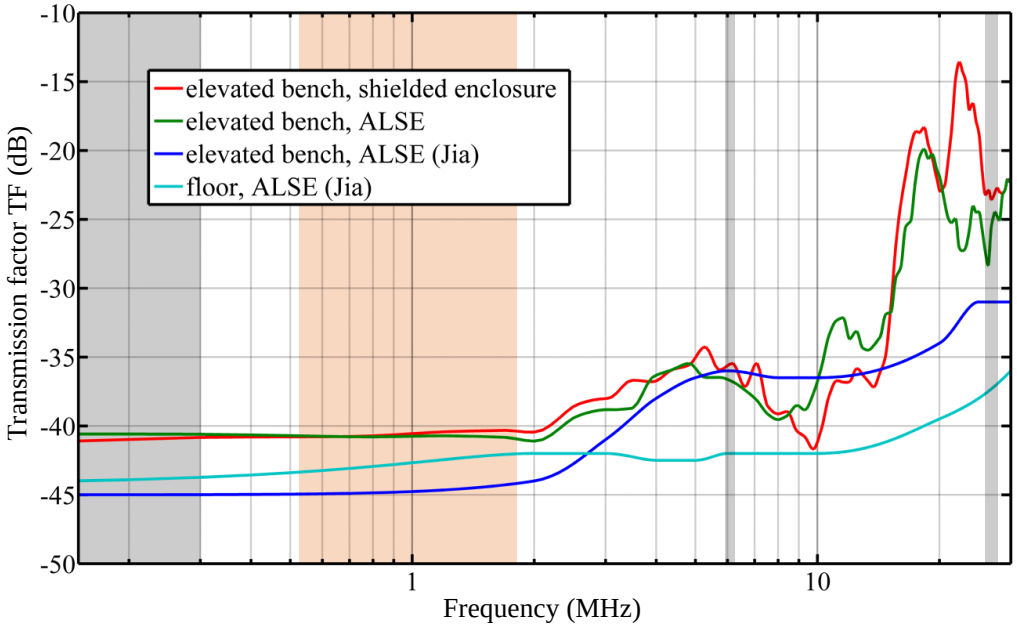

Figure 2.3.: The graph illustrates the impact of elevating the bench and the effectiveness of absorbers. For the colored frequency ranges RE limits are given by CISPR 25, but most automotive manufacturers regulate only the AM band from 520 kHz to 1.8 MHz. The first two curves (red, green) were derived from measurements using complete application setups where the harness included an additional power supply line (Fig. 2.4 and Fig. 2.5), while Jia's [27] harness was a single wire.

almost frequency independent transfer function between radiation source and rod antenna for frequencies up to 10 MHz, whereas the TF of the elevated setup changes drastically with frequency already above 2 MHz. In fact, it is clearly stated in Annex J of CISPR 25 Ed.4 that the elevated bench leads to RE measurement results that cannot be correlated to the reference data for chamber validation, meaning that the latter is not useable as reference result for RE compliance tests. Hence, the data published in the standard cannot be directly used to derive an ALSE test simulation model. Instead, results from an ALSE test featuring the actual test setup are needed.
Second, especially at higher frequencies there is a big difference between the two ALSE measurements (blue and green curves). However, this aligns with the data published in [28], where similar deviations can be observed.
Third, absorbers perform poorly at the low frequencies observed with the rod antenna. They may attenuate cavity resonances[4] but still the radiation characteristic are quite similar. The increasing radiation above 2 MHz is due to capacitive coupling between table and chamber floor and partly due to coupling between the chamber floor and the shield of the coaxial cable which connects to the EMI receiver outside of the chamber. Placing the test setup directly on the floor eliminates these parameters. This way the absorber performance

[4]In this figure it is one resonance at roughly 22 MHz. Generally, it is difficult to predict the number, frequencies and amplitudes of cavity resonances that would additionally appear due to missing absorbers.

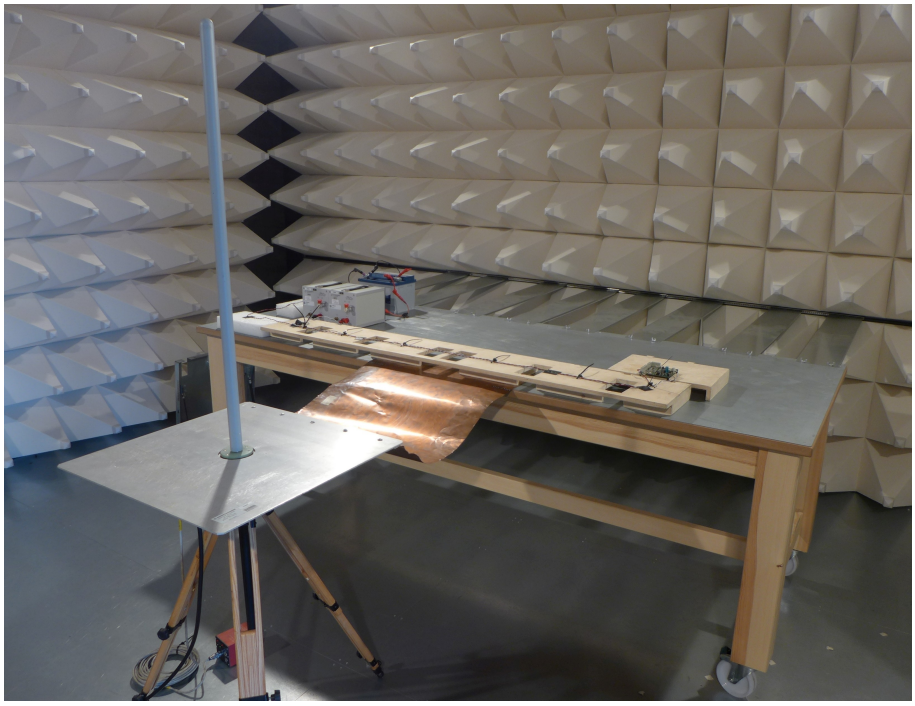

Figure 2.4.: Test setup in a certified ALSE used for the green curve of Fig. 2.3.

Figure 2.5.: Test setup in a non-certified shielded enclosure without absorbers used for the red curve of Fig. 2.3. The photo was taken in the EMC lab of the Institute for Electronics at Graz Universtiy of Technology were most of the experiments for this thesis were conducted.

can be observed better which allows stricter regulation, so that this impact factor (compare Fig. 2.2) should be minimized. Still the table grounding scheme, i.e. the impact of the elevated setup, is undefined. The related uncertainties and poor comparability between different test sites remain. Swanson [29] and [18] investigated by simulation the influence of the chamber and table size and various grounding and absorption schemes. It leads to the conclusion that above $10\,\mathrm{MHz}$ the accurate prediction of measurement results is not attainable. The referenced works consider the setups according MIL-STD-461E and F (which is similar to G) and CISPR 25.
Multiple resonances occur which correlate to the length and the position of the cable harness, the shape of the grounded bench and its extension and the size of the screened room. Goodwin and Marvin discussed their appearance and how to model it with lumped circuits already around 1990 [30] [31]. Absorber material can significantly reduce the amplitudes.

2.1.1. Counterpoise Connection Schemes

The counterpoise provides the ground potential reference for the measurement with the rod antenna, hence its connection to the chamber's ground (the reference potential for the EMI receiver) has significant impact on the E-field reading. Many authors published on the 'ideal' counterpoise connection and grounding scheme that should yield E-field measurement results which come as close as possible to the value of the undisturbed field observed in an OATS. Though, it is a controversial issue by itself which reading should be obtained with the ALSE test, specifically if the elevated ground plane and the distant, non-perfect grounding of the rod antenna's reference are allowed to alter the measurement result (the setup bears resemblance to the grounding concept in a vehicle) or not.
According the automotive CISPR 25 standard the rod antenna counterpoise was in all editions always connected to the table, i.e. the elevated bench, but in the MIL-STD-461 the counterpoise connection was subject to change. The current situation is, that the most recent Edition 4 of CISPR 25 (2016) specifies a table-connected counterpoise but the active MIL-STD-461G [32] (2015) requires an isolated counterpoise that is grounded via the shield of the coaxial cable to the chamber floor. Gandolfo *et al.* [33], Carobbi [22] and Uno *et al.* [18] very recently (2017 and 2018) discussed various counterpoise (and bench) connection schemes. The conclusion is, that setup related resonances can be eliminated with a directly grounded counterpoise which results in an TF being as good as constant up to $30\,\mathrm{MHz}$, and that a completely floating counterpoise would reduce the field readings by $10\,\mathrm{dB}$ to $20\,\mathrm{dB}$. This thesis focuses primarily on the default CISPR 25 ALSE test setup. However, the resulting model for RE simulation should be physically meaningful, thus it should also be able to reflect a change in the emission reading due to a deviating counterpoise potential. Therefore, in the last section of Chapter 4 the model will be verified against the measurement and 3D simulation results published in the referenced works.

2.1.2. Coaxial Cable Attached to the Antenna

There are some recent publications demonstrating that even below $30\,\mathrm{MHz}$ the coaxial cable which connects the receiver antenna to the measurement instrument (the EMI receiver) may notably influence the displayed RE reading. In the CISPR 25 standard the type and layout of this cable is not specified. In contrast, MIL-STD-461G [32] directs to use a ferrite sleeve around the coaxial cable to dampen possible oscillations and also specifies the cable layout for better repeatability and comparability of ALSE test results.
Carobbi and Izzo [34] showed that the cable layout determines the appearance of significant resonances around $15\,\mathrm{MHz}$ to $20\,\mathrm{MHz}$ and stated this was because of unwanted electric field below the counterpoise of the rod antenna. Zingarelli and Grego [35] observed that those resonances are due to capacitive coupling between the coax cable's shield and the chamber floor, which agrees with the experimental results of [34] but is a totally different explanation. For a $3\,\mathrm{m}$ coaxial cable, cable-induced resonances between $20\,\mathrm{MHz}$ to $30\,\mathrm{MHz}$ are reported in [35]. The longer the cable, the lower are respective frequencies. To mitigate this effect it is proposed to use a rod receiver antenna with optical interface like [36].
Uno *et al.* [18] conducted measurements with different types of rod antennas. They concluded, that especially if the potential of the antenna output is not isolated from the counterpoise,e.g. with a built-in isolating balun, the undefined additional ground connection established via the shield of the coaxial cable can cause significant deviations in the E-field reading above $10\,\mathrm{MHz}$, depending on the length of the cable and the way it is connected to ground.

2.2. Evolution of Simulation Models over Frequency

Now that the needs of an IC designer and the uncertainties of the ALSE test setup itself were discussed, this section will go into more detail on the development of a suitable simulation model. With increasing observation frequency the prediction of RE gets more and more complicated, hence the simulation model needs to imply respectively more details. The discussion is based on Fig. 2.6.

2.2.1. Frequencies Below $3\,\mathrm{MHz}$: Figure 2.6(a)

It was depicted by Fig. 2.3 of Section 2.1 (compare the light and dark blue traces) the elevation of the grounded bench has little impact of less than $3\,\mathrm{dB}$ below $3\,\mathrm{MHz}$. The offset between the two traces is due to the different sizes of the elevated ground plane and chamber floor. This factor will be further discussed in Section 3.4 of the next chapter. [24] and [37] confirm that the bench and counterpoise grounding do not impact RE at such low frequencies. Hence, to keep the simulation model as simple as possible, it is valid to assume a single global GND.

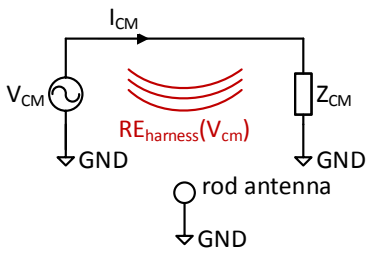

(a) Frequencies below 3 MHz: Capacitive coupling with global ground.

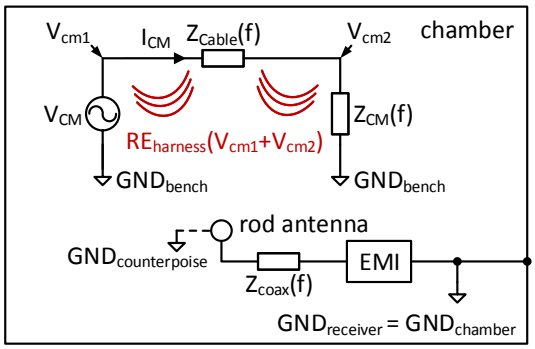

(b) Frequencies below 30 MHz: Capacitive coupling with distributed ground.

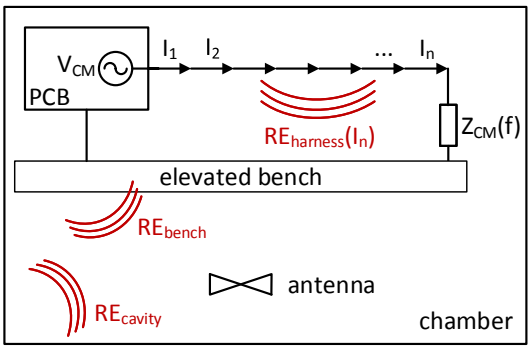

(c) Frequencies above 30 MHz: PCB affects the output signal. Radiation from distributed currents, elevated bench and cavity.

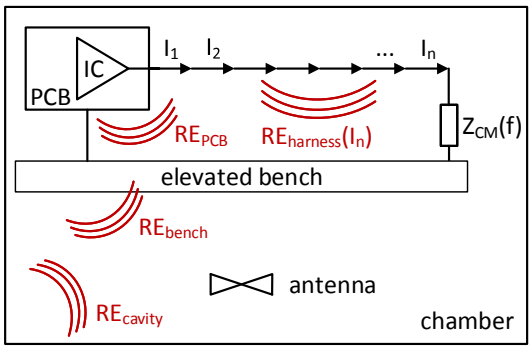

(d) Frequencies above 100 MHz: Respects IC model and additional radiation from PCB.

Figure 2.6.: Evolution of simulation model complexity over frequency

Already in 1989 Paul [38] compared the contributions of common-mode (CM) and differential-mode (DM) currents in a cable harness on it's radiated emissions and showed that the main source of radiation is the common-mode component. The radiated field components due to differential-mode currents would be canceled because they are in anti-phase, while the field components due to the common-mode currents would be superposed because they are in-phase. Jia [27] investigated by simulation that it is reasonable to ignore differential-mode radiation as long as the diameter of a cable bundle is less than 2 cm. It is therefore justified to replace an arbitrary (unshielded) cable harness with a single wire, sourced by the common-mode component of the cable signal only, as will be further discussed in section 2.3.1. The 'radiation' mechanism is capacitive coupling from the cable harness only. Electrostatic conditions can be assumed, i.e. the load and cable impedance are considered constant and CM voltage V_{CM} and current I_{CM} are related via Ohm's law. As long as the receiver antenna is terminated with high impedance (which it usually is), the transmission factor is frequency independent. In [39] it was shown that - assuming electrostatic conditions - computing RE based on the CM voltage or current yields similar results. There, a long dipole model was applied, i.e. the harness is replaced by a single long

current dipole. In practice, measuring CM currents of very low amplitude with high phase accuracy is difficult at very low frequencies [40]. Recently, it was presented in [41] that at very low frequencies (roughly below $0.1\,\mathrm{MHz}$ to $1\,\mathrm{MHz}$ in $1\,\mathrm{m}$ distance of a long wire) the calculation of the E-field using electric charges only excels measurement based calculations applying the multi dipole model.

2.2.2. Frequencies Between $3\,\mathrm{MHz}$ and $30\,\mathrm{MHz}$: Figure 2.6(b)

Roughly at $10\,\mathrm{MHz}$ another coupling mode becomes dominant over the direct capacitive coupling. It was termed transverse electromagnetic (TEM) mode coupling by Marvin and Goodwin [30]. The TEM mode propagates in the transmission line formed by the elevated conducting bench and its extension to the rod antenna counterpoise, and the walls of the screened room (the absorber lining becomes effective only at higher frequencies). This coupling mode is defined by the size of the chamber and the elevated bench. According [30] the characteristic impedance of the table sections can be used to model it. This approach will be followed in Chapter 4.2. Although the cable harness is still the sole source of radiation, secondary resonance effects need to be respected in the simulation model. The first cavity resonance typically appears at around $35\,\mathrm{MHz}$ [31] but might be lower for big chambers[5]. Of course the elevated ground plane within the room will tune this cavity resonance frequency. The coaxial cable which connects the receiver antenna to the measurement instrument (the EMI receiver) may introduce additional resonances. Some of the mentioned resonance effects might be attenuated by the use of absorbers but will not be completely eliminated (see Fig. 2.3), so it is necessary to respect all second-order resonances in the simulation model. This can be done by replacing the global GND with distributed GNDs and modeling the interfaces with lumped circuits. The $1.5\,\mathrm{m}$ cable harness itself was a perfect conductor in Fig. 2.6(a) but should be replaced by at least a simple circuit model to respect cable self-resonances which are typically in the range of $20\,\mathrm{MHz}$. The radiation captured by the receiver is a superposition of the DUT output signal and the signal on the far end of the harness.
In most publications RE is modeled by using the cable CM current, but Frei demonstrated in [42] that even for complex systems a quasi-static simulation featuring simple LC circuits yields accurate results for frequencies below $10\,\mathrm{MHz}$. In [43] he proposes to use a combination of capacitive CM voltage measurement (for low frequencies) and CM current measurements to obtain a substitution model of a cable harness valid for broad frequency ranges. Jia [27] states that below $10\,\mathrm{MHz}$ the cable-voltage based method yields better accuracy with higher reliability than the cable-current based predictions. Using a CVP he was able to correctly capture the cable-related resonances between $10\,\mathrm{MHz}$ and $20\,\mathrm{MHz}$. However, measurements and simulations based on capacitive voltage coupling are only

[5] The first cavity resonance frequency corresponds to the 'longest' wave that fits into the measurement chamber, hence is inverse proportional to the room diagonal D by $\lambda = c/D$. For a typical chamber size of $5.3\,\mathrm{m} \times 6.5\,\mathrm{m} \times 3.6\,\mathrm{m}$ this is $(3 \cdot 10^8\,\mathrm{m\,s^{-1}})/\sqrt{(5.3\,\mathrm{m})^2 + (6.5\,\mathrm{m})^2 + (3.6\,\mathrm{m})^2} = 33\,\mathrm{MHz}$ [25].

practicable in case of unshielded cables. For shielded cables it is better to predict the radiated emission based on distributed shield and ground currents, as done by Schneider in [8].

2.2.3. Frequencies Above 30 MHz: Figure 2.6(c)

At lower frequencies the IC was modeled as an independent CM voltage (or current) source. With increasing frequency it needs to be respected that the IC is part of an electronic system mounted on a PCB. The PCB is unlikely to radiate by itself yet, but the components surrounding the IC might effect the IC's output signal. Hence, accurate models of the PCB circuitry should be added to the simulation testbench.
It is no longer sufficient to consider the cable harness as only one or two emission sources. Instead, it is replaced by a number of distributed short dipole currents. The number of current dipoles is increasing with frequency.
Below 30 MHz ALSE measurements are conducted with a rod antenna, which captures mainly the electric field. At higher frequencies other antennas are used which capture both polarizations of the electromagnetic field. According to [27] the finiteness and shape of the ground plane is mostly affecting the horizontal polarization of E-field and that for frequencies above 30 MHz. Here it becomes necessary to respect the radiated field introduced by surface and edge currents in the ground plane. Higher order cavity resonances and multi-path reflections appear. The absorber performance plays a critical role. Simple equivalent circuit representations can poorly capture the complexity of the complete system. State of the art is to use 3D EM simulators or simulation models based on transfer function measurements of a real ALSE setup.

2.2.4. Frequencies Above 100 MHz: Figure 2.6(d)

At such high frequencies it needs to be considered if the PCB itself (current loops) or equipped components, like big inductors for DC/DC converters contribute directly to the RE reading. On IC level components like bond wires and package gain impact on the output signal and have to be respected in the IC model.
Even if all effects that the IC manufacturer has control of (transistors, padrings, bonding, package, IC grounding scheme, supply line distortions) are considered, the impact of system level parameters (PCB, cable harness type, EUT grounding scheme, surface currents) is likely to be dominant. In this frequency range IC level simulation of system level RE is as good as guessing and will hardly enable to reliably predict a pass or fail of emission limits.

2.3. Considering the Complete Cable Harness

2.3.1. Radiation Model for a Cable Bundle

Many publications deal with the analysis of multiconductor transmission lines (MTLs). Most present equivalent circuits for time- or frequency-domain simulation and consider (high-frequency) parameters like equivalent input impedance, reflection coefficients and crosstalk. The standard work is the book [44] by Paul. For the prediction of radiated emission originating from a cable bundle it is a common approach to replace the bundle with an equivalent single wire[6]. This approach is often termed the equivalent cable bundle method (ECBM).
It was already discussed, that for frequencies above $30\,\mathrm{MHz}$ RE is caused by CM currents. Already in 1996 Desheng [14] modeled the radiation of a multiconductor line by measuring the CM current with a current probe enclosing the complete cable bundle. The variation along the cable of the current phase as well as its amplitude need to be taken into account. The same measurement-based approach was used more recently in [40] for the ALSE method. In that contribution it is especially pointed out that the CM current based prediction of a cable's radiation is unsuitable for frequencies below $30\,\mathrm{MHz}$ because it is difficult to retrieve the correct current phase.
A more analytic contribution - again based on electric dipole currents and for electric fields above $30\,\mathrm{MHz}$ - is [46]. It is pointed out here, because the authors make the observation that the RE of a wire adjacent to a grounded wire is about half the RE of a single wire. They also state that the RE of a multiconductor line is less than the sum of RE of the same number of singularly considered conductors. This shielding effect of a MTL is argued to be because of opposite currents induced to nearby wires by crosstalk. The postulated shielding effect will be investigated in Chapter 3.5.2 but for very low frequencies and by electrostatic means, i.e. without the use of currents or mutual inductances. It will be shown that the (much simpler) consideration of static voltage potentials only leads to the same results.
When the near-field radiation of a cable bundle is calculated a single-wire equivalent can still be used but its exact dimension gets relevant. [48] is an extensive article which describes a procedure to obtain the equivalent's cross-section geometry and placement. In the very recent work [47] (2017) electric and magnetic field equivalent single wire radii for twisted wire pairs (TWPs) are derived and used to simulate radiated electric and magnetic fields above $10\,\mathrm{MHz}$ - again based on CM current distribution along the equivalent wire. The electric and magnetic equivalent radii are different due to the wire's dielectric coating. The method is illustrated by Fig. 2.7 on example of a TWP. This cable type is very common for automotive applications and is mostly used for the experiments presented in this thesis too. During the electrostatic calculation of the very near-field RE in Chapter 3 the ECBM will be applied to represent one or two TWPs by their single-wire equivalents. It will be derived how to choose the value of the equivalent radius to assure that the RE of an

[6] A single-wire equivalent can also be used to describe radiation induced effects, as presented in [45].

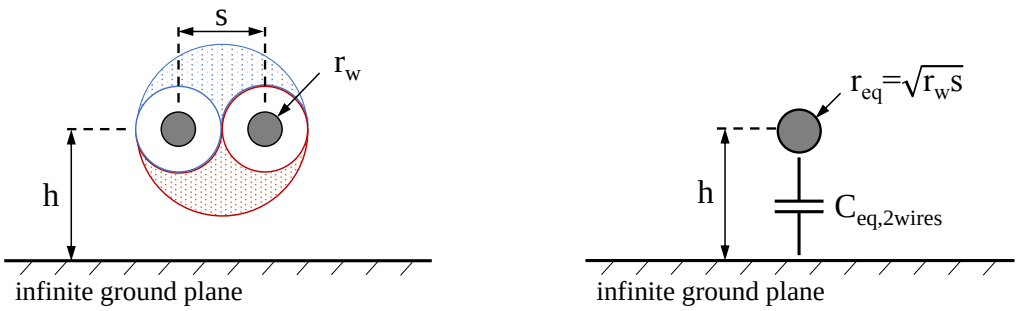

(a) A twisted pair cable in distance h above an infinite ground plane. Both conductors have radius r_w and are separated by s.

(b) The single-wire equivalent of the TWP has a radius of $r_{eq} = \sqrt{r_w s}$ [47] and an equivalent capacitance towards ground $C_{eq,2wires}$.

Figure 2.7.: For the ease of analytic discussion, a twisted pair cable is replaced with an equivalent single wire. In this work, the dielectric of the cable coating is neglected. The method will be used and further discussed in Chapter 3.5.1.

equivalent wire is linearly proportional to the CM *voltage* at the replaced cable bundle. The ECBM is a handy tool for the analytic discussion of RE. However, this method has its limitations when the radiated emission is a function of the position of a cable within a harness, as will be shown in Chapter 3.7.1.

2.3.2. Supply Line Radiation

CISPR 25 defines that the complete typical cable harness should be used during the evaluation of the radiated emission. This includes at least the power supply and GND lines, which the DUT needs for operation and at least one cable connecting the load. If multiple loads can be connected to the DUT, the harness may compromise more cables. A general case is depicted by Fig. 2.8.
In this thesis it is assumed that the load cable(s) directly connected to the output of an IC driver is the main source for the radiated emission measured with the ALSE test and that the radiation originating from the supply lines can be neglected. (This is often enough the case as long as an effective supply line filter is used.) This assumption is not to simplify the prediction of the harness' radiation. For the presented approach it does not matter what cable or how many cables contribute to the RE. The above assumption is rather applied because otherwise it is more difficult to predict the disturbing signal from IC level point of view. That is, because in most cases the IC is not directly powered with the supply voltage provided by the supply line (for instance 12 V from a car battery). The supply line input is first filtered and the supply voltage is regulated to the IC operating voltage. In order to simulate the distortions on the supply line produced by the operation of the EUT the current consumption profile of the complete circuitry connected to the supply line needs to be known and models describing the output-to-input coupling through the voltage

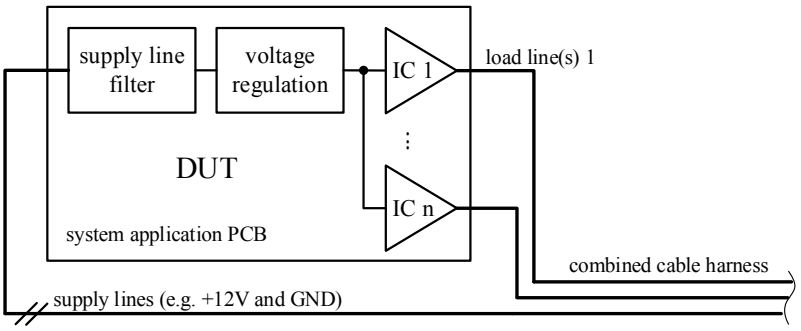

Figure 2.8.: The combined $1.5\,\mathrm{m}$ cable harness consists of supply and load lines. The latter are directly connected to an IC output so that their signal can be simulated well on IC level. Potential distortions on the supply line on the other hand are difficult to predict from IC level point of view due to the in-between regulation and filter circuits.

regulation circuit are necessary. The distortions coupling through the output stage of an IC on the other hand can usually be simulated with high accuracy. Especially if noisy grounds, bonding, package and PCB have negligible impact as is the case at low frequencies.

2.4. Short Summary and Orientation

Referring back to Fig. 1.1 of the Motivation chapter, till now the middle block of the overall emission problem, i.e. the transmission path from DUT output to EMI receiver input, was discussed. In short, it is feasible to include RE simulation to a circuit level model, at least for a limited frequency range. This eventually yields a simulated voltage amplitude at the receiver antenna's output node. This output is terminated by $50\,\Omega$, which is the input impedance of the EMI receiver. In order to be able to compare the simulated EMC test result, i.e. the emission spectrum of the receiver antenna output voltage, the IC or system designer needs to visualize the simulated spectrum in a similar way as the real measurement instrument. The next chapter introduces the topic of EMI receiver software modeling and points out special issues that will be further described in the last third of this thesis.

2.5. EMI Receiver Modeling

Inherent to all conventional circuit design environments is the discrete Fourier transformation (DFT), commonly implemented using the fast Fourier transformation (FFT) algorithm[7]. Hence it is the straightforward solution to compute frequency domain emission spectra

[7]The differentiation between FFT and DFT is irrelevant for this work. The more general term DFT will be used, although it is more likely that a circuit simulator actually processes a FFT.

from time domain simulation data. But electromagnetic emissions are measured with a kind of spectrum analyzer, a so-called Electromagnetic Interference Receiver (EMI receiver). The reading displayed by that instrument might differ from a DFT result, although for many signals the maximum amplitudes are equal. In general, a DFT is often sufficient to predict the EMI receiver's Peak (PK) detector reading. However, there are a cases where the emission spectrum prediction with a DFT fails. A DFT is intended for periodic signals only and by definition captures the spectral energy of one complete signal period. Its frequency resolution is a function of the number of processed time discrete samples, i.e. the period length and the sampling rate. In contrary, an EMI receiver applies a frequency selective input window of strictly defined bandwidth, compare Table 2.2, which makes its frequency resolution a signal independent constant. Modern, so-called time domain (TD) EMI receivers process the windowing directly on the transient input signal and employ a short time Fourier transformation (STFT).Details may be found in [49], in documentations of the instrument suppliers themselves [50] [51] [52] and of course by the defining CISPR 16-1-1 standard [53]. In order to display the radiated emission simulation result exactly like the real measurement hardware would do it[8], a software EMI receiver emulator is needed. Such were already presented by Hörmaier *et al.* [55], Karaca *et al.* [54] and Li *et al.* [56]. The latter focuses on the fact that a common DFT analysis is different from the windowed STFT processed by the EMI receiver.
The following subsections introduce issues that will be discussed in more detail in Chapter 5 of this work.

2.5.1. Emission Spectrum of Broadband Signals

The understanding of the terms *narrowband* (NB) and *broadband* (BB) varies for different technical fields. For this work it is convenient to define them with respect to the frequency resolution bandwidth (RBW) of an EMI receiver, which is the $-6\,\mathrm{dB}$ bandwidth of the used intermediate frequency (IF) filter, also termed B_6. Depending on the observed frequency band it my vary. The respective values are specified in CISPR 16-1-1 [53] and listed in Table 2.2. In this work, a signal is termed narrowband, if not more than one harmonic of the Fourier transformed signal falls within the EMI receiver's resolution bandwidth B_6, as shown in Fig. 2.9(a). The receiver is able to resolve each spectrum line as a discrete frequency. If the signal is broadband, multiple harmonics are within the receiver bandwidth, as in Fig. 2.9(b). The receiver is not able to resolve single spectrum lines, therefore it displays a continuous spectrum, also called the spectrum envelope. In contrast to the EMI receiver's fixed frequency resolution, that of a DFT is a variable given by the number of frequency points and the sampling frequency. Usually, it is much higher than that of an EMI receiver, so that the DFT still resolves discrete spectral lines, even when the EMI receiver

[8] In this work it is taken for granted that the dwell time of the EMI receiver is such that all of the signal spectrum is captured. Besides the minimum timing requirements of the respective measurement standard, for the Peak (PK) detector, the dwell time needs to be at least one complete signal period, while Quasi-Peak (QP) and Average (AVG) detector require the input of at least 3-5 complete periods [54].

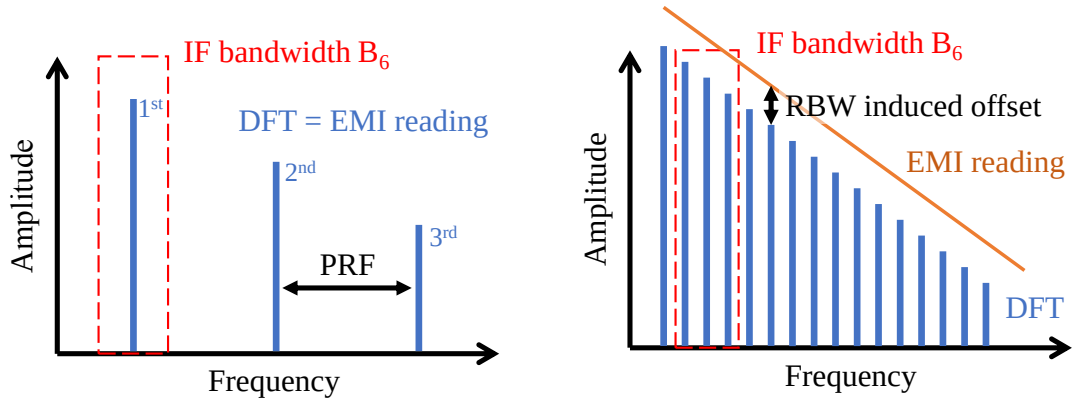

(a) Narrowband signal, $PRF > B_6$: Only one harmonic of the disturbance spectrum is within the bandwidth of the receiver's input filter.

(b) Broadband signal, $PRF < B_6$: Multiple spectral components are within the bandwidth of the receiver's input filter.

Figure 2.9.: Spectral appearance of the EMI receiver reading as function of the disturbance' repetition rate [52]. The example shows the spectrum of a pulse train. The harmonics (blue) are separated by the pulse repetition frequency (PRF).

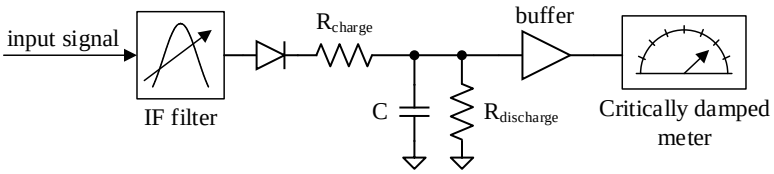

Figure 2.10.: Schematic of the Quasi-Peak detector circuit. If the input voltage is higher than the voltage across the capacitor C, the capacitor is charged via R_{charge}, else, the capacitor is discharged via $R_{discharge}$. The component values are adjusted for each frequency range according the CISPR 16-1-1 specifications. The once mechanical critically damped indicating instrument is nowadays mimicked by a differential equation of second order.

Table 2.2.: CISPR frequency bands and the corresponding $-6\,\mathrm{dB}$ bandwidths of the intermediate frequency filter (IF) [53]. If the repetition rate of a disturbance is higher than the filter bandwidth, the EMI receiver shows the spectrum envelope instead of single peaks, as in Fig. 2.9.

CISPR Band	A	B	C and D
Frequency range	9 kHz - 150 kHz	150 kHz - 30 MHz	30 MHz - 1 GHz
IF bandwidth B_6 (RBW)	200 Hz	9 kHz	120 kHz

displays only an envelope.
For narrowband signals the EMI PK reading is similar to the DFT output. For broadband signals the spectrum envelope displayed by the EMI receiver is higher than the discrete amplitudes of the DFT result. Processing the spectra of broadband signals by DFT only may significantly underestimate the real-world measurement result delivered by the EMI receiver! Of course, disturbing signals can be composed of narrowband and broadband components and the effect on the EMI reading is not always easy to distinguish. Thus, the general use of an EMI receiver emulator to analyze the emission spectrum of transient simulation data is advisable.
Because broadband disturbers appear with low repetition rates, it is tiresome to record them by simulation (or measurement). Fortunately, the increase of the EMI receiver reading with respect to the DFT emission amplitudes due to different resolution bandwidths - termed RBW induced offset in Fig. 2.9(b) - can be mathematically described. Its derivation is one of the novel contributions of this work and will be presented in Chapter 5.1.

2.5.2. Quasi-Peak Detector

The QP detector is supposed to depict the likelihood of noticeable interference between devices better than the PK detector. Unfortunately, its reading is more complicated to simulate than the PK reading, because not only the STFT algorithm but also the QP detector circuit and especially the behaviour of the (former mechanical) critically damped meter needs to be considered. Respective equation is given in CISPR 16-1-1 [53].
Krug and Russer presented an analog and a digital implementation of the QP detector in [57]. The analog approach models the detector circuitry and the inherent critically damped meter with RC elements as depicted in Fig. 2.10 while the digital model uses a cascade of two IIR1-filters (infinite impulse response filter of first order). The bottleneck, however, is the data that needs to be fed to the model. Due to the large discharging time constants of the QP circuit both approaches require a transient input signal of at least $2\,\mathrm{s}$ length, which may lead to very long simulation times. Hence, the accuracy of the emulated QP reading is commonly traded for computation speed. In [54], for instance, a solution is given by calculating the QP result from the AVG reading as function of the pulse repetition frequency (PRF)[9]. This reduces the required simulation output to a few ms. Unfortunately, the approach can only be applied for periodic pulsed disturbances.
This work focuses on the application of data transmission devices. Typical output signals consist of sections of active data transmission with in-between idle times of various duration. Such data transmission streams are usually very long, whereas the signal contents that constitute the emission spectrum are only short chunks. Moreover, the signal period is extremely long or the transmissions might not be periodic at all. For real measurements this means that the measurement or dwell time needs to be increased accordingly, which of course slows down the measurement. When the QP reading should be found by (IC

[9] The derivations given in [54] basically yield the characteristics plotted in [52].

level) simulation, this is an even bigger issue, because, first, simulation of the complete data transmission is often not processable, and second, during the circuit or system design phase the designer doesn't know which data stream will be output during the EMC tests. It was part of this thesis to consider suchlike issue for the first time! In Chapter 5.2 an EMI receiver software emulator with implementation of a QP detector optimized for the processing of long data streams will be presented.

2.6. Chapter Conclusion and Outlook

The ALSE test is a system level EMC test to evaluate the radiated emission originating from a cable harness connected to the DUT. From IC level point of view it is difficult to predict system level RE, especially if the prediction should be found by simulation only and if the IC is used in a complex system. The task gets more complicated with increasing frequency. The IC manufacturer usually does not know the final application PCB and has no models of the used components. However, simplifications can be applied that enable to generate a simulation model suitable for IC level simulation up to $30\,\mathrm{MHz}$ without knowledge the overall system realization.
For this reason, the work in this thesis was limited to the frequency range from $150\,\mathrm{kHz}$ to $30\,\mathrm{MHz}$, which corresponds to CISPR Band B where ALSE tests are performed solely with the $1\,\mathrm{m}$ rod antenna.
For frequencies below some MHz electrostatic conditions apply and radiated emissions can be forecast with very good accuracy. Above, the anechoic chambers itself has a major impact because a main parameter leading to deviating measurement results in different chambers – the ground plane connection – is excluded during the chamber validation procedure. As a result, a simulation model can only represent a given real test setup but it cannot guarantee precise prediction of measurement results obtained in an arbitrary laboratory. That is also true because of all the freedoms of interpretation an EMC engineer has within the standardized regulations. Fortunately, CISPR 25 does not define emission limits between $1.8\,\mathrm{MHz}$ (end of MW or AM band) and $30\,\mathrm{MHz}$ (with exception of the narrow SW band $5.9\,\mathrm{MHz}$ to $6.2\,\mathrm{MHz}$ and the CB band from $26\,\mathrm{MHz}$ to $28\,\mathrm{MHz}$). Most automotive manufacturers stick close to the frequency bands defined in the standard. Hence the simulation of radiated emissions between $1.8\,\mathrm{MHz}$ and $30\,\mathrm{MHz}$ has only informative character but can be considered mostly irrelevant for the validation of electromagnetic compatibility!

The majority of published approaches to simulate RE of ICs is not suitable for continuous use by the circuit designer. The designer (in person) is normally no EMC expert and does not want to deal with additional, complex simulation tools. In this thesis the generation of a simple simulation model is presented which can easily be implemented in the native circuit design environment (e.g. SPICE or Cadence Virtuoso) used by the designer and does not notably increase the simulation time. The focus is on ALSE measurements with the

vertical monopole antenna only. The outcome will be an equivalent circuit of the coupling path similar to Fig. 2.6(b).
Chapter 3 discusses direct capacitive coupling between a straight cable harness and the rod receiver antenna. This is the major coupling mechanism in the ALSE test for frequencies below roughly $3\,\mathrm{MHz}$. Based on electrostatic field theory the transmission factor between cable and receiver antenna will be analytically derived. Additionally, the impact of different types of load driving schemes and cable harnesses will be discussed.
Chapter 4 step by step introduces all parts needed to generate a circuit model to simulate the ALSE test result in the complete CISPR Band B up to $30\,\mathrm{MHz}$ and discusses the corresponding theory.
Chapter 5 concludes with the post-processing of the simulation data using an EMI receiver emulator. It focuses on the processing and the spectral appearance of long data streams, which are typical test signals for DUTs that are intended for data transmission.

It is important to keep in mind that the tolerance for chamber validation is $\pm 6\,\mathrm{dB}$ of the reference data. This uncertainty range of $12\,\mathrm{dB}$ comes on top of every simulation result. Hence, even if a simulation aligns perfectly with measurements, component manufacturers should be very careful to guarantee absolute emission readings to their costumers.

3. Electrostatic Approach to Express the Coupling Below 3 MHz

3.1. Derivation of the Capacitive Coupling Factor

It was shown in the preceding chapter that below roughly $3\,\mathrm{MHz}$ the dominant 'radiation' mechanism is direct capacitive coupling between the radiation source, i.e. the cable harness, and the vertical monopole receiver antenna. It results in a constant transmission factor which is approximately $-40\,\mathrm{dB}$. This value was measured or simulated by other contributions before, but it was never derived analytically. As a first step towards the intended simulation model, this chapter will present how to calculate this transmission factor (TF) using fundamental equations from electrostatic field theory.
The presented analytic approach was first published by the author in [39] and used in [58]. It is based on the setup illustrated by Fig. 3.1 with the values from Table 3.1 and applies some assumptions or simplifications:

- The wavelength (in vacuum) at $150\,\mathrm{kHz}$ is approximately $2\,\mathrm{km}$, at $30\,\mathrm{MHz}$ it is $10\,\mathrm{m}$, but the length of the cable harness is only $1.5\,\mathrm{m}$. Hence, within the considered frequency band there is no wave propagation along the harness. It is therewith justified to assume static conditions, i.e. the voltage potential at the cable is regarded as constant over the whole cable length and phase and time issues are neglected. The near-field measurement results given in [7] confirm that the amplitude of the radiated field is constant along the full cable length for frequencies up to $10\,\mathrm{MHz}$.
- It is assumed that the receiver antenna itself does not affect the local E-field at the observation point, nor does the receiver electronics influence the voltage reading, i.e. the receiver's input impedance is assumed to be very high. The influence of two parameters of a real rod antenna (radius and termination impedance) is in short addressed in Chapter 3.2.
- Also any impact of the coaxial cable connecting the antenna output to the EMI receiver input is neglected. It is known from literature (see Chapter 2.1.2) that the antenna cable might influence the emission reading above $10\,\mathrm{MHz}$.
- The ground plane is a perfect electric conductor.
- For now, the ground plane is assumed to be infinite. The finite ground plane will be considered in Chapter 3.4.

Cable harnesses for automotive applications are often composed of unshielded twisted pair cables. This is also the default cable type used in this work. When dealing with cables consisting of multiple wires it is common to replace the compound by an equivalent single wire approximation (similar to Fig. 2.7 of Chapter 2.3.1). The following derivations assume that the cable harness under consideration can be regarded as single (equivalent) wire. A closer definition will be given in Chapter 3.5.1.

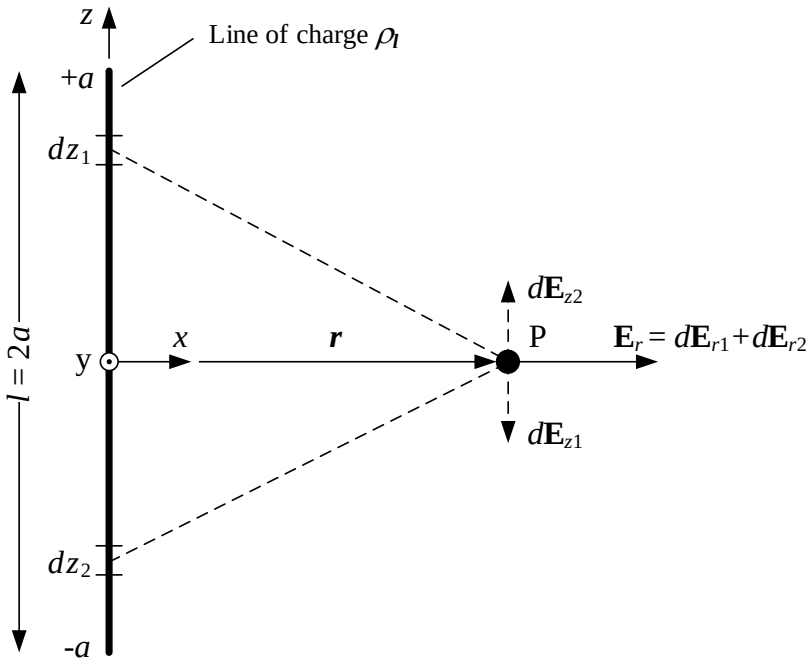

(a) Top view: The harness of length $l = 2a$ is replaced by a line charge density ρ_l placed along the z-axis ranging from $(x, y, z) = (0, 0, -a)$ to $(0, 0, +a)$. Because the rod antenna (labeled by point P) is located at the center of the harness at $z = 0$, the E-field components $d\mathbf{E}_z$ add to zero, so that $\mathbf{E}$ is only a function of r.

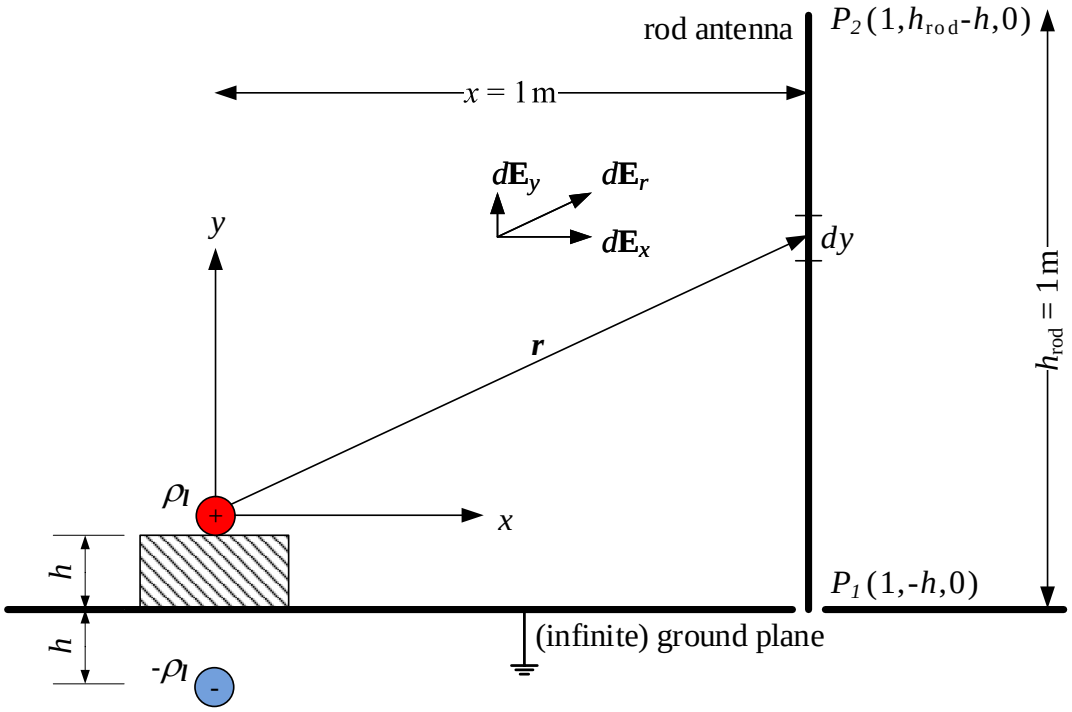

(b) Side view: The line charge density ρ_l is placed along the z-axis at $(x, y) = (0, 0)$. It is mirrored with negative sign below the ground plane at $y = -2h$. The vertical rod antenna of height $h_{\mathrm{rod}} = 1\,\mathrm{m}$ is located at $1\,\mathrm{m}$ distance in x-direction.

Figure 3.1.: Calculation setup for electrostatic solution (infinite ground plane)

3.1.1. Calculation Applying the Voltage Potential

The capacitance per meter [F/m] of a cylindrical conductor, i.e. a wire, of radius r_0 in distance h above an infinite ground plane (as depicted by Fig. 2.7(b) or Fig. 3.11(a)) is expressed by (3.1) given that $h \gg r_0$ [59].

$$C'_{\text{wire}} = \frac{2\pi\varepsilon_0}{ln(\frac{2h}{r_0})} \tag{3.1}$$

The wire will acquire a charge Q [C] as function of its potential V_{wire} [V] and capacitance towards a reference conductor, which is the ground plane. When the wire is very thin compared to its length l [m] it can be represented by a line charge density ρ_l [C/m] (3.2).

$$\rho_l = Q/l = C'_{\text{wire}} \cdot V_{\text{wire}} \tag{3.2}$$

The ALSE setup cable harness is far longer than its overall diameter, hence above simplification applies, which leads to the calculation setup sketched by Fig. 3.1. The potential Φ at a point $P(x, y, z)$ induced by a finite line of charge of length $l = 2a$ centered at $(0, 0, 0)$ is then given by (3.3) [60]

$$\Phi(x, y, z) = -\frac{\rho_l}{4\pi\varepsilon_0} ln\left(\frac{z - a + \sqrt{r^2 + (z - a)^2}}{z + a + \sqrt{r^2 + (z + a)^2}}\right) \tag{3.3}$$

where

$$r = \sqrt{x^2 + y^2} \tag{3.4}$$

Whenever a charge is located near a comparatively large grounded plane, image theory is used to express the impact of the plane on the electric field distribution. As depicted in Fig. 3.1(b), the line charge density ρ_l representing the wire is in distance h above the ground plane, hence the image $-\rho_l$ is introduced. The resulting potential along the rod antenna of length h_{rod} from $y = -h$ to $y = h_{\text{rod}} - h$ is

$$\Phi_{\text{total}}(x, y, z)\Big|_{y=-h}^{y=h_{\text{rod}}-h} = \Phi_{\text{original}}(x, y, z)\Big|_{y=-h}^{y=h_{\text{rod}}-h} - \Phi_{\text{image}}(x, y, z)\Big|_{y=+h}^{y=h_{\text{rod}}+h} \tag{3.5}$$

Note that (3.5) is valid for an arbitrary placement of the receiver antenna in the (x, z) plane.

The E-field reading corresponds to the maximum potential value along the path of the rod antenna. Fig. 3.2 plots the evolution of the electric potential for a setup as in Fig. 3.1 for a vertical receiver antenna at observation point $P(1, y, 0)$, i.e. $1\,\text{m}$ in x-direction away from the center of the line charge at $z = 0\,\text{m}$. The plot assumes that the source is at a potential of $0\,\text{dBV}$, hence the maximum induced receiver potential is equal to the coupling attenuation, i.e. the transmission factor. Additionally, the plot shows the results from electrostatic 3D simulation using the setups from Fig. 3.3 and Fig. 3.4. From this the impact of a finite ground plane or the real 'table shaped' ground plane becomes visible: The smaller the ground plane, the higher is the potential induced at the observation point. More details regarding this issue will be discussed in Chapter 3.4.

Table 3.1.: Parameters of the ALSE test setup according Fig. 3.1 used in Chapters 3.1.1 and 3.1.2

Description	Symbol	Value
Permittivity of vacuum	ε_0	$8.854 \cdot 10^{-12}\,\mathrm{F/m}$
Length of rod monopole receiver	h_{rod}	$1\,\mathrm{m}$
Distance of cable harness from ground plane	h	$0.05\,\mathrm{m}$
(Equivalent) wire radius	r_0	$0.001\,\mathrm{m}$
Cable length	$l = 2a$	$1.5\,\mathrm{m}$
Observation distance in x-direction	x	$1\,\mathrm{m}$
Position along rod receiver in y-direction	y	ranging from $h_{\mathrm{rod}} - h$ to $h_{\mathrm{rod}} + h$
Position along cable in z-direction	z	ranging from $-a$ to $+a$
Line charge	ρ_l	$C'_{\mathrm{wire}} \cdot V_{\mathrm{wire}}$
(Equivalent) line potential	V_{wire}	$1\,\mathrm{V} = 0\,\mathrm{dBV}$
Capacitance/meter between wire and ground	C'_{wire}	(3.1)
Voltage received by the monopole antenna	V_{rod}	(3.14)

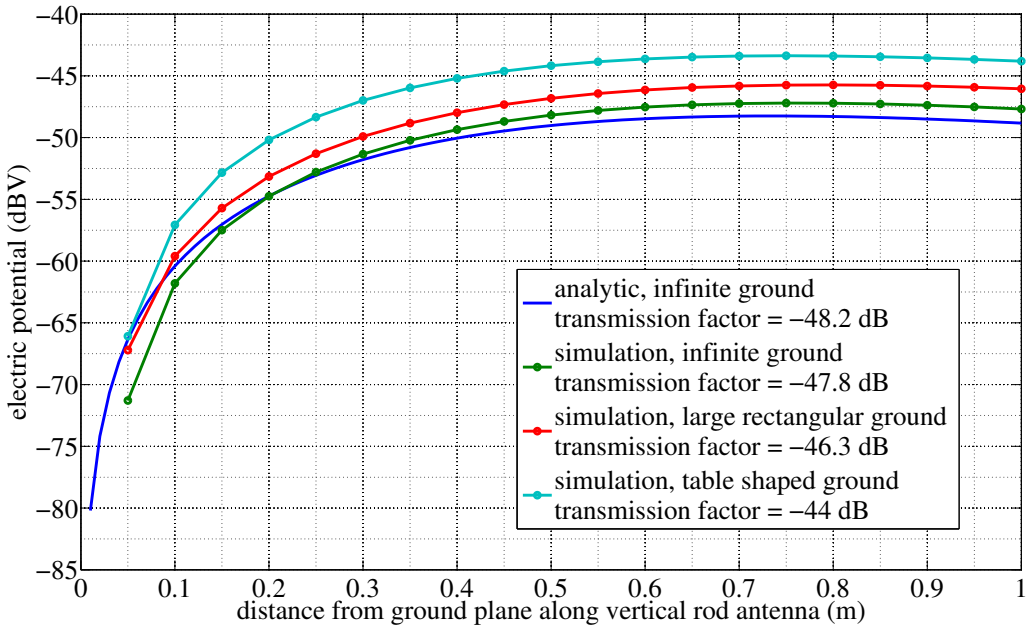

Figure 3.2.: Plot of the electric potential along the $1\,\mathrm{m}$ vertical rod receiver antenna at $P(x, y, z) = P(1\,\mathrm{m}, 0, z)$ originating from a $1\,\mathrm{m}$ long line charge with $r_0 = 1\,\mathrm{mm}$ at a potential of $1\,\mathrm{V}$, i.e. $0\,\mathrm{dBV}$. Compared are the analytic results obtained with (3.1) and (3.5) to those from electrostatic 3D simulation.

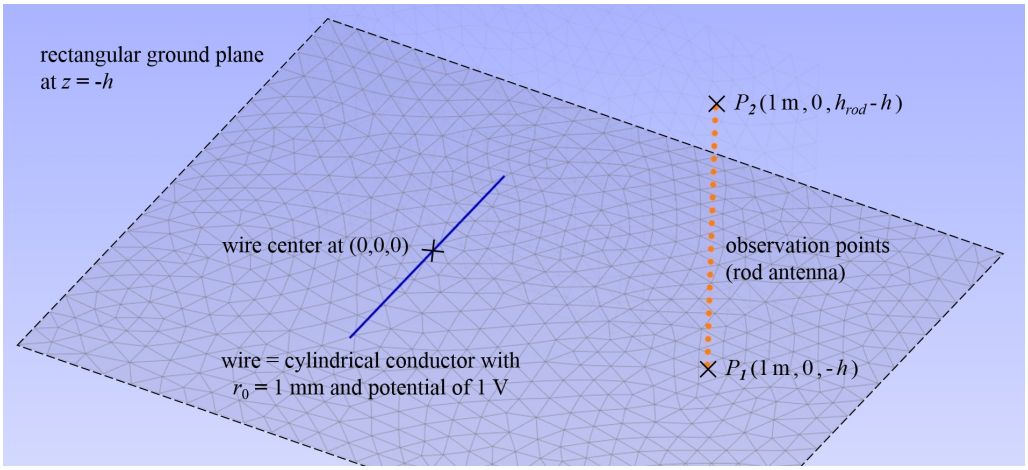

Figure 3.3.: EMCoS 3D simulation setup featuring an infinite or large rectangular ground plane. The blue line is a cylindrical conductor representing a single wire. With the electrostatic solver the electric potential in the orange observation points is computed.

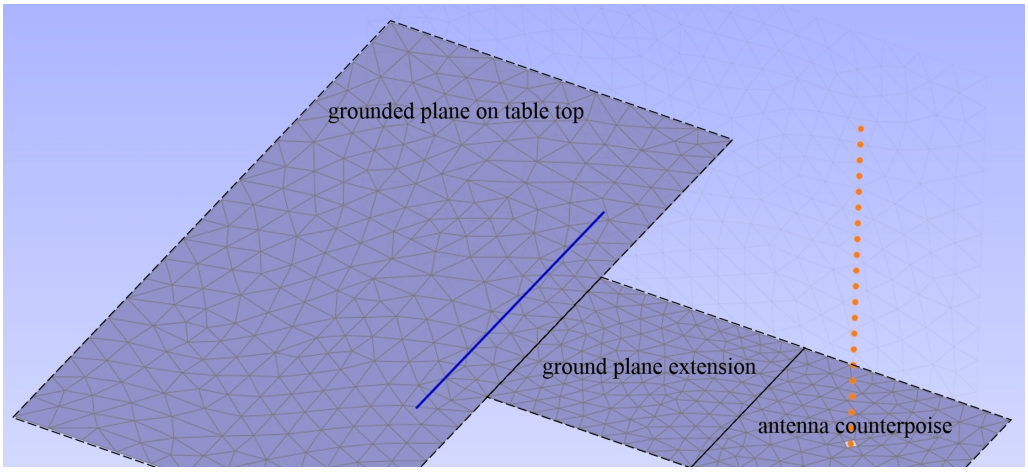

Figure 3.4.: EMCoS 3D simulation setup similar to Fig. 3.3 but with table shaped ground plane.

3.1.2. Closed Form Solution by Integration of the E-Field

From above approach the coupling to the rod antenna can already be illustrated, but the receiver reading has to be found by looping over the values of y and a max function. A more convenient closed form solution can be given by applying (3.6) which delivers the electric field vectors invoked by Φ.

$$\mathbf{E} = -\nabla\Phi \tag{3.6}$$

In general, the E-field $d\mathbf{E}$ at a point **P** excited by a segment dz of the line charge consists of two components $d\mathbf{E}_r$ and $d\mathbf{E}_z$, hence is a function of *x*, *y* and *z*. [60] gives the general equations for the field components. In the special case exhibited by Fig. 3.1(a) where **P** is located at the center of the line charge at $z = 0$, the negative and positive z-components add to zero so that the E-field in *r*-direction is only a function of *x* and *y* [61]:

$$\mathbf{E}_r = \frac{\rho_l \cdot r}{4\pi\varepsilon_0} \int_{-a}^{+a} \frac{dz}{(r^2+z^2)^{3/2}}\,\mathbf{e}_r = \frac{\rho_l}{2\pi\varepsilon_0} \frac{1}{r\sqrt{(\frac{r}{a})^2+1}}\,\mathbf{e}_r \tag{3.7}$$

The monopole antenna captures mainly vertical E-field, which is the component in *y*-direction. The impact of magnetic field components on the measurement results can be neglected, which results in a low error of $1\,\mathrm{dB}$-$3\,\mathrm{dB}$ [7]. With

$$r\,\mathbf{e}_r = x\,\mathbf{e}_x + y\,\mathbf{e}_y \qquad \text{thus} \qquad \mathbf{e}_r = \frac{x}{r}\,\mathbf{e}_x + \frac{y}{r}\,\mathbf{e}_y \tag{3.8}$$

the *y*-component of the electric field from (3.7) is

$$\mathbf{E}_y = \frac{\rho_l}{2\pi\varepsilon_0} \cdot \frac{y}{r^2\sqrt{(\frac{r}{a})^2+1}}\,\mathbf{e}_y \tag{3.9}$$

The voltage at the top point of the (virtual) rod antenna P_2 towards its reference point P_1 can be found by integrating the E-field (3.9) along the height of the rod (3.10). Note that this is an idealized view, which does not consider that a real antenna would deform the field due to its metallic surface.

$$V_{P_1,P_2} = -\int_{P_1}^{P_2} \mathbf{E}_y \cdot dy \tag{3.10}$$

Above integral (3.10) yields a voltage which is the measured quantity in the ALSE test. It equals the displayed E-field reading in V/m, because the rod is exactly $1\,\mathrm{m}$ long. Because the rod antenna is in distance h above the ground plane, where the line charge density ρ_l gets mirrored, the receiver captures the sum of the voltages induced by the original and the mirrored charge, V_{ρ_l} and $V_{-\rho_l}$ respectively. With a rod antenna height of h_{rod} the voltage received by the antenna can be expressed as (3.11) and (3.12).

$$V_{\mathrm{rod}} = V_{\rho_l} + V_{-\rho_l} = \int_{h_{\mathrm{rod}}-h}^{-h} \mathbf{E}_y \cdot dy - \int_{h_{\mathrm{rod}}+h}^{+h} \mathbf{E}_y \cdot dy \tag{3.11}$$

$$V_{\mathrm{rod}} = \frac{\rho_l}{2\pi\varepsilon_0} \int_{h_{\mathrm{rod}}-h}^{h_{\mathrm{rod}}+h} \frac{y}{r^2\sqrt{(\frac{r}{a})^2+1}}\,dy \tag{3.12}$$

Respecting $r = \sqrt{x^2 + y^2}$ an analytical solution for (3.12) can be found as (3.13). It is valid for an arbitrary wire length $l = 2a$ and distance from the ground plane h, as well as variable observation distance in x-direction and rod antenna length h_{rod}.

$$V_{\text{rod}} = \frac{-\rho_l}{2\pi\varepsilon_0} \cdot \tanh^{-1}\left(\frac{\sqrt{a^2 + x^2 + y^2}}{a}\right)_{y=h_{\text{rod}}-h}^{y=h_{\text{rod}}+h} \tag{3.13}$$

The received voltage can be further expressed in terms of the voltage at the wire as (3.14) by inserting $\rho_l = C'_{\text{wire}} \cdot V_{\text{wire}}$ and (3.1).

$$V_{\text{rod}} = V_{\text{wire}} \cdot \frac{-1}{ln(\frac{2h}{r_0})} \cdot \tanh^{-1}\left(\frac{\sqrt{a^2 + x^2 + y^2}}{a}\right)_{y=h_{\text{rod}}-h}^{y=h_{\text{rod}}+h} \tag{3.14}$$

$$V_{\text{rod}} = \frac{\rho_l}{C'_{\text{wire}}} \cdot \frac{-1}{ln(\frac{2h}{r_0})} \cdot \tanh^{-1}\left(\frac{\sqrt{a^2 + x^2 + y^2}}{a}\right)_{y=h_{\text{rod}}-h}^{y=h_{\text{rod}}+h} \tag{3.15}$$

Here (3.15) is given explicitly although it is redundant to (3.14) because from that presentation it gets obvious that V_{rod} is proportional to the wire's capacitance towards the ground plane! An electrostatic or capacitive coupling factor k_{cap} can be defined as the ratio of voltage received at the rod antenna and that on the wire (3.16). It is a function of the setup's geometry but independent of the frequency!

$$k_{\text{cap}} = \frac{V_{\text{rod}}}{V_{\text{wire}}} \tag{3.16}$$

If the complete E-field $\mathbf{E}_r$ of (3.7) was used for above derivation instead of only the E-field in y-direction $\mathbf{E}_y$ (3.9), the resulting voltage V_{rod} (hence k_{cap}) would increase by approximately $1.2\,\text{dB}$ in case of a $1.5\,\text{m}$ wire, whereas the deviation is a function of the wire's length $l = 2a$. For four exemplary values the deviation ΔV_{rod} is given by Table 3.2. The derivation via $\mathbf{E}_y$ was chosen, because the resulting values fit better those from the approach applying the voltage potential of Chapter 3.1.1, as well as the results from 3D simulation (compare Table 3.4). Generally speaking, however, it needs to be noted that both approaches of Chapters 3.1.1 and 3.1.2 used the prior listed simplifications. That is, the metal body of the rod antenna itself, which would deform the E-field, was not respected, nor was any other impact of the real-life test setup. Thus, the results from above analytic considerations have to be regarded as vast approximation. In the following subsections, some of the real setup's components will be addressed. Again, the presented investigations are useful to explain the principle of capacitive coupling as major mechanism leading to the low-frequency field readings observed during the ALSE test with the rod antenna, but must not be understood as attempt to precisely predict the measurement results.

Table 3.2.: Deviation of induced voltage at the rod antenna ΔV_{rod} when calculated by respecting $\mathbf{E}_r$ or only the E-field in y-direction $\mathbf{E}_y$ as function of wire length.

wire length	l=0.5 m	l=1 m	l=1.5 m	l=2 m
$\Delta V_{\text{rod}} = V_{\text{rod}}(\mathbf{E}_r)/V_{\text{rod}}(\mathbf{E}_y)$	+2.7 dB	+2.1 dB	+1.2 dB	+0.3 dB

3.2. Considering the Antenna Factor

Above calculations investigated the E-field along the path of the virtual rod receiver antenna but omitted the impact of the actual metallic rod itself, as well as the termination impedance of the antenna. Both, however, have significant impact on received voltage V_{rod} and thereby on the coupling factor k_{cap}. For visualization, simulations were conducted with a setup similar to Fig. 3.3, i.e. with infinite ground plane. The results are displayed by Fig. 3.5. It shows a parametric sweep over three values for the radius of the rod antenna r_{rod} and three values for possible termination impedances. The radius $r_{\text{rod}} = 8\,\text{mm}$ is that of the Schwarzbeck VAMP 9243 active rod antenna which was used for most measurements conducted for this work. From Fig. 3.5 it can be observed, the transmission factor between wire and rod antenna is frequency independent, as long as the rod´s termination impedance Z_{term} is high compared to its self-capacitance towards ground C_{rod}. Then, the capacitive divider formed by $C_{\text{wire-rod}}$ and C_{rod} illustrated by Fig. 3.6 yields a frequency independent coupling factor. This effect will again be addressed in Chapter 3.6 by means of (3.25). The capacitance C_{rod} is a function of the rod´s radius r_{rod}, as expressed by (3.17). The actual voltage V_{rod} is hence a function of Z_{term} and r_{rod}. Fig. 3.5 shows some examples. An impedance higher than e.g. $10\,\text{M}\Omega$ means that the rod is as good as floating and yields values for TF that come closest to the ideal values derived in above section. Further considerations on the impact of the termination impedance are made in [62]. Effects of the antenna input circuit on the received spectrum above $10\,\text{MHz}$ are discussed based on experiments in [18].

$$C_{\text{rod}} = \frac{2\pi\varepsilon_0 \cdot h_{rod}}{ln(\frac{h_{rod}}{r_{rod}})} \tag{3.17}$$

Eventually, it is the task of the antenna manufacturer to provide a correction factor - the so-called antenna factor - that accounts for the above mentioned real-life effects of the rod antenna and the in-built measurement circuit, so that the reading given by the EMI receiver displays the actual field values freed from the antenna‘s impact. As long as this antenna factor is respected during the ALSE measurements, it does not need to be considered in simulation. Hence, during this thesis, the impact of the antenna on the measured field will not further be discussed. V_{rod} resulting from (3.14) is understood to equal the voltage that ideally should be output by the antenna receiver.

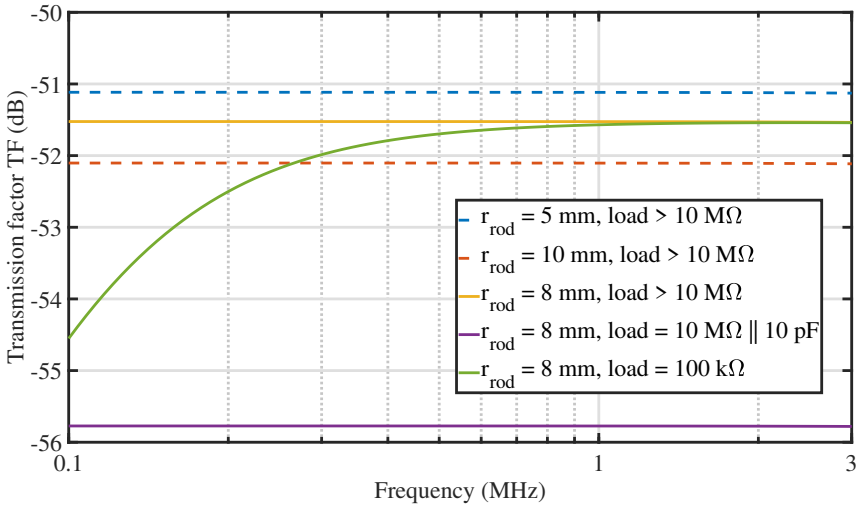

Figure 3.5.: Impact of the rod antenna´s radius and termination impedance on the transmission factor, i.e. the received voltage V_{rod}, below $3\,\mathrm{MHz}$. Results were obtained by 3D EM simulation, using an infinite ground plane and a single wire harness of $r_0 = 1\,\mathrm{mm}$ and $1\,\mathrm{m}$ length.

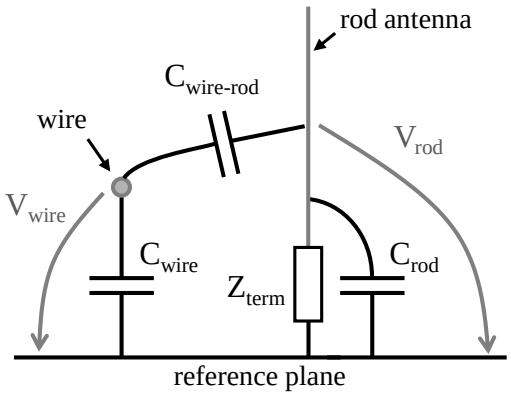

Figure 3.6.: Illustration of the capacitive coupling between wire and rod receiver antenna, including the rod´s termination impedance given by the attached measurement circuit.

3.3. Impact of Cable Length and Radius on Direct Capacitive Coupling

The CISPR 25 standard defines a cable length of minimum $1.5\,\mathrm{m}$ but also allows longer harnesses within a certain range. Though, due to practical reasons, e.g. multiple or large loads connected to the cable end(s), vehicle manufacturers sometimes extend the length limits or prescribe the use of longer cables. Fig. 3.7 plots the transmission factor resulting from (3.14) for the values from Table 3.1 and increasing cable length l. Here $l = 1\,\mathrm{m}$ yields $\mathrm{TF} = -48\,\mathrm{dB}$, which is similar to the value of Fig. 3.2 obtained in the preceding chapter by (3.5). It is interesting to observe that emissions are increasing with increasing cable length - as expected - but saturate when the cable becomes very long. This is because radiation originating from portions of the harness being very far from the receiving antenna hardly contributes to the measured E-field. However, because test benches are not infinitely large, in real ALSE setups the cable length seldom exceeds $3\,\mathrm{m}$.
Furthermore, it can be observed from (3.14) that if all parameters of the measurement setup - including the wire length and potential - are constant, the RE result finally depends on the wire radius. The thicker the wire, the higher is the radiated emission. To verify this statement ALSE tests were conducted using exactly the same measurement environment but two different cable types, namely a tightly twisted pair cable with an overall diameter of $3\,\mathrm{mm}$ and a non-twisted audio cable with about double the diameter. Fig. 3.8 is a photo of the cables. It is assumed that twisting of the cables does not affect the radiated emission at very low frequencies. In Table 3.3 the transmission factors extracted from the measurements result are compared to the calculation results using (3.14) and - as lookahead to the next chapter - (3.18). The analytic prediction shows the expected impact of the wire radius, though the final deviation due to the different cable types is very small.

3.4. Considering the Ground Plane Size

The analytic discussion so far assumed an infinite ground plane. In the real ALSE setup this is not the case. As can be observed from Fig. 3.2 - by comparing the traces from simulation for infinite versus table shaped ground plane - or Table 3.3 - comparing the measurement result versus the analytic solution using (3.14) - that not respecting the finiteness of the ground plane introduces errors of up to $6\,\mathrm{dB}$. In this chapter an empirically derived correction to (3.13) is introduced to resolve this issue.
In [27] the impact of the finite ground plane was experimentally investigated by placing the EUT either on the chamber floor or on the default table with ground extension to the receiver counterpoise. The results were already illustrated by Fig. 2.3. For this work similar measurements were conducted with a large elevated ground plane. Fig. 3.10 gives a photo of the measurement setup. All results are collected in Table 3.4 and can be summarized as follows:

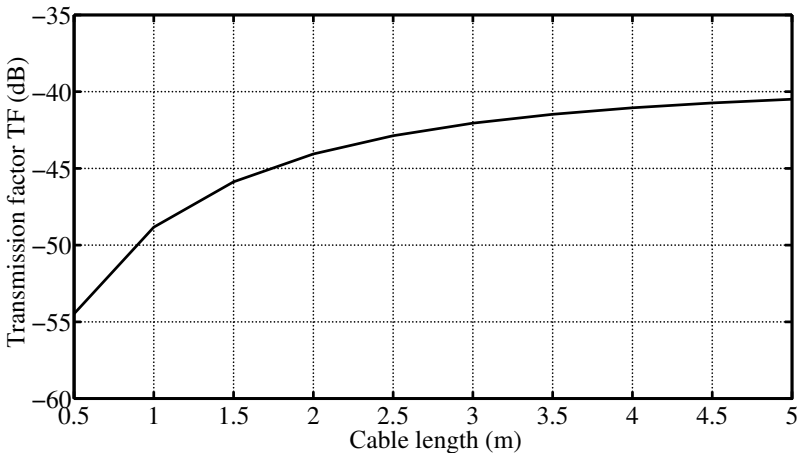

Figure 3.7.: ALSE TF as function of cable length according (3.14) with the values from Table 3.1 (infinite ground, $r_0 = 1\,\mathrm{mm}$): Emissions increase with cable length but saturate for very long cables at a TF close to $-40\,\mathrm{dB}$.

Figure 3.8.: Comparison of the tightly twisted pair cable (black, $r_\mathrm{w} = 0.42\,\mathrm{mm}$, $s = 1.5\,\mathrm{mm}$) and the non-twisted audio cable (white, $r_\mathrm{w} = 0.62\,\mathrm{mm}$, $s = 2.8\,\mathrm{mm}$) used for the measurements of Table 3.3

Table 3.3.: Electrostatic coupling factors for the two cables of Fig. 3.8. The analytic calculation uses the equivalent single-wire radius $r_\mathrm{eq} = \sqrt{r_\mathrm{w} s} = r_0$.

	twisted pair l=1.5 m $r_0 = 0.8\,\mathrm{mm}$	audio cable l=1.5 m $r_0 = 1.3\,\mathrm{mm}$	ΔRE
measurement	$-40\,\mathrm{dB}$	$-37\,\mathrm{dB}$	$+3\,\mathrm{dB}$
analytic (3.14)	$-46.3\,\mathrm{dB}$	$-45.3\,\mathrm{dB}$	$+1\,\mathrm{dB}$
analytic (3.18)	$-41.1\,\mathrm{dB}$	$-40.2\,\mathrm{dB}$	$+0.9\,\mathrm{dB}$

- The larger the ground plane, the lower is the radiation. [1] This can be understood from the method of image charges illustrated in Fig. 3.1(b): The image charge introduced to respect the ground plane partly compensates the field of the original charge. In measurements the difference between large and default ground plane size is about $2\,\mathrm{dB}$. In simulation this deviation is more pronounced and gets even bigger with increasing cable length.
- The 3D simulations did not include a model of the surrounding chamber. The fact that the simulation results for l=$1\,\mathrm{m}$ and l=$1.5\,\mathrm{m}$ fit well to the measurements (table ground) and analytic predictions (infinite ground) proves that for the considered low frequencies the shielded enclosure and the absorber lining are negligible. (In [39] it was wrongly assumed that charge images at the chamber walls need to be considered.)

The analytic calculation can be adjusted to better respect the real shape of the ground plane. The idea is illustrated by Fig. 3.9: In the ALSE test the cable is placed close to the edge of the ground plane, i.e. the table. For most of the cable's length, the underneath ground plane ends nearby at the table's edge. Thus, the simplification of an infinite ground plane - modeled by inserting a mirror charge - overestimates its impact. Only at the center of the cable the ground plane extends towards the receiver antenna counterpoise. Exclusively here the concept of a large ground plane applies, so that a respective part of the original line of charge is mirrored. By electrostatic 3D simulation similar to Fig. 3.3, but with the ground plane replaced by a wire of negative potential and variable length, it was found that the length of the mirrored line charge l_{image} is not equal to the width of the counterpoise extension but is roughly proportional to the length l of the cable harness. $60\,\%$ of the full cable length is a conformable value, which accounts as long as the cable is significantly longer than the ground plane extension is wide, i.e. $l \geq 1\,\mathrm{m}$ for a typical counterpoise width of $0.6\,\mathrm{m}$. (3.13) is modified as such leading to (3.18). According Fig. 3.1(b) the integration limits are $y = h_{\mathrm{rod}} - h$ to $y = -h$ for the original line charge of length $2a$ and $y = h_{\mathrm{rod}} + h$ to $y = +h$ for the negative line charge image of length $2a_{\mathrm{image}} = 2 \cdot 0.6a$. The results from (3.18) are added to Table 3.4. They correspond well to the measured and simulated results. Unfortunately, only few data points are available to verify the approach.

$$V_{\mathrm{rod}} = \frac{-\rho_l}{2\pi\varepsilon_0} \left[\tanh^{-1}\left(\frac{\sqrt{a^2 + x^2 + y^2}}{a} \right)_{y=h_{\mathrm{rod}}-h}^{y=-h} - \tanh^{-1}\left(\frac{\sqrt{a_{\mathrm{image}}^2 + x^2 + y^2}}{a_{\mathrm{image}}} \right)_{y=h_{\mathrm{rod}}+h}^{y=+h} \right] \tag{3.18}$$

[1] The measurements in [27] show the other way around. In this point they do not align with the simulations and measurements of this work. From the setup photo in Chapter 4.2.1 of [27] it *seems* that during the measurements at the chamber floor the monopole receiver counterpoise, i.e. the reference potential, was only loosely grounded via the coax cable shield. This would explain the shift in the measurement results.

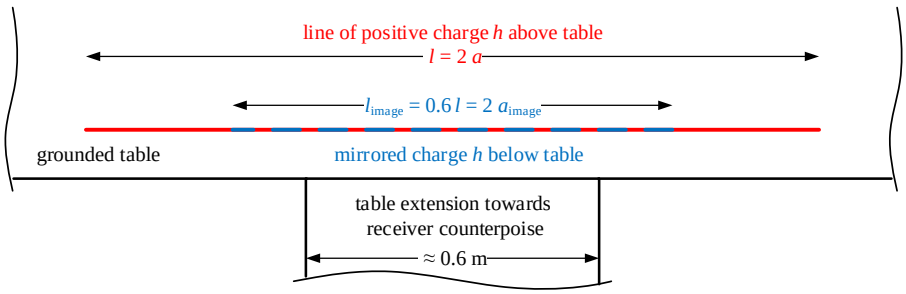

Figure 3.9.: To respect the table-shaped ground plane analytically, only 60 % of the full cable length centered around the ground extension are mirrored. (This simple correction of the ground plane size holds as long as the cable is significantly longer than the ground extension is wide.)

Table 3.4.: Coupling factors k_{cap} for a single wire of various length and radius, obtained by different means.

	l=0.5 m $r_0 = 2\,\mathrm{mm}$	l=1 m $r_0 \approx 1\,\mathrm{mm}$	l=1.5 m $r_0 \approx 1\,\mathrm{mm}$
Measurement (table ground)	≈−50 dB [26][2]	−43 dB	−41 dB −45 dB [27]
Measurement (large ground) elevated (Fig. 3.10) chamber floor		−45 dB	−43 dB −43 dB [27]
Analytic (table ground) partial image (3.18)		−42.2 dB	−40.7 dB
Analytic (infinite ground) potential (3.5) E-field (3.14)	−52.4 dB −53.1 dB	−48.2 dB −48.8 dB	−45.4 dB −45.9 dB
Simulation (table ground) 3D electrostatic 3D EM		−44.0 dB	−39.1 dB
Simulation (infinite ground) 3D electrostatic 3D EM	−58.9 dB [1] −49 dB [26][2]	−47.8 dB	−46.7 dB

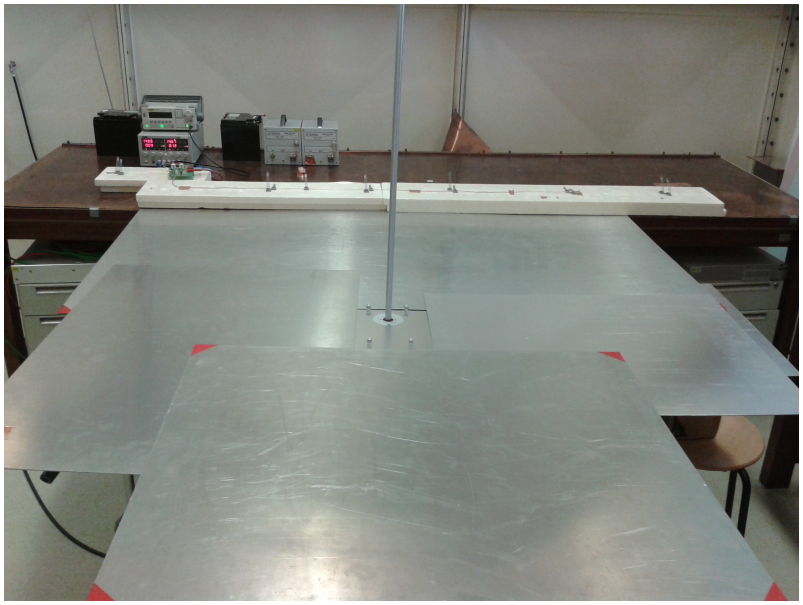

Figure 3.10.: ALSE measurement setup with a large elevated ground plane used to obtain the result listed in Table 3.4

3.5. Radiation from Two Identical Parallel Cables

3.5.1. Equivalent Line Potential V_{wire} and Equivalent Single-Wire Radius r_{eq}

The above derivations showed that the voltage V_{rod} received by the rod antenna due to electrostatic coupling is proportional to the voltage at the cable harness V_{wire}. For simple setups where the complete harness consists of only a single wire, V_{wire} is the voltage signal which is intentionally delivered to the load. This voltage signal can usually be easily simulated, as it is the direct output of the DUT. The low-frequency emission captured during the ALSE test is proportional to this well known quantity. However, in most cases V_{wire} is rather an equivalent part of the cable voltage which couples to the receiver antenna, namely the common-mode (CM) voltage[3]. Though, remembering $Q = C \cdot V$ or $\rho_l = C'_{\text{wire}} \cdot V_{\text{wire}}$ and (3.13), the electric field originating from the cable is not produced by the potential or voltage V_{wire} alone, but rather by the charge at the conductor, which is also a function of the capacitance C'_{wire}. Only if C is constant, the charge and hence the coupling to the receiver antenna is directly proportional to V. Then, as will be exhibited, it is possible to replace a cable bundle with a single-wire equivalent holding an equivalent line potential which equals the CM voltage at the original bundle.

[2]The signal input to the radiator used in [26] is scaled by a resistor divider of $120\,\Omega$ and $150\,\Omega$. A factor of $150/270 = -5\,\text{dB}$ is applied to given injection voltage to obtain the transmission factor.

[3]As discussed in the introduction chapter, it is widely known and accepted that CM *currents* are the major source of a cable's radiation. Hence, it is easily stated at this point, that as long as electrostatic coupling prevails, RE is due to CM *voltages*.

For a single wire at potential V_1 the capacitance towards the ground plane can be calculated by (3.1) and the corresponding wire charge Q is directly proportional to V_1. Obviously, as there is only one line potential in the system the single wire potential V_1 is equal to the equivalent line potential V_{wire}.
In case of more than one wire, there is a coupling capacitance between all conductors. For now, consider a set of two parallel conductors as shown in Fig. 3.11(b). With s being the separation between the two wires, h again the height above the plane and r_{w} the radius of each wire, the capacitances per meter are expressed by (3.19) and (3.20) [59]. This also applies for twisted pair cables.

$$C'_{\text{GND}} = C'_{11} = C'_{22} = \frac{2\pi\varepsilon_0}{ln(\frac{4h^2}{r_{\text{w}}s})} \tag{3.19}$$

$$C'_{12} = \frac{2\pi\varepsilon_0 \cdot ln(\frac{2h}{s})}{ln(\frac{4h^2}{r_{\text{w}}s})ln(\frac{s}{r_{\text{w}}})} \tag{3.20}$$

The capacitance matrix $\mathbf{C}_{\text{2wires}}$ (also termed electrostatic induction matrix) is

$$\mathbf{C}_{\text{2wires}} = \begin{bmatrix} C_{\text{GND}} + C_{12} & -C_{12} \\ -C_{12} & C_{\text{GND}} + C_{12} \end{bmatrix}$$

The charges at each wire relate to the wire potentials V_1 and V_2 via (3.21).

$$\begin{pmatrix} Q_1 \\ Q_2 \end{pmatrix} = \begin{bmatrix} C_{\text{GND}} + C_{12} & -C_{12} \\ -C_{12} & C_{\text{GND}} + C_{12} \end{bmatrix} \cdot \begin{pmatrix} V_1 \\ V_2 \end{pmatrix} \tag{3.21}$$

Here, $\mathbf{C}_{\text{2wires}}$ is symmetric because the wires are at same distance above the ground plane. (This is also the case for twisted pair cables where the average distance to the ground plane is equal.) If the wire's potentials are equal, so are the induced charges. If the potentials are of inverse sign, the charges are too. If the wire potentials are different, the charges will be distributed according (3.21). Measured far from the cable harness, the captured radiated emission is proportional to the sum of the wire charges $Q_1 + Q_2$.

$$\begin{aligned} Q_1 + Q_2 &= (C_{\text{GND}} + C_{12}) \cdot V_1 - C_{12} \cdot V_2 - C_{12} \cdot V_1 + (C_{\text{GND}} + C_{12}) \cdot V_2 \\ &= C_{\text{GND}} \cdot (V_1 + V_2) \\ Q_1 + Q_2 &= 2 \cdot C_{\text{GND}} \cdot \frac{V_1 + V_2}{2} \end{aligned} \tag{3.22}$$

It is interesting to observe that $Q_1 + Q_2$ is no function of the coupling capacitance between the wires C_{12}. As expected, the sum of charges and therefor the E-field of the wire assembly is proportional to the common-mode voltage at the harness $V_{\text{CM}} = (V_1 + V_2)/2$. Differential-mode voltages $V_1 = -V_2$ cause no radiation.

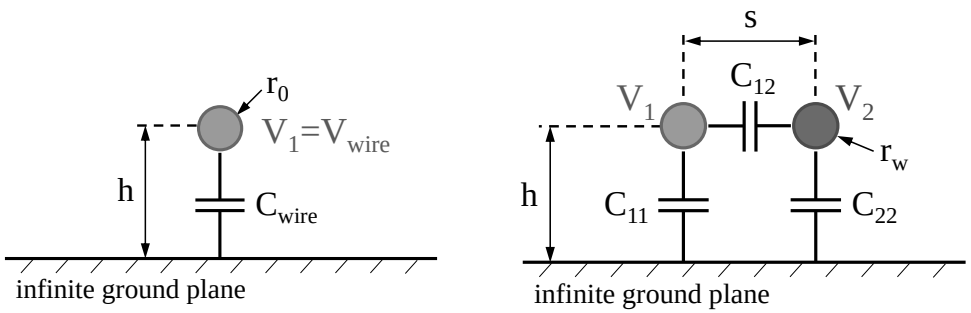

(a) A single wire of radius r_0 above an infinite ground plane. The capacitance to ground C_{wire} can be calculated by (3.1). The signal voltage at the wire V_1 equals the equivalent source voltage V_{wire}.

(b) Two parallel wires of same radius r_{w}. The capacitances are given by (3.19) and (3.20). Only if $r_{\text{eq}} = \sqrt{r_{\text{w}} s}$ the equivalent line potential V_{wire} becomes $V_{\text{CM}} = (V_1 + V_2)/2$.

Figure 3.11.: Capacitive coupling between wires and ground plane

To simplify the analysis it is a common approach to replace tight cable harness by an equivalent single wire (remember Fig. 2.7 of the introduction Chapter 2.3.1). The E-field produced by the single-wire equivalent holding the charge $Q_1 + Q_2$ is proportional to V_{CM} only if the equivalent single-wire radius $r_{\text{eq,2wires}}$ fulfills (3.23), which is gained by combining (3.1) and (3.19).

$$\begin{aligned} Q_1 + Q_2 = C_{\text{eq,2wires}} \cdot \frac{V_1 + V_2}{2} \qquad & C_{\text{eq,2wires}} \equiv C_{\text{wire}} \\ \text{if} \qquad & r_{\text{eq,2wires}} = r_0 = \sqrt{r_{\text{w}} s} \\ \text{where} \qquad & r_{\text{w}} = r_1 = r_2 \end{aligned} \tag{3.23}$$

The value of $r_{\text{eq,2wires}}$ is equal[4] to that obtained in [47] although the intention behind the derivation is different! Here, it was *defined* that the equivalent radius should satisfy that the electrostatic field originating from the single-wire equivalent is proportional to V_{CM} of the replaced bundle, which again was *defined* to be $V_{\text{CM}} = (V_1 + V_2)/2$ (rather than simply $V_1 + V_2$). The referenced work on the contrary defines that $r_{\text{eq,2wires}}$ should satisfy $C_{11} || C_{22} = 2C_{\text{GND}}$ being equal to C_{wire} and it is *assumed* without proof that this will lead to emissions proportional to V_{CM}. Furthermore, they do not include the capacitive coupling between adjacent wires to the derivation. This work does, but also shows by (3.22) that for the radiated electric near-field it has no impact.

[4] It is not precisely equal because [47] additionally respects the wire's coating, but the appearance of the formula $r_{\text{eq}} = \sqrt{rs}$ is the same. As the analytic results in this thesis align well with the measurements, it is assumed that in practice the coating is negligible. Though, reading [63] raises the idea that things could be different when coated wires couple to uncoated ones.

3.5.2. Near Field Coupling as Function of the Wire's Potential

The preceding section clarified that low-frequency electric near field coupling is proportional to charges, which are linked to wire potentials (or voltages) via capacitances. It was shown on the example of a wire pair that the measured antenna voltage V_{rod} induced by a bundle is proportional to the sum of the wire charges. By clever definition of an equivalent single-wire radius $r_{\text{eq,2wires}}$, the sum of charges at the wire pair - and hence V_{rod} - could be expressed proportional to V_{CM}. Now, the relation between charges Q, wire potentials V and antenna voltage will be further examined.
For this work, measurements were conducted to compare the antenna voltage V_{rod} induced by a single wire, to that of two twisted wires of the same type, i.e. a twisted wire pair (TWP). (For electrostatic considerations the twisting is irrelevant because it mainly affects the magnetic field but the low-frequency ALSE measurement result is a function of the electric near-field.) The TWP can be replaced by an equivalent single wire of radius $r_{\text{eq,TWP}}$, which corresponds to $r_{\text{eq,2wires}}$ of (3.23). During the measurements, the two wires of the TWP where either both supplied with $1\,\text{V}$ (termed 'both active'), one supplied while the other was unconnected, i.e. floating, or one supplied while the other wire was grounded to $0\,\text{V}$. Table 3.5 lists the measured V_{rod} for each configuration. Additionally, (3.1) and (3.19) - (3.21) were applied to obtain the induced charges from the wire voltages and geometry. Clearly, the analytically derived sum of the wire charges $\sum Q$ is proportional to the measured antenna voltage!
Furthermore, the listed results allow following interesting observations which are visualized by Fig. 3.12 and Fig. 3.13:

- At first glance, it seems logical that the operation (with same amplitude and phase) of two close-by wires at a time, instead of only one, as illustrated by Fig. 3.12(a), would double the emitted E-field. This is not the case! In fact the voltage measured at the rod antenna due to capacitive coupling, V_{rod}, does hardly change! The electric field is caused by charges, so the total amount of charges $Q = C \cdot V$ on the harness needs to

Table 3.5.: A single $1.5\,\text{m}$ wire of $r_{\text{w}} = 1\,\text{mm}$ compared to one TWP with a wire separation of $s = 3\,\text{mm}$ ($r_{\text{eq}} = 1.7\,\text{mm}$) located $h = 0.05\,\text{m}$ above the ground plane. Capacitances are calculated by (3.19) and (3.20), charges according (3.21). Correlation of the calculated charges and the measurement result as function of the wires' potential.

Configuration	V_1 [V]	V_2 [V]	Q_1 [pC]	Q_2 [pC]	$\Delta(Q_1 + Q_2)$	ΔV_{rod} (measured)
Single wire	1		18.1		reference	reference
Both active	1	1	10.2	10.2	$+1.1\,\text{dB}$	$+1\,\text{dB}$
One floating	1	0.8	18.1	0.0	$0\,\text{dB}$	$-0.3\,\text{dB}$
One grounded	1	0	43.1	-32.8	$-4.9\,\text{dB}$	$-5\,\text{dB}$

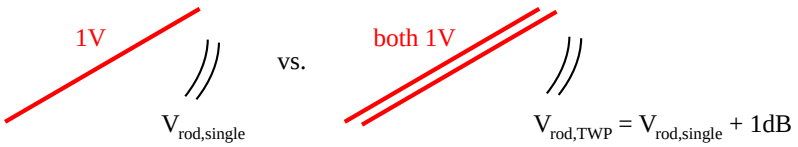

(a) Both wires of the TWP active: V_{rod} doesn´t double, it is only slightly increasing! Compare to Fig. 3.13(a)

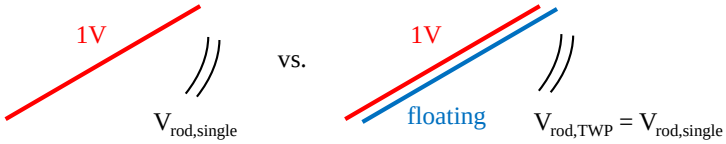

(b) One wire of the TWP floating: The second wire has no impact on V_{rod}! Compare to Fig. 3.13(b)

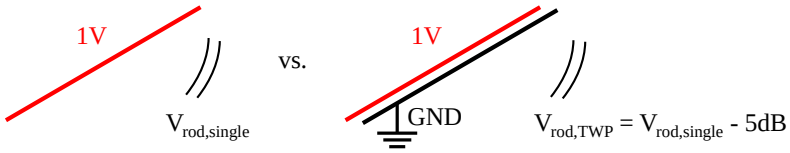

(c) One wire of the TWP grounded: V_{rod} decreases significantly, but it is not exactly halved! Compare to Fig. 3.13(c)

Figure 3.12.: Visualization of the results from Table 3.5: Antenna voltage $V_{\text{rod,single}}$ due to a single wire in comparison to that of a TWP for the listed configurations.

be considered. In the presented case, the potentials $V_1 = 1\,\text{V}$ and $V_{\text{CM}} = (1\,\text{V} + 1\,\text{V})/2$ (following the definition of the preceding Chapter) are equal. The slight increase of V_{rod} is due to the capacitance deviation between $C_{\text{singleWire}}$ and $C_{\text{eq,TWP}}$ proportional to $ln(\frac{2h}{r_{\text{w}}})/ln(\frac{2h}{r_{\text{eq,TWP}}}) = +1.1\,\text{dB}$. Likewise, ΔV_{rod} could also be explained by the slightly different (equivalent) wire radii.

- Again related to Fig. 3.12(a) another close-by assumption is, that because the single wire's potential V_1 is equal to V_{CM} of the TWP, the received voltage V_{rod} should be unchanged. Though, this is only true if $r_{\text{w}} \equiv r_{\text{eq,TWP}}$, i.e. if the sum of wire charges stays constant. Otherwise, ΔV_{rod} is not proportional to ΔV_{wire}!
- Floating wires acquire no charge. They take on the local field potential and by this do hardly impact the radiated field, see Fig. 3.13(b). The potential the wire floats to can be calculated by (3.24) according the capacitance divider from Fig. 3.11.

$$V_2 = \frac{C_{12}}{C_{12} + C_{22}} = \frac{C_{12}}{C_{12} + C_{\text{GND}}} \tag{3.24}$$

- If one wire is at ground potential, as shown by Fig. 3.12(c), it will have a certain shielding effect, because to hold $0\,\text{V}$ it has to acquire a negative charge, compensating the field of the active wire. The resulting electric field close to the harness is illustrated by Fig. 3.13(c). The reduction in V_{rod} relative to both wires being active is proportional to the change in V_{CM}, namely $-6\,\text{dB}$, but relative to the single wire it is less.

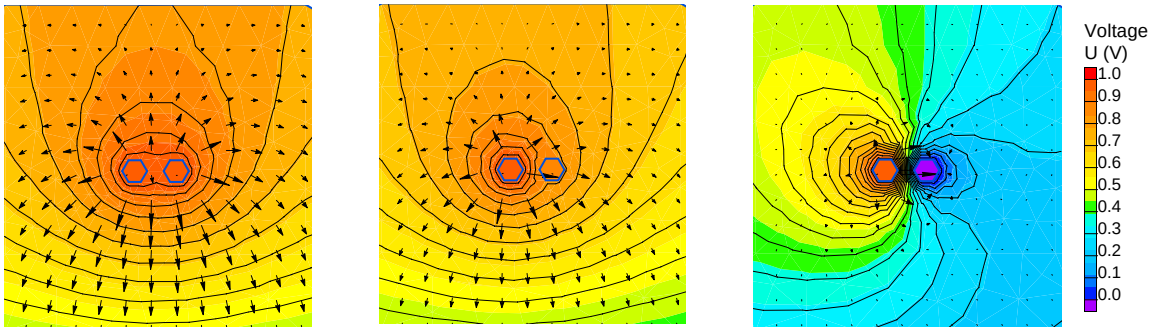

(a) equal potential (b) right wire floating (c) right wire grounded

Figure 3.13.: Colormaps of the electrostatic voltage potential with equipotential lines and vectors of electric field (scaled to maximum field) for two parallel wires of $1\,\mathrm{mm}$ radius $50\,\mathrm{mm}$ above a ground plane (located on the far bottom - not visible). Plots prepared with Quickfield [64]
(a) Both wires are at same potential.
(b) The right wire is floating, hence takes on the local voltage potential. The field distribution is hardly affected.
(c) The right wire is grounded. It shields the field produced by the left wire.

3.5.3. Application to Common Driver Topologies

It was noted in the introduction that it is difficult to predict system level RE of an IC because the device could be used in different ways. Fig. 3.14 shows three ways to use the same single-ended IC driver to operate the same load. From IC's point of view the applications are identical. The ALSE test results, however, would be different. That is because not the IC's output signal, but the CM voltage on the harness is the source of emission (considering only electrostatic near field coupling). Taking the rod antenna voltage V_{rod} induced by the single wire configuration of Fig. 3.14(a) as reference, one could assume that the received voltage is halved when using a TWP as in Fig. 3.14(b), as $V_{\mathrm{CM}} = V_1/2$ in that case. This is almost true, but not exactly, because the additional capacitive coupling between the wires of the TWP has to be taken into account. In other words, the equivalent radius of the TWP $r_{\mathrm{eq,TWP}}$ is not equal the radius of the single wire. Similar to the comparison given in Table 3.5, the reduction of V_{rod} will be slightly less than $6\,\mathrm{dB}$, whereas the exact value depends on the wire separation.
In Fig. 3.14(c) two drivers of the same type are used to drive two loads in parallel with same amplitude and phase[5]. The combined harness consists of two TWP, which are very close together. The coupled antenna voltage is proportional to the overall harness CM voltage, which is again $V_1/2$ as in Fig. 3.14(b). However, again similar to Table 3.5, scenario (b) and (c) will not yield the same emission reading, because - again - the corresponding capacitances are different, or in other words, the equivalent radii of the harnesses are not equal.

[5]This is of course a very theoretical assumption. In practice it is close to impossible to perfectly align CM distortions of different drivers, so RE will notably increase when multiple devices are operated in parallel.

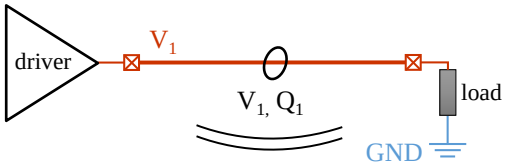

(a) Single-ended driver with locally grounded load. The harness consists of a single wire with radius r_1. V_{rod} is directly proportional to V_1.

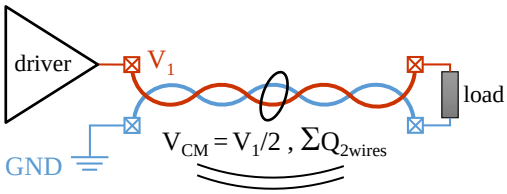

(b) Single-ended driver with load grounded at the driver side utilizing a TWP. V_{rod} is proportional to $V_{CM} = (V_1 + 0)/2 = V_1/2$.

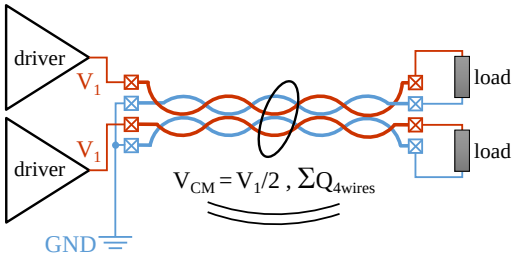

(c) Two single-ended drivers operating in parallel. The harness consists of two close-by TWP. V_{rod} is proportional to $V_{CM} = (V_{CM1} + V_{CM2})/2 = V_1/2$, but $r_{eq,2xTWP} \neq r_{eq,TWP}$.

Figure 3.14.: The same single-ended IC driving the same load can yield very different V_{rod} readings. V_{rod}(b) is about - but not exactly - half V_{rod}(a), V_{rod}(c) is about - but not exactly - equal to V_{rod}(b).

3.6. ALSE Simulation Circuit for Simple Harnesses

Before proceeding with the investigation of the electric field originating from a more complex cable bundle, the so far obtained results should be examined on circuit level. Above electrostatic calculations prove that for low frequencies the 'radiated' emission of a wire is a matter of capacitive coupling. The whole ALSE setup can be expressed by only three capacitances which are illustrated in Fig. 3.15(a):

- C_{wire} being the capacitance between the wire (or the single-wire equivalent of the harness) and the ground plane,
- $C_{wire\text{-}rod}$ to represent the capacitive coupling between (equivalent) wire and the rod receiver antenna, and finally
- C_{rod} which is the capacitance between the vertical rod antenna and the ground plane.

The value of C_{wire} determines the amount of charges collected at the harness and as a consequence the equivalent line potential V_{wire}, which is - by definition of the equivalent radius given in Chapter 3.5.1 - equal to V_{CM}. In practice, V_{CM} is either measured or simulated (applying a model of the harness which includes its capacitance towards ground) so that in a circuit to simulate the low-frequency coupling, the harness can be directly replaced by a voltage source with amplitude (and phase) of V_{CM}. A respective simulation circuit is given by Fig. 3.15(b). V_{CM} is the input to the radiation model, V_{rod} the desired output.
The electrostatic coupling factor (3.16) can now be expressed similar to (3.24) as the ratio between $C_{wire\text{-}rod}$ and C_{rod} (3.25). The capacitance between the rod receiver antenna of

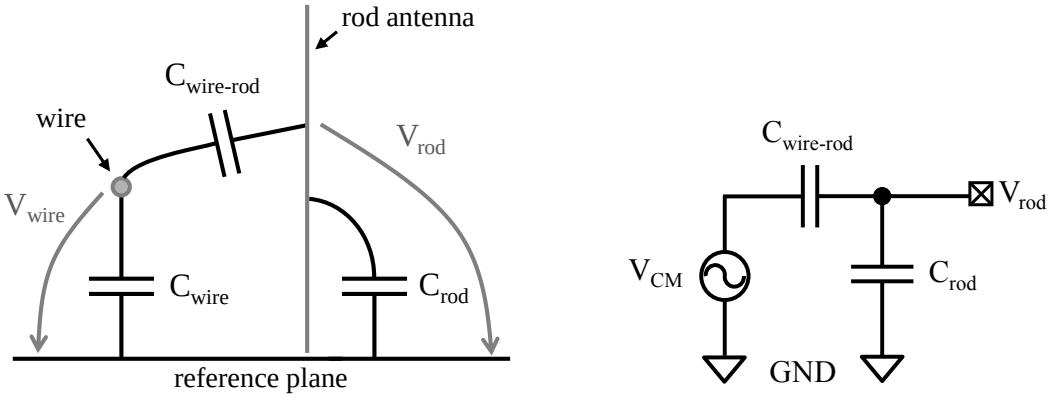

(a) Physical representation of the capacitive coupling between the (equivalent) wire and the rod receiver antenna. ©2018 IEEE [58]

(b) Circuit interpretation of the left figure. The potential at the cable equals V_{CM}.

Figure 3.15.: Illustration of the capacitive coupling between harness and rod receiver antenna.

length h_{rod} and radius r_{rod} and the ground plane can be calculated by (3.26) [65]. For e.g. $r_{\mathrm{rod}} = 5\,\mathrm{mm}$ the equation yields $C_{\mathrm{rod}} = 10.5\,\mathrm{pF}$.

$$k_{\mathrm{cap}} = \frac{C_{\text{wire-rod}}}{C_{\text{wire-rod}} + C_{\mathrm{rod}}} \tag{3.25}$$

$$C_{\mathrm{rod}} = \frac{2\pi\varepsilon_0 \cdot h_{rod}}{ln(\frac{h_{rod}}{r_{rod}})} \tag{3.26}$$

As the capacitance between wire and rod antenna $C_{\text{wire-rod}}$ is significantly smaller than the rod´s self-capacitance towards ground C_{rod}, the latter dominates k_{cap} in (3.25). Assuming, for instance, the value $C_{\text{wire-rod}} = 52\,\mathrm{fF}$ from Table 3.6 for the infinite ground plane and the values $r_{\mathrm{rod}} = 5\,\mathrm{mm}$ and $10\,\mathrm{mm}$, this results in $C_{\mathrm{rod}} = 10.5\,\mathrm{pF}$ and $12.1\,\mathrm{pF}$ respectively, i.e. a deviation of $1.2\,\mathrm{dB}$, and further $k_{\mathrm{cap}} = -46.2\,\mathrm{dB}$ or $-47.4\,\mathrm{dB}$, which equals the deviation of the values for C_{rod}. In other words, the change of the coupling factor Δk_{cap} approximately relates to a change of the ($1\,\mathrm{m}$ long) rod antenna‘s radius from $r_{\mathrm{rod},1}$ to $r_{\mathrm{rod},2}$ according (3.27). This is in agreement with the investigations already presented in Fig. 3.5, given that the antenna is terminated with high impedance.

$$\Delta k_{\mathrm{cap}} \approx \frac{ln(1/r_{\mathrm{rod},1})}{ln(1/r_{\mathrm{rod},2})} \tag{3.27}$$

The value of the coupling capacitance $C_{\text{wire-rod}}$ that correlates to a given k_{cap} can be obtained by rearranging (3.25) to (3.28).

$$C_{\text{wire-rod}} = \frac{k_{\mathrm{cap}} \cdot C_{\mathrm{rod}}}{1 - k_{\mathrm{cap}}} \tag{3.28}$$

By 3D simulation (setups from Fig. 3.3 and Fig. 3.4) the capacitances between the elements as sketched in Fig. 3.15(a) where extracted. The capacitance values from simulation are

Table 3.6.: Capacitance values for Fig. 3.15 (single wire of $1.5\,\mathrm{m}$, $r_{\mathrm{eq}} = 1.5\,\mathrm{mm}$). Analytic values by (3.26), (3.28) and (3.14) (infinite ground) or (3.18) (table ground). The deviation in the value of $C_{\text{wire-rod}}$ for the table-shaped ground is due to the difference in C_{rod}.

	infinite ground			table-shaped ground		
	C_{wire}	$C_{\text{wire-rod}}$	C_{rod}	C_{wire}	$C_{\text{wire-rod}}$	C_{rod}
Analytic	18.6 pF	56 fF	10.5 pF	18.6 pF	105 fF	10.5 pF
3D simulation	18.5 pF	52 fF	12.9 pF	18.4 pF	146 fF	12.4 pF

compared to those obtained by the analytically derived coupling factor k_{cap} and (3.28) in Table 3.6. It can be observed, that the non-finite ground plane mainly affects the coupling capacitance between wire and rod antenna!

The circuit in Fig. 3.15(b) will form the core of the ALSE simulation model that will be developed in Chapter 4. Though, it is only useable for *simple* cable harnesses, meaning harnesses which can be replaced with a single-wire equivalent with an equivalent line potential that is independent of the positioning of the original charges within the original harness. This is roughly speaking only true for harnesses consisting of not more than two *unshielded* TWP. The next chapter investigates a more complex case.

3.7. Capacitive Coupling of a Multi-Cable Harness

Note that in Chapter 3.5.1 it was only possible to find a constant i.e. wire potential independent equivalent radius because $C_{11} = C_{22}$, meaning all wires where equally close to the ground plane. The coupling between wires did not impact the final result because it was the same between all conductors, namely C_{12}. In fact, whenever those requirements are not fulfilled, no constant cable bundle equivalent radius or equivalent line potential can be found but they become a function of the wire's potentials.
For only two parallel wires it was simple to obtain the coupling capacitances matrix analytically. When the harness consists of more wires, this soon becomes too complex for practical usage. Given for example six wires, the 6x6 capacitance matrix $\mathbf{C}_{\text{6wires}}$ holds 36 values. Fortunately, there are many (free) software tools available that can be used to calculate the coupling matrix from a cable bundle's cross section. Knowing the capacitance matrix, the charges $\mathbf{Q}$ at each wire can be easily computed by (3.29) where the column vector $\mathbf{V}$ holds the voltage at each wire.

$$\mathbf{Q} = \mathbf{C}_{\text{6wires}} \cdot \mathbf{V} \tag{3.29}$$

The charge at wire 1 for instance equals

$$Q_1 = C_{11}V_1 + C_{12}V_2 + C_{13}V_3 + C_{14}V_4 + C_{15}V_5 + C_{16}V_6 \tag{3.30}$$

where each coupling capacitance is different. In contrast to the preceding chapter, it is not possible to find an universal equivalent line potential which correlates to the received antenna voltage V_{rod} alike $V_{\text{CM}} = \sum \mathbf{V}/2$. Assume one wire was at a certain voltage, like $1\,\text{V}$, while the other five are grounded, i.e. $0\,\text{V}$. If V_{rod} was proportional to the CM voltage at the harness being $\sum \mathbf{V}/(\#wires)$, the reduction in V_{rod} due to five grounded wires would always equal $1/6 = -15.6\,\text{dB}$. This is obviously not the case as visualized by Fig. 3.16: Wires which couple stronger to adjacent conductors radiate less E-field than wires at the outside of the harness. The amount of charge that is needed to maintain the wire potentials is a function of the active wire's capacitive coupling to adjacent wires. The resulting antenna voltage is proportional to the sum of charges collected at the harness $\sum \mathbf{Q}$, not $\sum \mathbf{V}$.

In the typical ALSE setup all wires are bundled to a combined harness, i.e. they are very close together, and the receiver antenna is far away. Hence it is legitimate to assume a single line of charge holding the sum of the six wire-charges $\rho_l = \sum \mathbf{Q}/l$ located at the center of the bundle. This makes the analytic derivation of the emitted E-field simple, because it yields the desired results with a single use (3.18) and does not require to find an equivalent wire capacitance or voltage. Unfortunately this simplification dismisses the location of the receiver antenna relative to the harness.

3.7.1. The Shielding Effect of Adjacent Wires as Function of the Active Wire's Position

The electrostatic E-field emitted by a 3x2 bundle of six $1.5\,\text{m}$ TWP was investigated by calculation applying above statement that it is proportional to $\sum \mathbf{Q}$. The analytic results where compared to measurements and backed up by 3D EM simulation.
Fig. 3.18 shows the experiment setup and the cable bundle used for the measurements. Both strands of one TWP were sourced with the same signal, resulting in a well defined V_{CM}. All other cables were shorted to the ground plane. RE was measured and compared to the that of a single TWP. The procedure was repeated for each TWP. The used numbering of the cables is visible from Fig. 3.16, which gives the cross section of the bundle as it was used for simulation and calculation, i.e. one equivalent wire for each TWP. The 6x6 capacitance matrix $\mathbf{C}_{\text{6wires}}$ was extracted using the free Transmission Line Electromagnetic Modeling Tool Suite (TNT) [66] with cylindrical conductors of $1\,\text{mm}$ radius and a center-to-center separation of $s = 4\,\text{mm}$. The 3D EM simulation setup was similar to Fig. 3.4 but with a bundle of six cylindrical conductors. For the analytic prediction (3.18) was applied which includes the consideration of the table-shaped ground plane.
The resulting graphs in Fig. 3.17 display the coupling factor k_{cap} according the definition of (3.16) as function of the active wire's position as well as the shielding effect due to the adjacent grounded wires in relation k_{cap} of a single $1.5\,\text{m}$ wire as given in Table 3.4, i.e. a reference of $-41\,\text{dB}$ for the results from measurement and calculation and $-39\,\text{dB}$ for the 3D EM simulation.
The results align with what could be expected from the E-field plots given in Fig. 3.16, namely that the near-field of the cable bundle is maximal for wires 4 and 6 at the outside

corners and minimal for wire 2 in the center of the harness. Although not all analytic values precisely fit the measurement results, it is clearly illustrated that the presented approach of simplifying the multi-cable problem to a single wire of equivalent charge and to calculate the 'radiation' by electrostatic means, is suitable to predict the radiated emission reading (at low frequencies) even of complex harnesses. The degree of accuracy is similar to that of 3D EM simulation, whereas for the 3D simulations, the meshing accuracy was kept low to reduce the computation time.

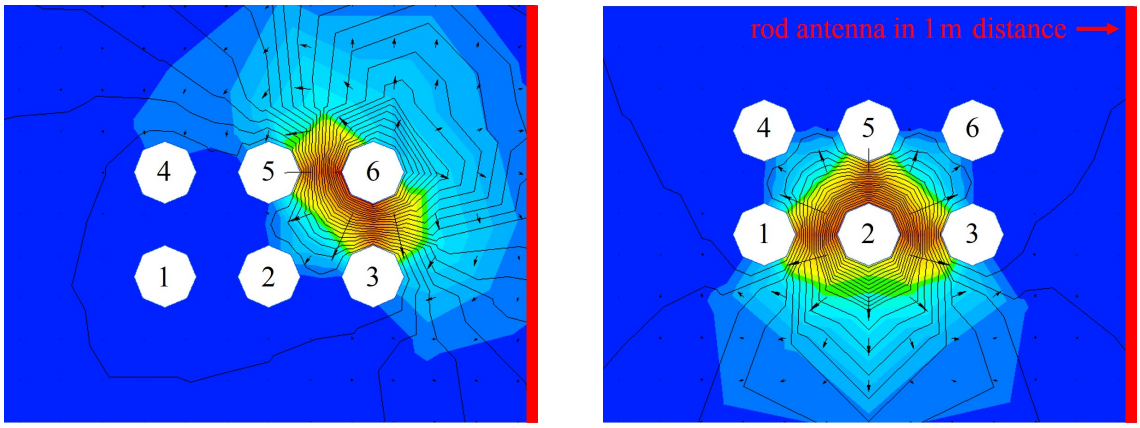

(a) Maximum E-field is measured when wire 6 is active.

(b) The E-field originating from wire 2 in the center of the harness is best shielded.

Figure 3.16.: E-field plots of six conductors above ground (not depicted, in the far bottom). One conductor holds a positive potential, all other are grounded. The E-field would be observed in the far right (not depicted). Values for electrostatic coupling are given by Fig. 3.17. Field plots generated with Quickfield [64]. ©2018 IEEE [58]

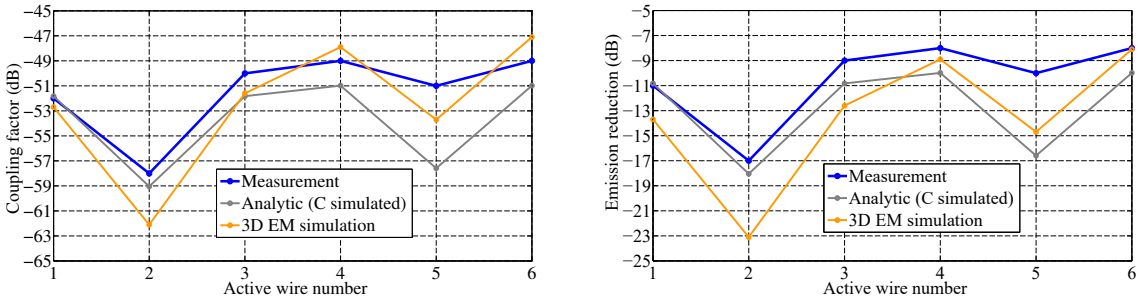

(a) Coupling factor relative to a source of $1\,V_{RMS}$.

(b) Shielding effect due to adjacent grounded wires, relative to the coupling factor of a single TWP.

Figure 3.17.: Near field coupling from a harness of six TWP with one active and five grounded wires as function of the active wire's position. Results from measurement, simulation and analytic prediction. Numbering of wire position is analog to Fig. 3.16.

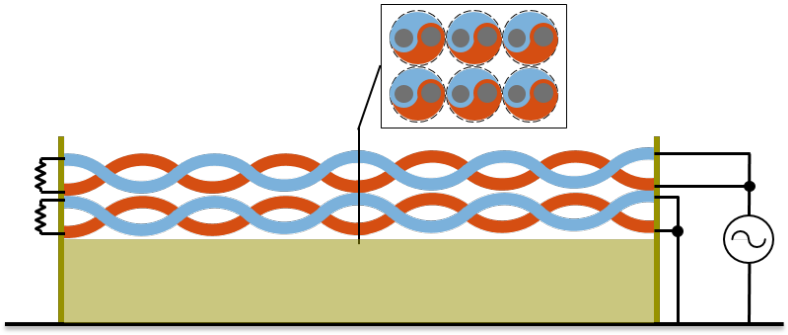

(a) At one side each cable is terminated with $5.6\,\mathrm{k\Omega}$, at the other side 5 of 6 cables are shorted to ground while only one is supplied with a $100\,\mathrm{kHz}$ sine of $1\,\mathrm{V_{RMS}}$.©2018 IEEE [58]

(b) Photo of the cable bundle

Figure 3.18.: Measurement setup for multi-cable radiation: A 3x2 bundle of six TWP of $1.5\,\mathrm{m}$ length, each with an equivalent radius of $1\,\mathrm{mm}$, center-center separation $4\,\mathrm{mm}$, $5\,\mathrm{cm}$ above the ground plane. The cable bundle is on a non-conductive support and is hold tight by non-conductive pillars.

3.7.1.1. Application to Common Driver Topologies

In numerous ALSE measurements related to the work on this thesis it was experienced that idle cables impact the RE measurement result in dependence of their termination impedance, i.e. their potential.
Assume an IC driver with multiple output channels. The ALSE test setup could look like that from Fig. 3.19. Whenever an output is not operative it is common to terminate it with $50\,\Omega$, short it to GND, or make it high-impedance. From electrostatic point of view the first two options mean practically the same. Thus, the cable connected to an output can either be actively driven to a potential, grounded or floating. Table 3.7 summarizes the impact on the radiated field. It applies the finding from Chapter 3.5.2 that floating wires acquire no charge and the results from Fig. 3.17. It is assumed that all signals at active TWP are in same phase. Similar to the discussion of Table 3.5, it can again be observed, that when many close-by wires are at same potential this does hardly increase the field reading. Floating wires have no impact on the measurement result at all, but grounded wires can drastically decrease it. Hence, for lowest system level RE, an idle IC output should always be terminated with low impedance towards ground!

Table 3.7.: A single $1.5\,\mathrm{m}$ TWP of $r_{\mathrm{eq}} = 1\,\mathrm{mm}$ at $1\,\mathrm{V}$ compared to six identical TWP with a separation of $s = 4\,\mathrm{mm}$ where either all or only one TWP holds $1\,\mathrm{V}$. V_{rod} is proportional to $\sum \mathbf{Q}$. ΔV_{rod} is given relative to the voltage induced by a single TWP.

Configuration	$\sum \mathbf{Q}$ [pC]	ΔV_{rod} (analytic)
Single wire	18.1	reference
All active	26.4	$+3.3\,\mathrm{dB}$
5 of 6 floating	18.1	$0\,\mathrm{dB}$
5 of 6 grounded	2.2 - 5.6	$-18.2\,\mathrm{dB}$ to $-10.1\,\mathrm{dB}$

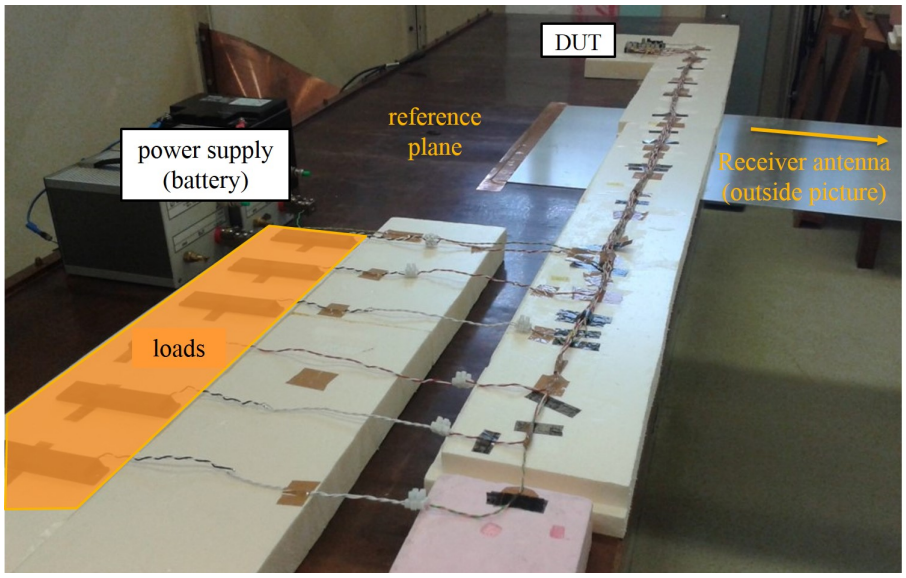

Figure 3.19.: Photo of an ALSE test setup comprising a harness of six TWP connecting the loads plus one TWP as supply line which connects the DUT to the car battery. The latter is neglected in this work, although for specific applications it might impact the measurement result. The rod receiver antenna is to the right, outside of the picture in $1\,\mathrm{m}$ distance from the harness.

3.8. Chapter Conclusion and Summary of Scientific Content

In this chapter the origin of the low-frequency E-field that is captured with the ALSE setup below roughly $3\,\mathrm{MHz}$ was investigated. The root cause for the emission reading is capacitive coupling between the cable harness and the rod receiver antenna, rather than actual radiation due to EM wave propagation. Thus, it can be described by a capacitive divider, resulting in a capacitive coupling factor, which was termed k_{cap}. This factor is practically frequency independent. Similar was already observed in some publications of other authors. In the past, the value of this constant 'radiation' or transmission factor (TF) was obtained by various means of measurement or simulation. The scientifically new contribution of this work is the analytic derivation by applying electrostatic field theory. Furthermore, the fact that electrostatic assumptions yield the correct TF with good accuracy constitutes the mathematical proof that capacitive coupling is the sole relevant coupling mechanism in the considered frequency range.
Various impact factors on direct capacitive coupling, like the ground plane size, cable length and (equivalent) radius where investigated. In the past, this was mostly done with help of 3D EM simulations or analytic models based on electric dipole current radiation. New in this work is, again, the analytic consideration with electrostatics only, i.e. without the need for currents and their distribution.
The intention of this thesis is to finally provide a circuit level simulation model that can be easily included in the daily business of an (integrated) circuit designer. The content of the foregoing chapter delivers an important milestone, which can be formulated as rule of thumb: Knowing that direct capacitive coupling is mostly independent of the cable type, it can be stated that the voltage received by the rod antenna is roughly $40\,\mathrm{dB}$ less than the common-voltage on the cable harness. Because the rod antenna is exactly $1\,\mathrm{m}$ long, the value of the received voltage V_{rod} equals the $\mathrm{dB}\mu\mathrm{V/m}$ reading at the EMI receiver connected to the rod antenna.

$$RE_{\mathrm{ALSE}<3\,\mathrm{MHz}}\,[\mathrm{dB}\mu\mathrm{V/m}] = (V_{\mathrm{CM,harness}}\,[\mathrm{dB}\mu\mathrm{V}] - 40\,\mathrm{dB}\mu\mathrm{V}) \cdot 1/\mathrm{m} \tag{3.31}$$

The observations made so far give evidence that this value holds within typical measurement and simulation uncertainties. For devices operating at low frequencies where the critical emission frequency range is e.g. the MW or AM radio band up to $1.8\,\mathrm{MHz}$, such rule of thumb enables to forecast electromagnetic compatibility already during early design phases even without precise simulations or a fabricated prototype.
However, the above value is only valid as long as the cable harness can be expressed as an equivalent single wire. This is roughly speaking only true for harnesses consisting of not more than two *unshielded* TWP. In case of more complex multi-cable harnesses the TF is not constant but a function of the active wire's position(s) within the harness. Then, the electrostatic coupling cannot be expressed through an equivalent line potential but only via the sum of charges at the harness. This is inconvenient for a circuit designer, who usually works with voltages and currents, not charges. It means that a test bench to simulate RE of a complex cable harness must include the coupling between all wires.

However, as was discussed in the introduction, it is unlikely that a circuit designer knows the exact parameters of the harness which will be used in the (system level) ALSE test. Therefore, considering the impact of a multi-cable harness during circuit level simulation is seldom productive. An IC or system architect should nonetheless be aware of the fact, that measurements conducted with harnesses composed of many cables may yield radiation readings significantly below that of single-wire simulations. This shielding effect was noted in literature before and the results of this work align well with what was already published, specifically Chapter 3.5.1 with [47] and Chapter 3.5.2 with [46], whereas the cited works attend to frequencies above $30\,\mathrm{MHz}$ and - as usual - are based on electric dipole sequences for calculating the radiated field. So, similar to the single-wire TF, the novel scientific contribution of this work is not to reveal that certain mechanisms exist, but to show that they are also relevant at very low frequencies, where they can be analytically described by electrostatic means. Compared to existing works the presented approach is mathematically simpler and easier to comprehend as it requires no knowledge of EM field theory.

It needs to be stated at this point, that the emission readings in $\mathrm{dB}\mu\mathrm{V/m}$ displayed by an EMI receiver are referenced to $1\,\mu\mathrm{V_{RMS}}$! Hence, to prevent errors of $3\,\mathrm{dB}$ when relating calculation results from equations like (3.31) to measurement results, voltages need to be given as RMS values rather than peak values ($V_{\mathrm{RMS}} = V_P/\sqrt{2}$). Chapter 5 will go in more details on characteristics of an EMI receiver and ways to model them. Before that, the ALSE simulation test bench which delivers the input signal to the EMI receiver model is developed in the next chapter.

4. An Universal Circuit Model to Simulate ALSE RE up to 30 MHz

In the introducing Chapter 2 it was described that the ALSE test setup offers many degrees of freedom concerning for instance the size and shape of the ground plane and the ALSE itself and especially for the way how the elevated bench is grounded. So far, this thesis regarded the ALSE test setup according the automotive CSIPR 25 Ed.4 [1] standard. Another widely used setup to evaluate RE is that defined in the military MIL-STD-461G [32]. Fig. 4.1 once more highlights the differences of the setups for RE measurement with the rod antenna. The counterpoise which provides the reference potential for the antenna output has to be extended to the grounded tabletop when tests are performed according CISPR 25 but should be grounded via the shield of the coaxial cable and unconnected from the table according MIL-STD-461G. Those varieties in standard-compliant ALSE test setups result in significant deviations in RE measurement results between $10\,\mathrm{MHz}$ to $30\,\mathrm{MHz}$ (pinpointed by measurement and simulation for instance in [22, 33, 67, 28]). None of these results is more 'correct' than others. A circuit level model of the ALSE setup should nonetheless be valid for the whole range of setup variances. In this respect, the intention of this work was to provide an universal simulation model that can be adjusted to reflect a specific ALSE setup by a set of sub-circuits and parameters. These will be described in detail within the following Sections 4.1 and 4.2. Afterward, in Section 4.3 the proposed model is evaluated by comparing simulation results for different configurations to reference data recently published by other authors.

The simple circuit in Fig. 3.15(b) of the preceding chapter describes electrostatic, i.e. capacitive coupling only which is insufficient to model the complete frequency range observed with the rod antenna. As was discussed in the introduction in Chapter 2.2, for frequencies higher than approximately $3\,\mathrm{MHz}$ an additional 'radiation path', termed transverse electromagnetic (TEM) mode coupling, needs to be respected. Fig. 4.2 gives an overview of the simulation testbench that will be topic of this chapter. In principle, it is a composition of the ideas and modeling approaches introduced in Chapter 2.2. The 'radiated' emissions couple by two different means from the cable harness to the receiver antenna *but both originate from voltages induced by the cable*. The total voltage received by the rod antenna V_{rod} is the sum of the voltage due to direct capacitive coupling V_{cap} and the indirectly induced V_{TEM} due to the moving potential of the node *counterpoise GND* (4.1).

$$V_{\mathrm{rod}} = V_{\mathrm{CM}} \cdot k_{\mathrm{cap}} + V_{\mathrm{counter,GND}} \cdot k_{\mathrm{TEM}} = V_{\mathrm{cap}} + V_{\mathrm{TEM}} \tag{4.1}$$

The signal delivered to the EMI receiver is the voltage at the output node *ALSE out*. Note the shift in the reference level due to the (active) output stage of the rod antenna.
It should be noted at this point, that conventional rod receiver antennas are usually equipped with an active output amplifier to achieve an antenna transmission factor which is constant over frequency and independent of the load (coaxial cable + EMI receiver) connected to the antenna output. For the presented simulation model this stage is assumed to be ideal (in contrast to other works), i.e. the voltage at the EMI receiver input equals the

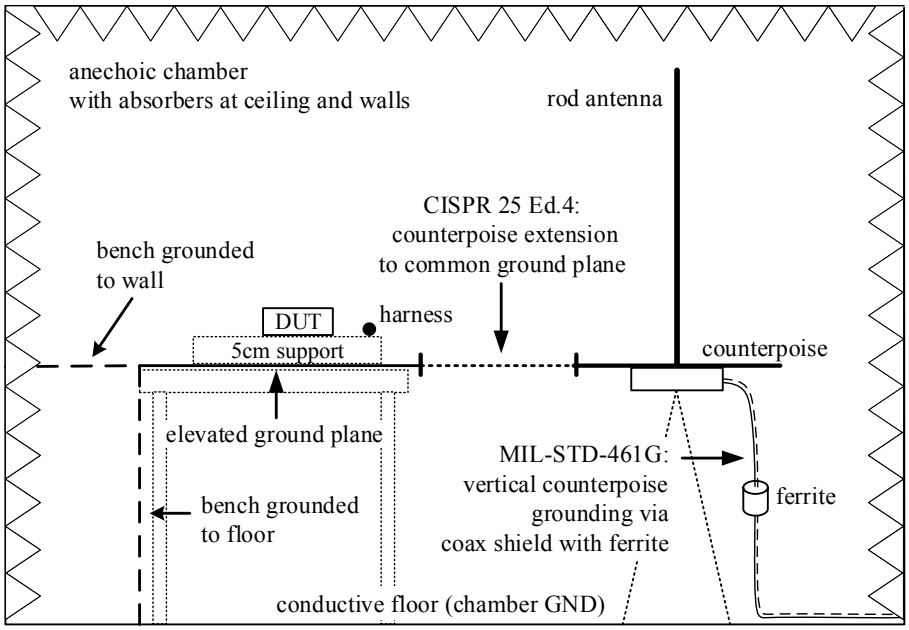

Figure 4.1.: Sketch of the ALSE test setup with the rod antenna, exhibiting common bench grounding schemes and different means of connecting the antenna counterpoise in dependence of the used standard.

voltage at the rod antenna. The coaxial cable connecting the antenna output to the EMI receiver is not modeled.
The EMI receiver will be discussed in Chapter 5. An electrical model would consist of a $50\,\Omega$ input impedance but is irrelevant due to the ideal antenna output buffer.

With increasing frequency the simplified 'reference plane' used so far needs to be separated into the reference potential of the wire, which is the table, and that of the rod antenna, which is the counterpoise. Respectively, the nodes *table GND* and *counterpoise GND* are introduced in Fig. 4.3. This top-level view includes two subcircuit blocks for the cable harness and the elevated bench which are detailed in Sections 4.1 and 4.2 respectively.
Similar to Fig. 4.2 before, Fig. 4.3 depicts the two coupling modes now on circuit level. The voltage received by the rod antenna is the sum of the voltages V_{cap} due to capacitive coupling (corresponds to V_{rod} in Chapter 3) and V_{TEM} invoked by TEM mode coupling. In accordance to (3.25) and (3.16) the value of V_{cap} is determined by k_{cap} as the ratio between the capacitive coupling from harness to rod antenna expressed by $C_{\text{wire-rod}}$ (3.28) and the capacitance between rod and counterpoise C_{rod}. During the electrostatic consideration only a single (equivalent) voltage V_{wire} existed at the harness. Now, the harness is replaced by an equivalent circuit which allows different voltages at all cable ends. The voltages at all cable ends equally contribute to V_{cap}, hence a fraction of $C_{\text{wire-rod}}$ is attached at each node. The antenna voltage originating from TEM mode coupling V_{TEM} is modeled as the voltage at the node *counterpoise GND* weighted by the factor k_{TEM}. Because V_{cap} and V_{TEM} refer to the same *floating* reference node *counterpoise GND* it is evident that k_{TEM} could be expressed

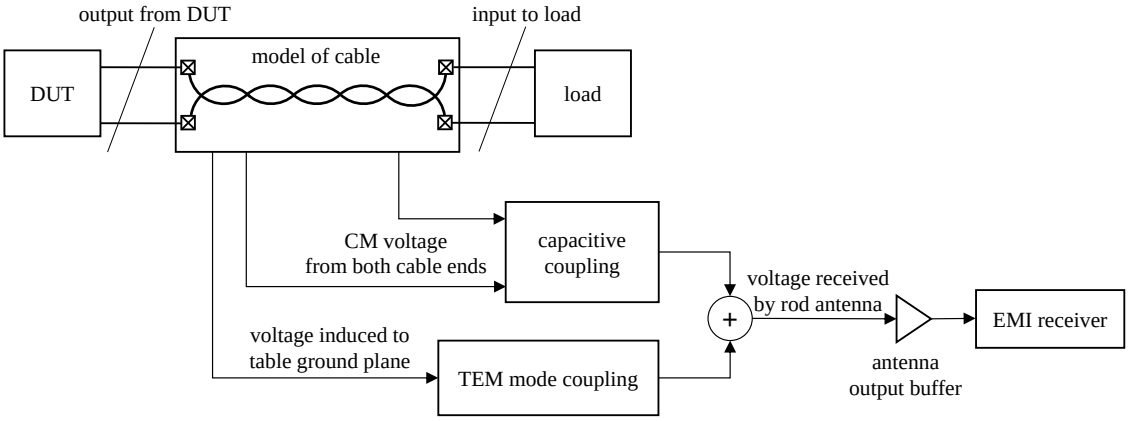

Figure 4.2.: The proposed ALSE RE simulation model depicted by functional blocks. Models of the DUT and the load are not covered in this thesis.

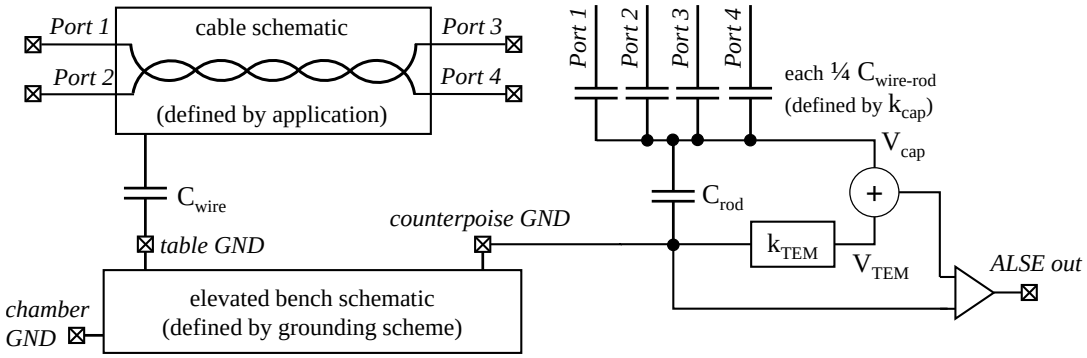

Figure 4.3.: Schematic top-level of the proposed circuit model defining the interface pins of the subcircuits which are discussed in the respective sections. Squares indicate I/O pins.

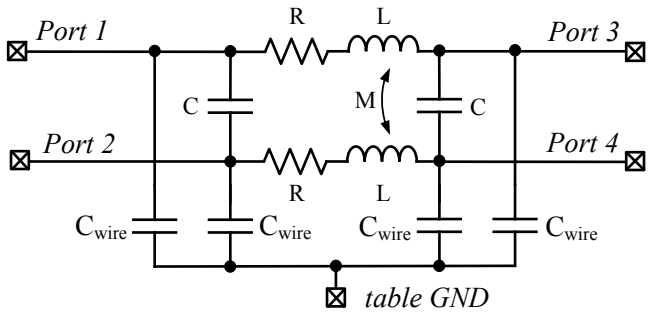

Figure 4.4.: Schematic for a harness consisting of a single TWP. For frequencies as low as 30 MHz such a simple model sufficiently reflects the cable's influence on RE. The specific circuit is object of the application's cable harness. Squares indicate I/O pins.

as function of k_{cap}. A best-match relation was found to be (4.2) by utilizing a parametric sweep (using the circuit simulator Cadence Virtuoso) and comparison of measurement and simulation of the transfer function between DUT output CM voltage and output voltage of the receiver antenna (node *ALSE out* in the schematic of Fig. 4.3). Though, the value and sign of k_{TEM} depend on the grounding of the elevated bench and the counterpoise. For the investigated configurations the respective values of k_{cap} and k_{TEM} are given in Table 4.2 and Table 4.3 of Section 4.3.

$$k_{\text{TEM}} = \pm 5 \cdot k_{\text{cap}} \tag{4.2}$$

4.1. Cable Schematic

A precise model of the cable harness and the attached load, including all kinds of crosstalk, of course are important to accurately simulate the behavior of the DUT. The generation of cable models has been scope of many publications (see Chapter 2.3) and does not add scientific value to this work. Assuming a typical cable inductance of around $1\,\mu\text{H/m}$ and capacitance to the ground plane of $12\,\text{pF/m}$ (compare Table 3.6), the fundamental resonance frequency for a $1.5\,\text{m}$ cable is roughly $f_{\text{res}} = 1/(2\pi\sqrt{LC}) = 31\,\text{MHz}$. For instance, the automotive TWP type FLRY-A 2x $0.5\,\text{mm}^2$ used for the measurement in Fig. 4.9 was resonant at $35\,\text{MHz}$. (This is outside the frequency range of Fig. 4.9 but is visible by the V_{CM} resonance in Fig. 4.10.) For the simulation of RE below $30\,\text{MHz}$ the equivalent circuit used to model the cable harness needs to be precise enough to correctly capture this first resonance. Therefor, in most cases an equivalent circuit as simple as that sketched in Fig. 4.4 is sufficient. Two quantities are important here:

- First, the common-mode voltage at the cable which directly couples to the receiver antenna. Depending on the termination impedance at the cable ends and due to the length of the cable signal resonances or reflections may occur, hence the voltages at both cable ends should be respected to equal terms, as illustrated in Fig. 4.2 and Fig. 4.5. It can be observed from Fig. 4.10 and also from the near-field measurement results shown in [7] that field components around $30\,\text{MHz}$ are radiating from the load side cable end. These would be missed by respecting solely the CM voltage at the DUT side, but are overestimated when only the CM voltage at the load is considered.
- Second, the capacitance C_{wire} between cable harness and ground plane. It determines the voltage that is induced to the bench, which defines the potential of the rod antenna counterpoise and is the stimuli for TEM mode coupling. Besides this important contribution to RE simulation, it should be respected in the circuit model of the cable harness because this additional capacitance towards ground might affect the output signal of the DUT. Note that C_{wire} scales with the length of the harness!

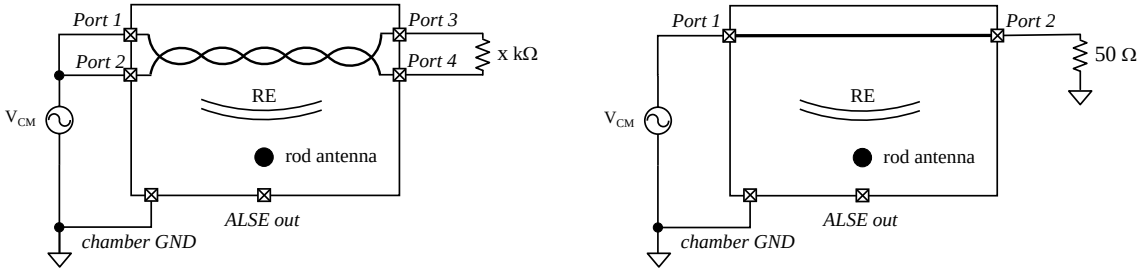

(a) Load without ground connection at TWP cable end, similar to the setups of Fig. 2.4, Fig. 2.5 or Fig. 3.18(a).

(b) Load terminated with $50\,\Omega$ to ground at end of single wire, as defined for the long wire calibration method of CISPR 25 Annex. J [1].

Figure 4.5.: ALSE simulation testbench top views for different types of load termination

4.2. Circuitry for the Elevated Bench

Following [68] the ALSE setup can be modeled by a coaxial TEM transmission line comprised of the elevated bench as center conductor and the shielded room as the outer conductor. In this way the concept of characteristic impedance Z_0 and textbook equations for a two-conductor stripline are used to generate a circuit model for the elevated bench with the chamber floor being the reference conductor *chamber GND*. The following subsections give the equations used to find the respective circuit component values summarized by Table 4.1.

4.2.1. Characteristic Impedance of the Table Sections

The relation between characteristic impedance Z_0 of a *lossless* transmission line and the per-unit-length values of an equivalent LC element is given by (4.3). The dielectric medium inside the chamber is approximated by free space with an effective dielectric constant $\varepsilon_{\text{re}} = 1$ and relative permeability $\mu_r = 1$, which allows to express the inductance per unit length L' and capacitance per unit length C' according (4.4). $\mu_0 = 4\pi \cdot 10^7\,\mathrm{H/m}$ is the magnetic constant (or permeability of free space) and $\varepsilon_0 = 8.854 \cdot 10^{-12}\,\mathrm{F/m}$ is the electric constant.

$$Z_0 = \sqrt{\frac{L'}{C'}} \tag{4.3}$$

$$L' = \sqrt{\varepsilon_0 \mu_0} \cdot Z_0 \qquad \text{and} \qquad C' = \frac{\sqrt{\varepsilon_0 \mu_0}}{Z_0} \tag{4.4}$$

Fig. 4.6(a) shows the dimensions of the elevated bench. The following equations to calculate the characteristic impedance of the sections can be found in [69]. These were empirically derived, hence the right-hand side expressions are unitless. Units are therefor provided in brackets. The table width W_{table} may be $1\,\mathrm{m}$ to $3\,\mathrm{m}$, hence $W/h \geq 1$ and (4.5) accounts. The extension towards the counterpoise should be as wide as the latter, typically

$W_{\text{extension}} = 0.6\,\text{m}$, hence $W/h \leq 1$ and (4.6) accounts. With (4.4) the respective per unit length components can be obtained which need to be scaled by the respective depth of table or extension (compare Fig. 4.6(a))!

$$Z_{0,\text{table}}\ (\Omega) = 120\pi \cdot \left(\frac{W_{\text{table}}}{h} + 1.393 + 0.667 \cdot \ln\left(\frac{W_{\text{table}}}{h} + 1.444\right)\right)^{-1} \tag{4.5}$$

$$Z_{0,\text{extension}}\ (\Omega) = 60 \cdot \ln\left(\frac{8h}{W_{\text{extension}}} + \frac{W_{\text{extension}}}{4h}\right) \tag{4.6}$$

4.2.2. Step in Width

The discontinuity caused by the step in the width of the elevated bench is modeled by a LCL element as depicted in Fig. 4.7. The circuit components are obtained by the below equations given in [70]. Again, these are unitless (or unit-ignoring) empirical relations.

$$C_{\text{dis}}\ (\text{pF}) = \sqrt{W_{\text{table}} W_{\text{extension}}}\left(2.33\frac{W_{\text{table}}}{W_{\text{extension}}} - 3.17\right) \tag{4.7}$$

$$L_{\text{dis}}\ (\text{nH}) = 987 \cdot h \cdot \left(1 - \frac{Z_{0,\text{table}}}{Z_{0,\text{extension}}}\right)^2 \tag{4.8}$$

$$L_{\text{dis,table}} = \frac{L_{\text{table}}}{L_{\text{table}} + L_{\text{extn}}} L_{\text{dis}} \tag{4.9}$$

$$L_{\text{dis,extn}} = \frac{L_{\text{extn}}}{L_{\text{table}} + L_{\text{extn}}} L_{\text{dis}} \tag{4.10}$$

4.2.3. Open Circuit at Floating Table End

The open circuit discontinuity at the counterpoise acts as capacitance C_{open} [69].

$$C_{\text{open}}\ (\text{pF}) = 0.412 \cdot 10^{-12}\left(\frac{W_{\text{extension}}/h + 0.262}{W_{\text{extension}}/h + 0.813}\right)\frac{\sqrt{\varepsilon_0\mu_0}}{Z_{0,\text{extension}}} \tag{4.11}$$

If the counterpoise is isolated from the table the additional open circuit discontinuity at the table edge is described by $C_{\text{open,table}}$ obtained from (4.11) by inserting W_{table} and $Z_{0,\text{table}}$ respectively. The schematic Fig. 4.6(d) is used which also includes the coupling capacitance between table and counterpoise $C_{\text{table-counter}}$ and C_{open} at both ends of the isolated counterpoise. (Here the value of $C_{\text{table-counter}}$ was taken from [22] where it was obtained from 3D simulation. Analytical expressions for gaps in microstrips exist [70] but do not reflect a step in width at the same time.)
Whenever the counterpoise is not floating but vertically grounded to the chamber floor, the resistor R_{counter} in parallel to C_{open} is set to a low-ohmic value.

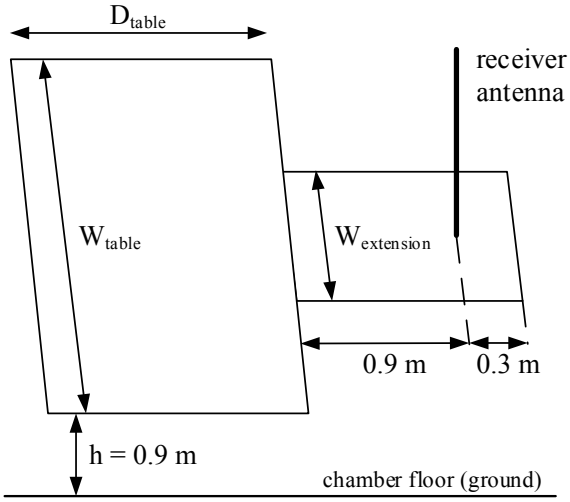

(a) Dimensions of the elevated bench

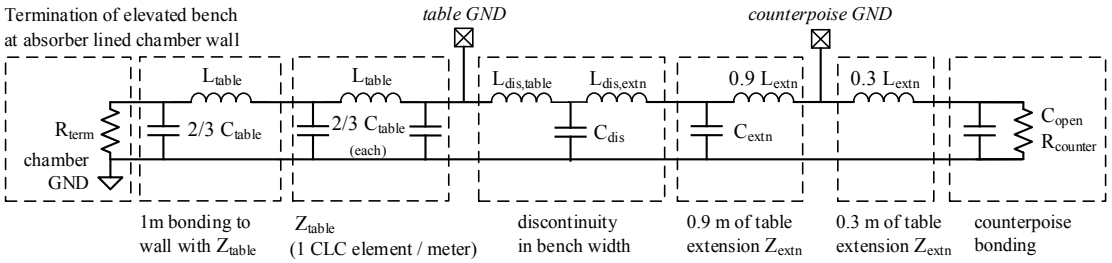

(b) Circuit representation of the elevated bench horizontally bonded to the absorber lined chamber wall.

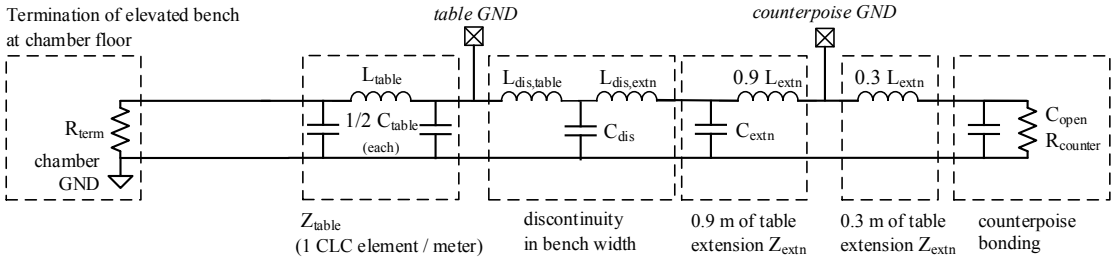

(c) Circuit representation of the elevated bench vertically bonded to the chamber floor.

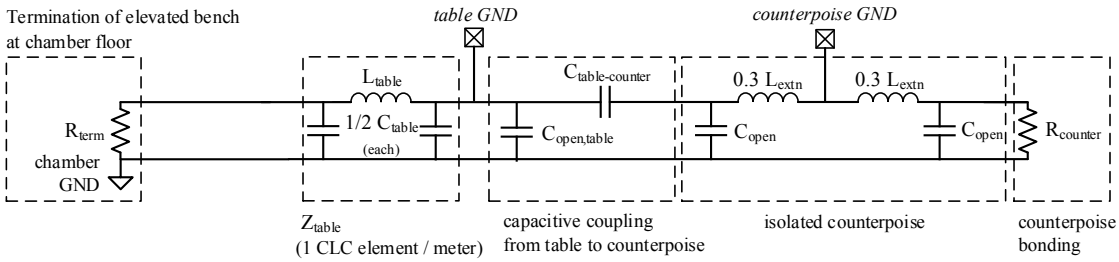

(d) Circuit representation of the elevated bench vertically bonded to the chamber floor and isolated counterpoise. The value of $C_{\text{table-counter}} = 5\,\text{pF}$ was copied from [22] where it was obtained by 3D simulation.

Figure 4.6.: Sketch of the elevated bench and the corresponding circuit representation. The top figure shows the dimensions used to derive the component values of the lower figures.

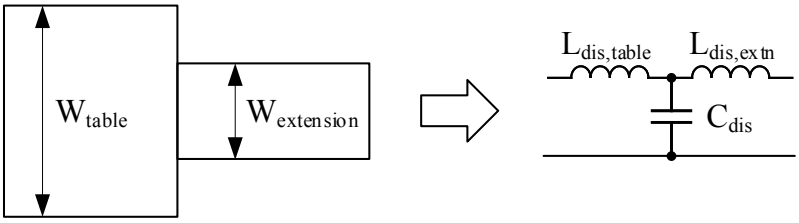

Figure 4.7.: Circuit representation of the step in width from table to extension towards counterpoise [70]

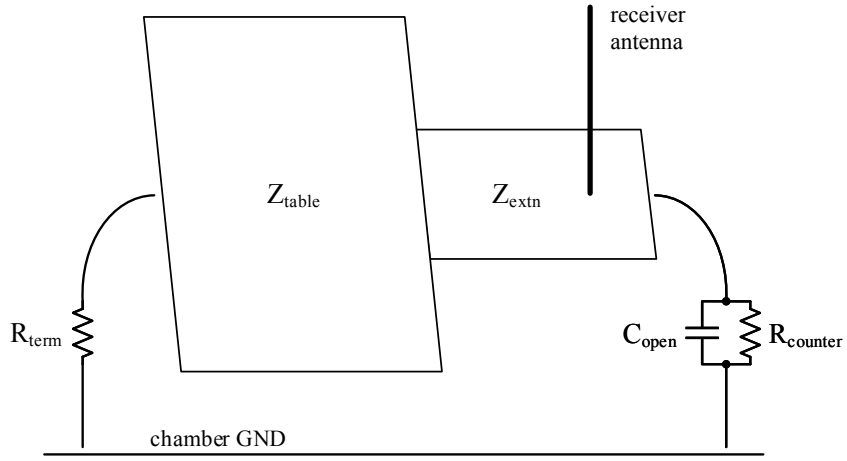

(a) CISPR 25 setup with counterpoise extension to table

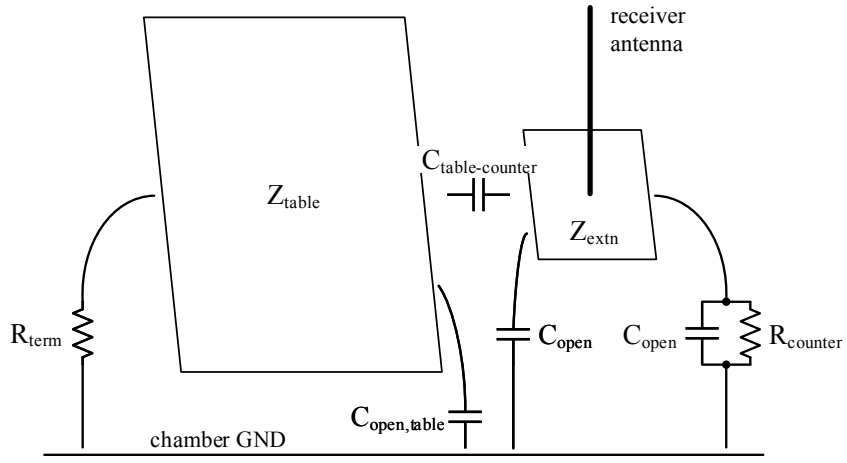

(b) MIL-STD-461G setup with floating counterpoise

Figure 4.8.: Visualization of termination capacitances and resistors used in Fig. 4.6

Table 4.1.: LC component values for the circuit representation of the elevated bench for $W_{\text{extension}} = 0.6\,\text{m}$ and $h = 0.9\,\text{m}$ and the values of W_{table} used for the model validation in Section 4.3.

component		W_{table} 2.5 m	W_{table} 3.0 m	used in
$Z_{0,\text{table}}$	(4.5)	74 Ω	65 Ω	Fig. 4.6(b-d)
$Z_{0,\text{extension}}$	(4.6)	151 Ω		
L'_{table}	(4.4)	245 nH/m	218 nH/m	
C'_{table}	(4.4)	45 pF/m	51 pF/m	
C_{open}	(4.11)	6 pF		
L'_{extn}	(4.4)	499 nH/m		
C'_{extn}	(4.4)	22 pF/m		Fig. 4.6(b,c)
C_{dis}	(4.7)	8 pF	11 pF	
$L_{\text{dis,table}}$	(4.9)	76 nH	86 nH	
$L_{\text{dis,extn}}$	(4.10)	155 nH	197 nH	
$C_{\text{open,table}}$	(4.11)	28 pF	32 pF	Fig. 4.6(d)
$C_{\text{table-counter}}$	[22]	5 pF		

4.2.4. Bench Termination at the Chamber Wall or Floor

It was shown in [71] that the dominant resonances around 20 MHz are originating from reflections at the rear chamber wall where the elevated bench is grounded to. (By 3D simulations using perfect absorbers it is also found in [71] that reflections at the other chamber walls have no impact below 30 MHz.) In the real ALSE these rear wall reflections should be attenuated by absorbers. The absorber performance is emulated by the value of R_{term} in the circuit model. $R_{\text{term}} = 0\,\Omega$ means direct grounding which corresponds to a shielded enclosure without any absorbers. This results in maximum resonance amplitudes. The other extreme is when the termination resistance is equal to the characteristic impedance of the table, i.e. $R_{\text{term}} = Z_{0,\text{table}}$. It means matched conditions and results in no reflections at all. Generally, the absorber's performance is unspecified below 30 MHz but can be expected to be poor[1], hence a low value of R_{term} is a good choice for the simulation model. From [26] and similar publication it can be observed that the rear-wall resonances vary a lot between different chambers. As a consequence, there is no 'correct' value for R_{term}. It should rather be adjusted to fit the characteristics of the chamber under consideration (if there is a specific one). Furthermore, it has significant impact on RE whether the elevated

[1] Compare Fig. 2.1. Additional considerations on the absorber performance are made in [71] based on 3D simulations. Actually, CISPR 25 Ed.4 [1] (Section 4.3.4.2) does not even define a mandatory absorption below 70 MHz. Instead, evaluation of the overall influences of the chamber, including absorbers, ground plane, grounding and others, is specified by comparison to reference RE data, as was already mentioned in Chapter 2.1.

Table 4.2.: Circuit parameters for different cable and load setups. The value of C_{wire} was calculated by (3.1) using a radius of $1\,\text{mm}$ for the $1.5\,\text{m}$ wire or $2\,\text{mm}$ for the CISPR 25 long wire method. $C_{\text{wire-rod}}$ is calculated from (3.28) using $C_{\text{rod}} = 10.5\,\text{pF}$. From [33] it was observed that a floating counterpoise reduces k_{cap} by $20\,\text{dB}$. k_{cap} for the long wire method was extracted from the standard.

test setup	schematic	C_{wire}	k_{cap}	$C_{\text{wire-rod}}$
$1.5\,\text{m}$ TWP with floating load like Fig. 2.4 and Fig. 2.5	Fig. 4.5(a)	$18\,\text{pF}$	0.01 ($-40\,\text{dB}$) (3.31)	$106\,\text{fF}$
$1.5\,\text{m}$ wire with terminated load used in [33]	Fig. 4.5(b)	$18\,\text{pF}$	0.01 ($-40\,\text{dB}$) (3.31)	$106\,\text{fF}$
$1.5\,\text{m}$ wire with terminated load and floating counterpoise [33]	Fig. 4.5(b)	$18\,\text{pF}$	0.01/10 ($-60\,\text{dB}$) from [33]	$11\,\text{fF}$
$0.5\,\text{m}$ wire with terminated load CISPR 25 'long wire method' [1]	Fig. 4.5(b)	$7\,\text{pF}$	0.0036 ($-49\,\text{dB}$) from [1]	$37\,\text{fF}$

bench grounding is realized by vertical or horizontal bonding [25]:
If the table is bonded to the rear chamber wall, schematic Fig. 4.6(b) is used. For this work $R_{\text{term}} = 12\,\Omega$ was chosen. The horizontal bond is respected by an additional $1\,\text{m}$ LC element with the characteristic impedance of the table.
If the bench is vertically bonded to the chamber floor, schematics Fig. 4.6(c) or Fig. 4.6(d) apply. The floor is not equipped with absorbers in the semi-anechoic ALSE, consequently the value of R_{term} needs significantly lower than in above case of bonding towards the absorber-lined wall. On the other hand, the 90 degree bend of the bench disturbs the TEM propagation, hence $R_{\text{term}} > 0\,\Omega$. Accordingly the termination resistance is reduced to $R_{\text{term}} = 4\,\Omega$ for the given examples. Again, this value is chamber specific and needs to be adjusted in particular.

4.3. Simulation Results and Model Verification

In Fig. 4.9 the transmission factor, i.e. the ratio of V_{CM} at the DUT output to $V_{\text{ALSE,out}}$ at the receiver antenna output (see Fig. 4.3), measured in a default CISPR 25 ALSE test setup with $1.5\,\text{m}$ harness similar to Fig. 2.4 is compared to that obtained by simulation with the described circuit model. The used TWP cable was floating at the load end, as in Fig. 4.5(b), and the bench bonded to the chamber wall. The cable-related simulation parameters and the equivalent circuit for the elevated bench were chosen as given in the first rows of Table 4.2 and Table 4.3. (For k_{cap} the rule of thumb (3.31) of Chapter 3.8 was applied.) The values of k_{cap}, k_{TEM} and R_{term} have a critical impact on the simulation result! With the described selection the simulation matches the measurement with deviations of less than $6\,\text{dB}$.

Table 4.3.: Circuit parameters for different bench and counterpoise grounding schemes. 'Counterpoise floating' configuration with bench bonded to floor as in [33].

configuration	schematic	k_{TEM}	R_{term}	R_{counter}
bench bonded to wall	Fig. 4.6(b)	$-5 \cdot k_{\text{cap}}$	$12\,\Omega$	$1\,\text{G}\Omega$
bench bonded to floor	Fig. 4.6(c)	$+5 \cdot k_{\text{cap}}$	$4\,\Omega$	$1\,\text{G}\Omega$
counterpoise grounded	Fig. 4.6(b,c)	$\pm 5 \cdot k_{\text{cap}}$	no impact	$4\,\Omega$
isolated counterpoise grounded	Fig. 4.6(d)	$+5 \cdot k_{\text{cap}}$	$4\,\Omega$	$4\,\Omega$
isolated counterpoise floating	Fig. 4.6(d)	$-5 \cdot k_{\text{cap}} \cdot 10$	$4\,\Omega$	$1\,\text{G}\Omega$

For the same simulation setup the composition of the ALSE spectrum is illustrated by Fig. 4.10. Note that the specific appearance of this plot is a function of the test setup, i.e. factors k_{cap}, k_{TEM}, circuit parameters and harness type. The transmission factor (TF) is normalized to the cable CM voltage at low frequencies. The top two traces are the CM voltage spectra at both cable ends. 'V_{CM} DUT' means the CM voltage at Port 1, 2 of Fig. 4.3, 'V_{CM} load' that at Port 3, 4. The frequency and amplitude of the CM voltage resonance above $30\,\text{MHz}$ is determined by the used cable harness. The voltage that couples directly to the receiver antenna is the sum of the CM voltages divided by k_{cap}. Additionally, the cable is capacitively coupled via C_{wire} to the elevated bench where it indirectly stimulates the TEM mode. From roughly $3\,\text{MHz}$ onwards the TEM induced voltage gains visible impact on the output voltage of the rod antenna $V_{\text{ALSE,out}}$. Above $10\,\text{MHz}$ TEM coupling dominates the emission spectrum. The oscillations at the elevated bench couple back to the cable and cause a shift in the CM voltage spectra around $20\,\text{MHz}$.

The following subsections validate the applicability of the proposed model to different measurement setups. Generally speaking, the described approach depicts RE trends within typical ranges of measurement uncertainty and repeatability (compare to the collection of results in [26]) and matches the accuracy achievable by simplified 3D simulations.

4.3.1. Evaluation of Bench Grounding Schemes and Table Size

As described above, the correlation between direct capacitive coupling and indirect TEM induced coupling via the floating end of the elevated bench (4.2) was found by parametric simulation and comparison to measurement results. For above configuration, i.e. with the bench horizontally bonded to the rear wall, $k_{\text{TEM}} = -5 \cdot k_{\text{cap}}$ was used, meaning that TEM 'radiation' and capacitive coupling are in anti-phase. It is easy to comprehend that if the bench is vertically bonded to the floor this will influence the TEM mode, because the field propagation between the bench, i.e. the center conductor of the stripline, and the chamber's

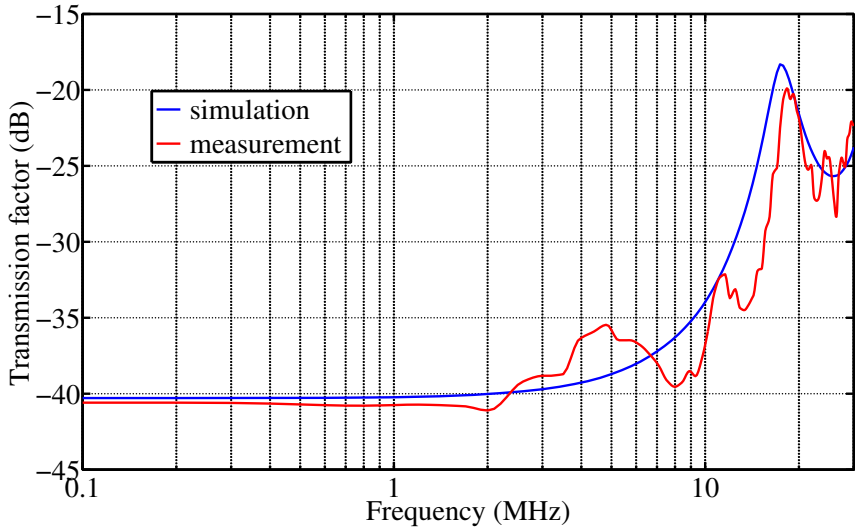

Figure 4.9.: Simulation (resulting from Fig. 4.10) versus measurement (green trace from Fig. 2.3) of the transmission factor from the CM voltage on the DUT cable end to output voltage at rod receiver antenna. Single $1.5\,\mathrm{m}$ TWP with floating load. Table is bonded to wall, $W_{\mathrm{table}} = 3\,\mathrm{m}$, $D_{\mathrm{table}} = 1\,\mathrm{m}$.

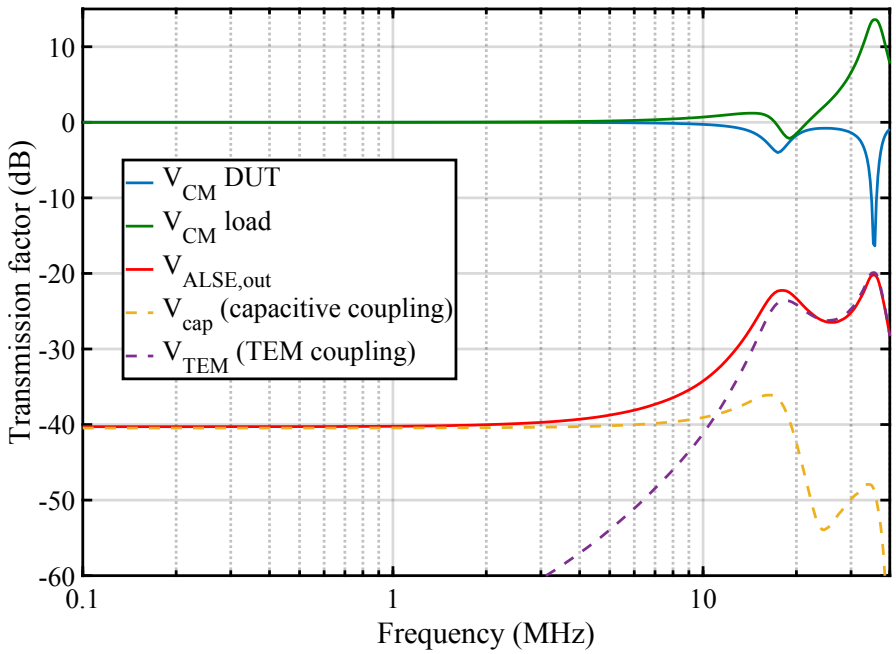

Figure 4.10.: Composition of the ALSE spectrum obtained by simulation. The plot shows the contribution of both coupling modes on the ALSE reading. The terminology of voltages is equal to Fig. 4.3.

ground gets disturbed. Interestingly, now the opposite applies, i.e. $k_{\text{TEM}} = +5 \cdot k_{\text{cap}}$, meaning the phase of the TEM induced voltage V_{TEM} is shifted by 180 degree and now adds to V_{cap}. This finding is validated by comparison to measurement results shown in [18].
In mentioned publication the long wire method of CISPR 25 Annex. J [1] was applied to evaluate the impact of ALSE setup parameters on RE from $10\,\text{MHz}$ to $30\,\text{MHz}$. The authors Uno *et al.* investigated different bench grounding schemes (horizontally bonded to wall, vertically bonded to floor, additional grounding of the counterpoise to floor) by measurement and the influence of the table's width and depth by 3D EM simulation. The results obtained with the above described circuit model are compared to the results published in the paper in Figures 4.11 to 4.13. (The plots use a linear scale frequency axis to allow easier comparison with the original work.) By simulation the resonances are more pronounced, however relative changes in amplitude and resonance frequencies can be well observed with the presented circuit model and the influence of the setup parameters is correctly depicted.
It is confirmed by Fig. 4.12 and Fig. 4.13 that the table depth has more impact than its width. This is already obvious from the circuit schematics and (4.5): The number of LC elements used to model the table scales linearly with D_{table} and so does $Z_{0,\text{table}}$, but a change of W_{table} has no linear impact on $Z_{0,\text{table}}$ (see (4.5)).
For the simulation a top-level schematic like Fig. 4.5(b) and the circuit parameters according the first three rows of Table 4.3 (all three for Fig. 4.11 and the second for the other figures) and the last row of Table 4.2 were used. It is noteworthy that k_{cap} for the long wire method was not found by calculation, because (3.14), which does not respect the finiteness of the ground plane size, would yield $-53\,\text{dB}$, (3.18) on the other hand, which respects the limited width of the table extension by mirroring only part of the wire charge, would yield $-45\,\text{dB}$. The value resulting from CISPR 25 Annex. J is in between, namely $-49\,\text{dB}$. It may be that (3.18) is overestimating the impact of the finite ground plane because the $0.5\,\text{m}$ wire used for the 'long wire method' is - in contrast to the default $1.5\,\text{m}$ cable - hardly shorter than the width of the table extension of $0.6\,\text{m}$. Additionally, the ground pillars holding the wire might have significant impact on the wire's capacitance to ground because of the short wire length, so that (3.1) is not applicable to derive C_{wire}. However, the objective of this section was not to evaluate the precision of the derivation of k_{cap} given in Chapter 3 in case of unusually short cable harnesses, but rather to verify the overall ALSE RE simulation model. Therefore, the value $k_{\text{cap}} = -49\,\text{dB}$[2] was copied from the standard's specification.

4.3.2. Antenna Counterpoise Connection Schemes

Gandolfo *et al.* investigated in [33] the impact of different ways of grounding the rod antenna's counterpoise by experiment and simulation. The referenced work was motivated

[2] Annex. J of CISPR 25 Ed.4 [1] defines a signal amplitude of $110\,\text{dB}\mu\text{V}$ at the wire radiator ($120\,\text{dB}\mu\text{V}$ source with $10\,\text{dB}$ attenuator) and gives reference E-field results of about $61\,\text{dB}\mu\text{V/m}$ at low frequencies which yields a transmission factor of $-49\,\text{dB}$.

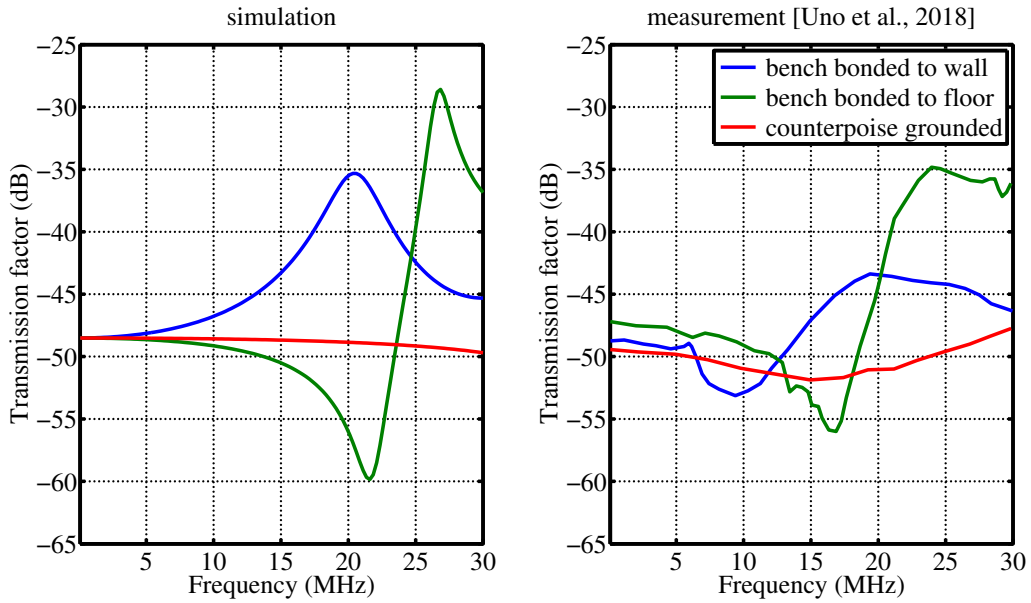

Figure 4.11.: Simulation VS measurement results published in [18] for long wire method of CISPR 25 Annex. J and various grounding schemes.

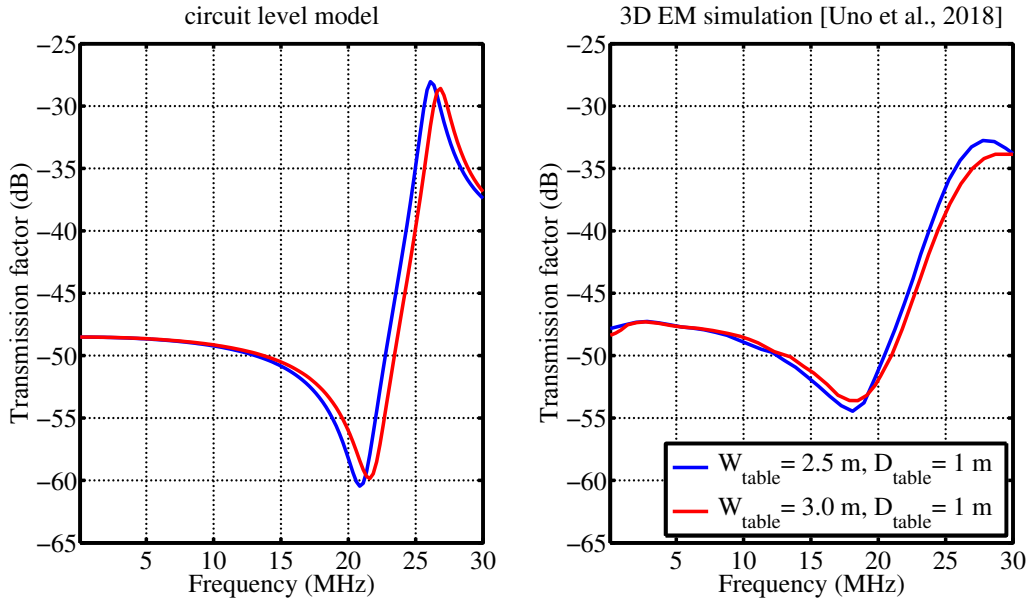

Figure 4.12.: Simulation VS 3D EM simulation results published in [18] for long wire method of CISPR 25 Annex. J showing the impact of changing the table's width W_{table} at constant table depth of $1\,\text{m}$.

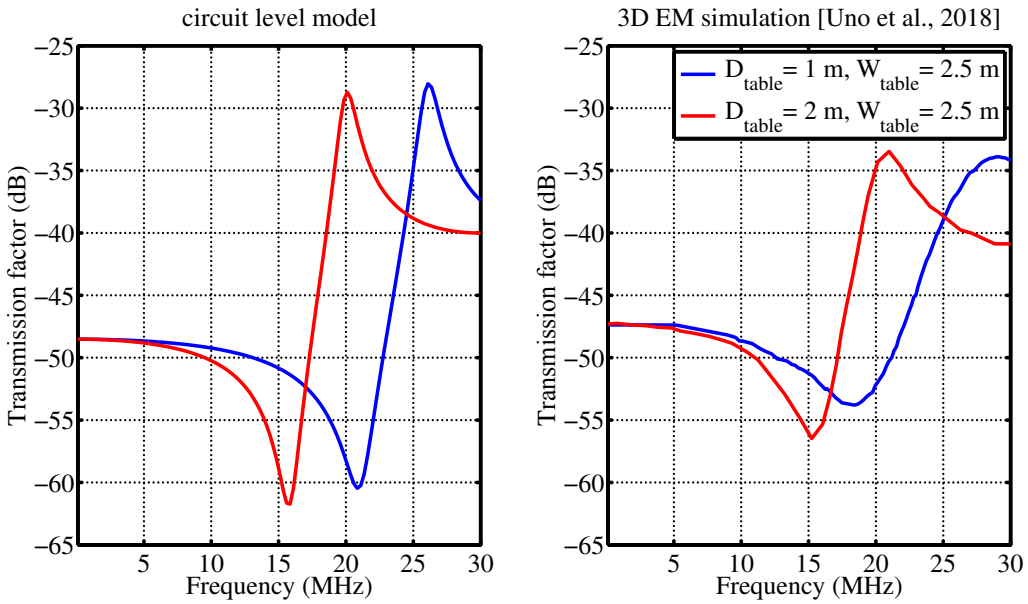

Figure 4.13.: Simulation VS 3D EM simulation results published in [18] for long wire method of CISPR 25 Annex. J showing the impact of changing the table's depth D_{table} at constant table width of $2.5\,\text{m}$.

by the fact that MIL-STD-461F (as well as 461G) specifies that the counterpoise must not be connected to the table, as defined by CISPR 25, but vertically grounded to the chamber floor. Additionally, during the discussion of the 'best' counterpoise connection scheme some authors found that a totally isolated counterpoise at floating potential would least disturb the actual E-field at the receiver antenna's position. Although scope of this thesis is the CISPR 25 configuration, an universal circuit level model of the ALSE setup should be valid irrespective of the counterpoise connection, hence the simulation results with the proposed model were verified against the measurement results published by Gandolfo.

The referenced work used a $1.5\,\text{m}$ wire terminated to the table surface, hence Fig. 4.5(b) and the respective rows of Table 4.2 apply. The schematic can be easily adjusted to reflect the isolated counterpoise as demonstrated in Fig. 4.6(d). Direct counterpoise connection to the chamber floor is reflected by choosing a small value for R_{counter}.

Carobbi states in [22] that the RE reading can decrease by $10\,\text{dB}$ to $20\,\text{dB}$ when the counterpoise is floating. The specific value is a function of the counterpoise impedance towards ground and also the rod antenna circuitry, the precise modeling of which is not covered by the simulation model described in this work. To verify nonetheless whether the circuit level simulation does depict the RE outline above $10\,\text{MHz}$ correctly, for the comparison to [33] the value of k_{cap} was adjusted by $-20\,\text{dB}$, i.e. divided by 10, to reflect the measurement results from the paper. Interestingly, TEM mode coupling is unaffected by the floating counterpoise (at least in magnitude, the sign changes), thus for the expression of k_{TEM} in terms of k_{cap} it is multiplied by 10 again (compare first and third row of Table 4.2 and the last two rows of Table 4.3).

In Fig. 4.14 the influence of different counterpoise connection schemes is visualized by

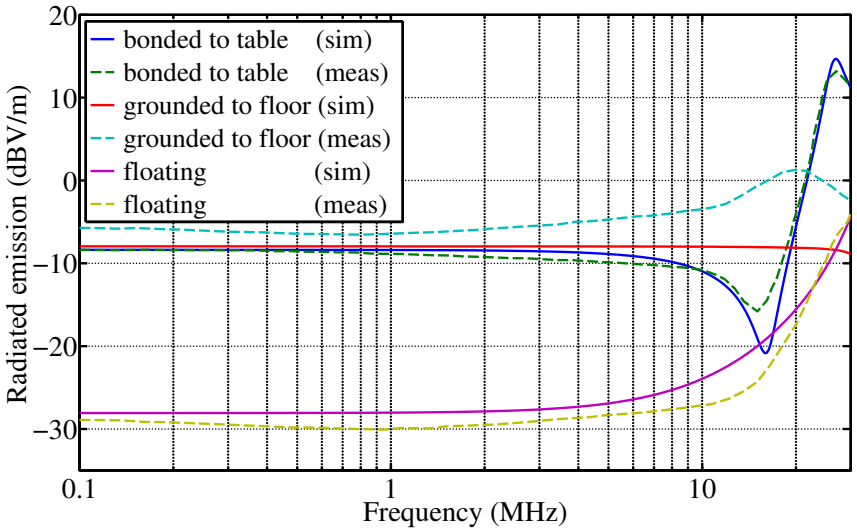

Figure 4.14.: Model verification for different counterpoise connection schemes. The measurement results are copied from [33]. The related work used a $1.5\,\mathrm{m}$ single wire terminated at one end to the bench plane. The elevated bench was bonded vertically to the chamber floor. Because the source amplitude is not revealed in the paper it was not possible to obtain the transfer function from the published measurement results. Therefore an offset factor was derived by comparing the simulated transfer factor at $100\,\mathrm{kHz}$ to the measured RE for the table-connected configuration and applied to all simulation results.

simulation with the proposed circuit model and compared to the measurement results published in [33]. Despite the differences, the general usability of the proposed circuit model is confirmed by the measurements. The biggest deviation is observed when the counterpoise is 'grounded to floor', i.e. unconnected from the table and vertically connected to the chamber's ground plane only via the shield of the coaxial cable which transmits the output signal to the EMI receiver. This is the default MIL-STD-461G illustrated by Fig. 4.1. According this standard, a ferrite with 20-$30\,\Omega$ at $20\,\mathrm{MHz}$ should be attached to the mid-point of the coaxial cable. This was done during the measurements but is not reflected by the simple circuit model. Kay considered in [67] the frequency dependency of the ferrite. He suggested to model it by $6\,\Omega$ in series to $0.2\,\mu\mathrm{H}$ (instead of $R_{\mathrm{counter}} = 4\,\Omega$ as used here) and noted that this would increase RE by roughly $6\,\mathrm{dB}$ above $25\,\mathrm{MHz}$.

4.4. Chapter Conclusion and Summary of Scientific Content

In this chapter a circuit level model to simulate ALSE test RE in the complete CISPR Band B from $150\,\mathrm{kHz}$ to $30\,\mathrm{MHz}$ was presented. The radiation captured with the rod antenna is originating from two sources:

- First, direct capacitive coupling, which was discussed in detail in Chapter 3. This coupling mode is modeled by a simple capacitive divider.
- Second, indirect or TEM mode coupling due to the elevated ground plane. The elevated ground plane is understood as transmission line and respected with an equivalent circuit reflecting its characteristic impedance. As a result, the rod antenna's reference potential is no static ground but influenced by the capacitive coupling of the cable harness towards the elevated bench and the bonding to ground of the latter. A portion of the received emissions is proportional to the signal on the bench by a factor k_{TEM} which describes the magnitude and phase of TEM induced radiation.

Cavity resonances are not included in the simulation model because they typically appear at frequencies above $30\,\mathrm{MHz}$. The model does only respect the dimension of the elevated ground plane and the low frequency (LF) absorber performance at the rear wall, not the dimension of the shielded enclosure itself.
The presented simulation model has physical meaning and does not include network-parameter black boxes which makes it easy to comprehend. It is furthermore usable in any circuit design environment and does not notably increase simulation times because it is based on RLC components only. The model is tunable to the dimension and ground connection of the elevated bench which enables to adjust the simulation to the test setup, for instance if simulations should be compared to measurements conducted in a specific chamber. Remember that Annex J of CISPR 25 Ed.4 [1] states that 'the absorber materials and reference ground plane grounding utilized in the ALSE will generally create the largest measurement deviations at frequencies below 200 MHz.' The design parameters used to tune the circuitry to reflect certain ALSE configurations were discussed and their impact exemplified by comparison to measurement and 3D EM simulation results of related works of other authors.
A model of the actually used cable harness can be integrated by modifying the respective circuit block. Such cable model needs to be accurate only within the limited considered frequency, hence it can be obtained easily with common transmission line simulation tools. The capacitive coupling factor k_{cap} (and consequently k_{TEM}) can be determined as exemplified in Chapter 3.7.

Basically, all the ideas leading to the presented circuit model where published by other authors before. Thus, the novelty of this work is not to show that ALSE RE can be simulated by a circuit level model. Novel to this work is rather the universality and the usefulness for day-to-day (IC) design tasks. For the first time a complete model is exhibited which covers the complete test environment from the DUT output to the EMI receiver input, i.e. cable

harness, bench and receiver antenna. Many existing publications on ALSE modeling are of pure academic nature. They investigate only parts of the problem, e.g. the impact of the counterpoise grounding scheme [22], or replace the DUT and the harness with ideal sources [71], or are too complicated to use without deep understanding of the radiation mechanisms [72]. Most use RLC component values obtained from 3D EM simulation or measurement which are specific for a certain setup and cannot be adjusted by the model's user (e.g. the IC designer) without detailed knowledge of the model generation procedure. In contrast, all component values used in this work are obtained from textbook equations (or were derived in the preceding chapters) and the circuitry itself reflects the physical setup.
In summary, the scientific novelty of this chapter is the merge of all modeling approaches that were published so far to a circuit model which is applicable to a broad range of test setup variances. This comes of course at cost of accuracy, however the described approach depicts RE trends within typical ranges of measurement uncertainty and repeatability and matches the accuracy achievable by simplified 3D simulations.

With this chapter the simulation of ALSE test radiated emission is concluded. A model to obtain the voltage signal at the EMI receiver input was established. So far, radiated emission was discussed in terms of relative transmission factors between DUT output signal and EMI receiver input signal. Coming back to Fig. 1.1 of Chapter 1 this corresponds to the middle block of the overall simulation topology. Yet, to obtain the final emission reading - which is relevant to evaluated pass or fail of given emission limits - the post-processing of the transient signal conducted by the EMI receiver needs to be considered. Therefor the next chapter covers means to emulate an EMI receiver by software, i.e. the final rightmost block of Fig. 1.1.

5. EMI Receiver Modeling

In most published works on the simulation of electromagnetic emissions the impact of the measurement instrument itself, the EMI receiver, is omitted and the emission spectrum is obtained by a straight-forward Fourier transformation. As long as only relative changes in the emissions of different designs are evaluated this might be sufficient. But when the simulated emission spectra should be compared to real measurement results, the circuit designer has to be aware of the differences in the post-processing of time domain data between an ordinary Fourier transformation and the short time Fourier transformation (STFT) applied by a modern EMI receiver when conducting a so-called 'time domain' scan. As exemplified by Fig. 2.9, in case of broadband distortions the PK detector reading can be significantly above the DFT outline, because the EMI receiver might capture more noise with its broader window. Generally speaking, without good knowledge of the actual signal input to the EMI receiver, it is impossible to tell how exactly the DFT result relates to the EMC test result. A designer running EMC simulations should be aware of that fact.

The focus of this thesis is on the application of data transmitting devices. An example of a possible output voltage waveform is given by Fig. 5.1 for a differential driver. The device is in sleep mode when no data is transmitted and both outputs are terminated to $0\,\mathrm{V}$. Before each transmission of a data package both outputs are ramped up to a mid-level from where the data modulation is executed. The resulting CM output voltage (leading to radiated emission from the cable harness) is the superposition of the mid-level on/off keying and distortions due to the actual driver operation, which are much smaller in amplitude. Obtaining the emission spectrum of such a waveform by simulation is tiresome for two reasons:
First, the period time is very long. A transient simulation (e.g. on IC transistor level) will need much time.
Second, it is obvious that the emissions will be dominated by the activation and deactivation of the driver output, hence the time-consuming simulation of the complete period might yield no insights into the spectral distortions produced by the actual DUT operation. It is also clear that the overall emissions measured during an EMC test will depend on the specific transmission protocol, i.e. the idle time in between packages and the transmitted data stream.
In the following sections both problems will be dealt with. The signal content due to the mid-level on/off keying is a trapezoidal pulse train with low repetition rate. Consequently it acts as broadband disturber, so that a DFT without special post-processing will not correctly predict the EMI receiver's PK reading. The Fourier envelope of that basic signal type is well known, as is that the transition times do significantly affect the frequency spectrum. By limiting the slew rates, the emissions introduced by the mid-level ramping can be achieved to fall below that of the main DUT operation and consequently have no noteworthy impact on the EMC test result. However, the questions remains how the PK reading relates to the Fourier envelope. In Section 5.1 the different frequency resolution of DFT and EMI receiver are considered and a correction factor is developed to obtain the PK reading from the DFT. The second issue, i.e. the specific transmission protocol, does not affect the PK reading but

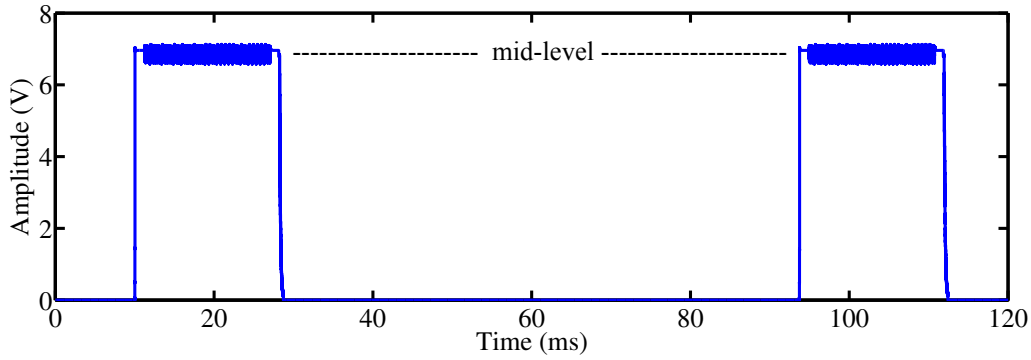

Figure 5.1.: Exemplary CM voltage output of a data transmitting device. Ideally, the differential output driver should produce no CM content but the mid-level ramping. Practically, during each switching event some CM distortions are generated, which results in CM noise of some hundred mV amplitude. The signal period T is $83\,\mathrm{ms}$.

rather the Average (AVG) and Quasi-Peak (QP) detector readings. In Section 5.2 it will be presented how to mathematically respect idle times in the data stream and to interpolate the detector readings without having to simulate the complete data transmission.

5.1. EMI PK Spectrum from a Broadband Trapezoidal Pulse Train

Fig. 2.9 of Chapter 2.5.1 compared the emission spectra of narrowband (NB) and broadband (BB) signals and showed that for BB signals a simple DFT underestimates the EMI receiver's reading. Now, the same distinction is made by Fig. 5.2 but in more detail. The presented example uses signals with long or short period times T, which corresponds to low or high pulse repetition frequency (PRF). The low-frequency level of the Fourier envelope of a trapezoidal pulse train is proportional to $A\tau/T$, compare Fig. 5.4(b). The spacing of the spectrum lines equals the pulse repetition frequency (PRF) which is the inverse of the signal period PRF $= 1/T$. Hence, the number of spectrum lines that appear within the receiver bandwidth are proportional to T. In case of NB disturbers with PRF $>$ RBW, treated by Fig. 5.2(c) and (d), the peak levels of DFT and PK detector are equal and both proportional to $A\tau/T$. If PRF $<<$ RBW, more specifically, if PRF $< \Delta f_{\mathrm{EMI}}$ as in Fig. 5.2(a) and (b), the EMI receiver displays a continuous spectral line and the PK detector reading is significantly above the DFT outline. Roughly speaking, the effect of the window's RBW is, that all spectrum lines are summed up, thus the PK reading becomes proportional to only the pulse area $A\tau$, i.e. independent of the signal period T, whereas the difference between DFT outline (which corresponds to only one spectrum line) and PK detector level is a function of the latter. To obtain the exact PK detector values the applied window function and its coherent attenuation (CA) need to be respected. Thereby a correction factor can be derived, which enables to predict the PK reading from a given DFT result, or from a known Fourier envelope. Its calculation is scope of this chapter. It is accomplished by considering

Table 5.1.: EMI receiver parameters used in this work (CISPR Band B) based on [55, 54]

parameter	symbol	value
resolution bandwidth	RBW	9 kHz
frequency step size	Δf_{EMI}	2.25 kHz
window time domain length	T_{W}	444 μs
standard deviation of the Gauss window	σ	42 μs

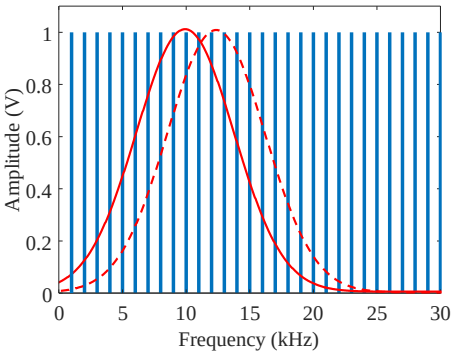

(a) Blue: Impulse train with 1 kHz repetition rate, PRF << RBW. Red and red dashed: intermediate frequency (IF) windows applied by the EMI receiver. The frequency step size Δf_{EMI} in between windows is 2.25 kHz in shown case.

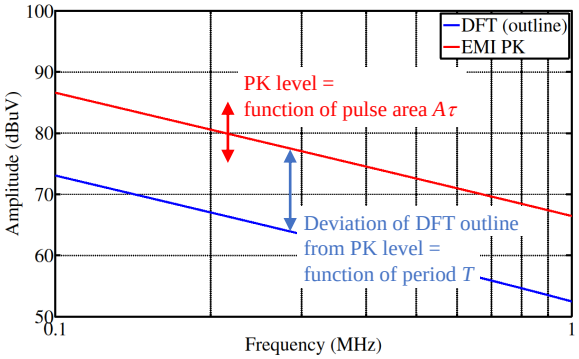

(b) If PRF $< \Delta f_{\text{EMI}}$ (appr.) as illustrated to the left, each IF window captures the same distortion level, so that the EMI receiver displays a continuous spectral line. The PK detector reading (red) is above the DFT outline (blue), whereas the deviation relates to the signal period T.

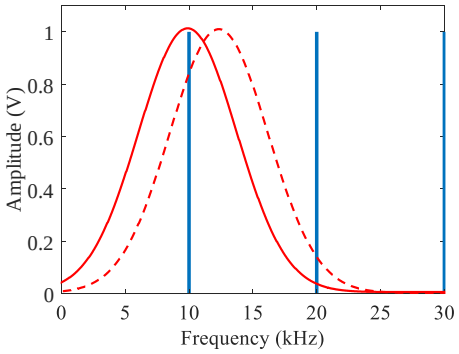

(c) Impulse train with 10 kHz repetition rate, PRF > RBW.

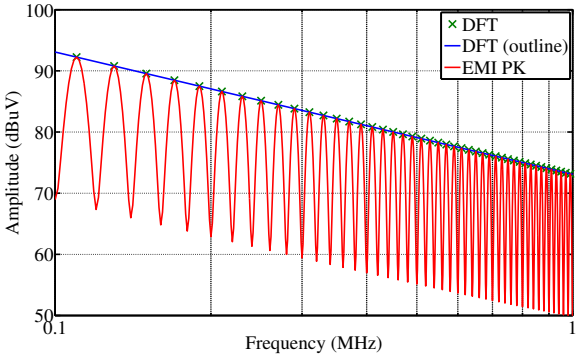

(d) The roll-off of the 9 kHz Gaussian window is different from that of the DFT, hence the spectral appearance differs but the peak values match.

Figure 5.2.: Left subfigures: EMI receiver windowing in frequency domain. All amplitudes are scaled to 1 V. Right subfigures: EMI PK reading in comparison to the DFT spectrum of the same signal. Shown are the spectra of a trapezoidal pulse train with slew times of 100 ns, 50 % duty cycle and PRF of 1 kHz or 10 kHz.

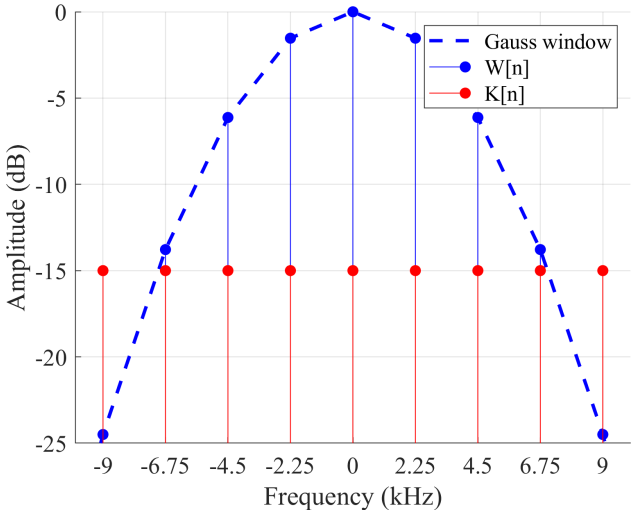

Figure 5.3.: Frequency discrete Gauss window $W[n]$ and constant signal $K[n]$. ©2017 IEEE [73]

the STFT carried out by modern TD EMI receivers.

When performing a STFT the time domain input signal $s(t)$ is first chopped into many short time domain chunks $\Delta s(t)$ of the length of the filter window T_{W}. Then a window function $w(t)$ is applied. Each of the resulting weighted signal chunks $\Delta s(t) \cdot w(t)$ are then Fourier transformed $\mathcal{F}[\Delta s(t) \cdot w(t)]$ which yields a high number of frequency spectra, each valid for a short time section of the signal. In practice, the processing is done with discrete time steps (5.1), where the discrete-time window is m points wide. From (5.1) it is obvious, that the weighting with the window function means the summation of all m points of the time-discrete signal chunk $S[n]$ within the window. If all of these happen to be constant $S[n] = K$ the special condition depicted by Fig. 5.3 appears and (5.1) simplifies to (5.2).

$$s(t) \cdot w(t) \mathrel{\hat{=}} \sum_{n=1}^{m} S[n] \cdot W[m-n+1] \tag{5.1}$$

$$\sum_{n=1}^{m} S[n] \cdot W[m-n+1] \overset{S[n]=const.}{\rightarrow} K \sum_{n} W[n] \tag{5.2}$$

The applied window function needs to meet the requirements of CISPR 16-1-1 [53]. The frequency step size Δf_{EMI} and the selectivity of the IF filter window are important variables in this regard. Manufacturers of EMI receiver may choose them differently. The step size Δf_{EMI} depends on the resolution bandwidth RBW. To avoid level errors usually $\Delta f_{\mathrm{EMI}} << RBW$ is used [74], e.g. $\Delta f_{\mathrm{EMI}} = RBW/4$ [51]. In [75] some common window functions are compared and discussed. For this work, it is assumed that the EMI receiver applies a Gauss window (5.4) [55] with the parameter values of Table 5.1.
Above equation (5.2) is very similar to the general definition of the coherent attenuation

(CA) of a window, which is the sum of all window elements divided by the number of elements N_{W}:

$$\mathrm{CA} = \sum_n W[n]/N_{\mathrm{W}} \tag{5.3}$$

For a frequency discrete Gauss window $W_{\mathrm{Gauss}}[n]$ as displayed in Fig. 5.3

$$W_{\mathrm{Gauss}}[n] = e^{-\frac{1}{2}(\frac{n}{\sigma f_s})^2} \tag{5.4}$$

the coherent attenuation is (5.5) as it is expressed in [55].

$$\mathrm{CA}_{\mathrm{Gauss}} = \frac{N_{\mathrm{W}} - 1}{\sigma f_s \sqrt{2\pi}} \tag{5.5}$$

where f_s is the sampling frequency, N_{W} the number of window elements and σ the window's standard deviation. To obtain a frequency response matching the requirements of CISPR 16-1-1 in Band B, $\sigma = 42\,\mu\mathrm{s}$ was chosen [54].
The number of window elements N_{W} is the ratio of the frequency step size Δf and the sampling frequency f_s of the signal under consideration.

$$N_{\mathrm{W}} = \frac{f_s}{\Delta f}. \tag{5.6}$$

Typically $N_{\mathrm{W}} >> 1$, hence the coherent attenuation can be approximated to be independent of the sampling frequency by replacing $N_{\mathrm{W}} - 1$ with N_{W}:

$$\mathrm{CA}_{\mathrm{Gauss}} \approx \frac{N_{\mathrm{W}}}{\sigma f_s \sqrt{2\pi}} = \frac{f_s/\Delta f}{\sigma f_s \sqrt{2\pi}} = \frac{1}{\sigma \Delta f \sqrt{2\pi}} \tag{5.7}$$

The coherent attenuation depends on the chosen frequency step size. This is a defined constant Δf_{EMI} for the EMI receiver. Together with the fixed window parameter σ it yields a constant value $\mathrm{CA}_{\mathrm{EMI}}$

$$\mathrm{CA}_{\mathrm{EMI}} = \frac{1}{\sigma \Delta f_{\mathrm{EMI}} \sqrt{2\pi}} \tag{5.8}$$

On the contrary, when processing a discrete Fourier transformation usually a rectangular window is applied which introduces no attenuation (5.10) and the frequency step size is a variable Δf_{DFT}. Assuming that one complete period T of the signal under consideration is used as input for the DFT, the distance between two frequency bins is defined by (5.9) with N_{DFT} being the number of frequency points and f_s again the sampling frequency.

$$\Delta f_{\mathrm{DFT}} = 1/T = f_s/N_{\mathrm{DFT}} \tag{5.9}$$

$$\mathrm{CA}_{\mathrm{DFT}} = 1 \tag{5.10}$$

Inserting (5.6) and (5.8) or (5.9) and (5.10) into (5.3) allows to compare the respective values for the weighted sum (5.2) which deviate due to the different window parameters:

$$K \sum_n W_{\mathrm{EMI}}[n] = K \cdot \mathrm{CA}_{\mathrm{EMI}} \cdot N_{\mathrm{W}} = K \cdot f_s \cdot \frac{\mathrm{CA}_{\mathrm{EMI}}}{\Delta f_{\mathrm{EMI}}} \tag{5.11a}$$

$$K \sum_n W_{\mathrm{DFT}}[n] = K \cdot \mathrm{CA}_{\mathrm{DFT}} \cdot N_{\mathrm{DFT}} = K \cdot 1 \cdot T \cdot f_s \tag{5.11b}$$

It is finally possible to gain the EMI receiver´s PK detector reading directly from a conventional DFT result by correcting the latter with the ratio of (5.11b) to (5.11a).

$$DFTcorrection = T \cdot \frac{\Delta f_{\text{EMI}}}{\text{CA}_{\text{EMI}}} = T \cdot \frac{\Delta f_{\text{EMI}}}{\sigma \Delta f_{\text{EMI}} \sqrt{2\pi}} = T \cdot \frac{1}{\sigma\sqrt{2\pi}} \tag{5.12}$$

Inserting the value $\sigma = 42\,\mu\text{s}$ from Table 5.1 and expressing the correction factor in dB yields

$$DFTcorrection = 20\,log_{10}(T)\,\text{dB} + 80\,\text{dB}\,. \tag{5.13}$$

The derivation of this correction factor was possible because in (5.2) it was assumed that all time-discrete signal points $S[n]$ are constant within the window‘s bandwidth. This is of course not always the case, however the next subsection gives a relevant application.

5.1.1. Correcting the Fourier Envelope of the Trapezoidal Pulse Train

Consider the well known Fourier envelope of a periodic pulse train, exhibited by the blue curve in Fig. 5.4(b). A drop by $-20\,\text{dB/dec}$ means that above $150\,\text{kHz}$ (the minimum frequency of CISPR Band B) the amplitude difference between signal points S$[n]$ within $9\,\text{kHz}$ is less than $1\,\text{dB}$ and gets even smaller for higher frequencies. Hence, the requirement for above derivation is conformed and (5.13) can be used in combination with the Fourier envelope of the pulse train to correct the DFT outline DFT_{pulse} (blue trace in Fig. 5.4(b)) to obtain the corresponding PK detector reading PK_{pulse} (red trace in Fig. 5.4(b)). The result (5.14) meets the expectation indicated by Fig. 5.2(a) as it is only a function of the pulse area but independent of the signal period.

$$\begin{aligned} PK_{\text{pulse}} &= 20\,log_{10}(2A\tau/T)\,\text{dB} + 20\,log_{10}(T)\,\text{dB} + 80\,\text{dB} \\ &= 20\,log_{10}(2A\tau)\,\text{dB} + 80\,\text{dB} \end{aligned} \tag{5.14}$$

The application of (5.14) is illustrated by Fig. 5.4(b). So far it was assumed that the maximum spectral energy captured by the EMI receiver (within a single window) equals that captured by the DFT (within one signal period). This is only true if the trapeze is short enough to completely fit inside one filter window (impulse) or if only one edge of the pulse significantly contributes to the emission spectrum.
If the pulse is perfectly symmetric and wider than a filter window, the spectral energy is equally distributed between the rising and falling edge of the pulse. The EMI receiver's PK reading will be exactly half of the DFT result, thus the correction factor needs to be decreased from $80\,\text{dB}$ to $74\,\text{dB}$. Although truly symmetric transients are unlikely for real signals, they are very common in simulations. In reality the needed adjustment will be somewhere below $6\,\text{dB}$.
If no edge fits completely into one window, the DFT result cannot be directly used to derive the Peak detector reading, because the prerequisite used to derive (5.13) - that the spectral outline is as good as constant within the bandwidth of one filter window - is not fulfilled.

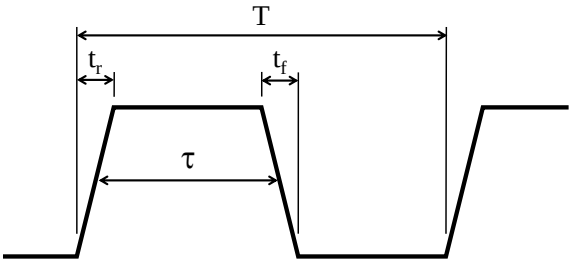

(a) Time domain waveform of a trapezoidal pulse train with amplitude A, period T, pulse width τ, transition times t_r and t_f.

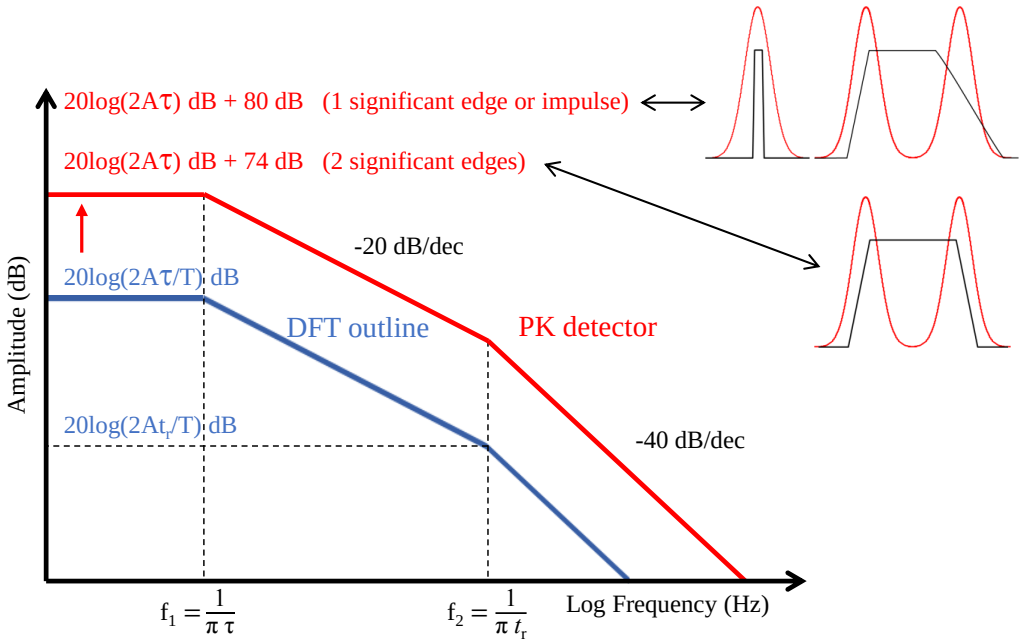

(b) Fourier envelope for a trapezoidal pulse train with $t_r = t_f$ (blue) and the corresponding PK detector reading (red) for signals were all spectral energy is captured by one STFT window (1 significant edge or impulse) and those were the energy is equally distributed (2 significant edges).

Figure 5.4.: Correction of the Fourier envelope of a periodic pulse train to obtain the corresponding EMI receiver's PK detector. ©2017 IEEE [73]

5.1.2. Validation

5.1.2.1. Periodic Impulse and Impulse Package

To showcase the application of the above introduced DFT correction factor, a simple example is given by Fig. 5.5. The top part of the figure shows a periodic impulse with repetition frequency much lower than the RBW of the EMI receiver. This is a broadband disturber where the foregoing considerations apply. The bottom part of the figure shows the same impulse in a burst package of three, with a separation of each $200\,\mu\mathrm{s}$, which corresponds to a repetition frequency of $5\,\mathrm{kHz}$ which is still below the RBW of the EMI receiver. A DFT by definition captures the spectral energy of one complete signal period. Obviously, the two signal variations of Fig. 5.5 yield different DFT results. In contrary, the EMI receiver's PK detector output is always the same. The effect can be easily explained by the working principle of the STFT utilized by modern EMI receivers during a time domain scan: For the STFT a filtering window (red in Fig. 5.5) is moved along the signal in time domain, capturing only the spectral energy of the signal chunk 'visible' inside the window. The DFT on the other hand captures always all energy contained within a signal period (brown dashed in Fig. 5.5). In case of the impulse package, the DFT of one signal period captures 3 impulses, whereas the PK detector 'sees' never more than one impulse at a time. The DFT overestimates the PK reading by a factor of 3, i.e. $9.5\,\mathrm{dB}$ (irrespective of the coherent gain of the Gauss window).
Respective measurements were conducted with an impulse as illustrated by Fig. 5.6 and period $T = 700\,\mu\mathrm{s}$. For the case of the single impulse, the PK reading can be directly calculated by (5.14), yielding $69.04\,\mathrm{dB}\mu\mathrm{V}$ for the spectral outline at low frequencies. The $-3\,\mathrm{dB}$ transition point to the $-20\,\mathrm{dB/dec}$ region is at $3.18\,\mathrm{MHz}$. Both values are in excellent agreement to the actual PK detector result displayed by Fig. 5.7. A DFT considering one complete period of the signal yields the purple trace of Fig. 5.7. According (5.13) this needs to be corrected by $16.90\,\mathrm{dB}$. This is very close to the exact deviation to the actual EMI PK detector reading, namely $16.44\,\mathrm{dB}$.
Considering a pulse triplet as depicted by the bottom figure of Fig. 5.5 with again a period of $T = 700\,\mu\mathrm{s}$, the EMI receiver displays the same PK levels. The DFT outline however increases by roughly $9.5\,\mathrm{dB}$ because thrice as much spectral energy is contained within one period. (Additionally, the modulation due to the bursting is visible by the orange trace in Fig. 5.7.) The DFT correction factor provided by (5.13) needs to be reduced respectively to $7.4\,\mathrm{dB}$ and applied to the outline of the DFT result (green dashed trace). This then leads again the correct PK detector levels.

5.1.2.2. Practical Example of Fig. 5.1

The presented DFT correction factor allows to omit the low-frequency trapezoidal content of the CM signal illustrated in Fig. 5.1 when the DUT output waveform is simulated. The

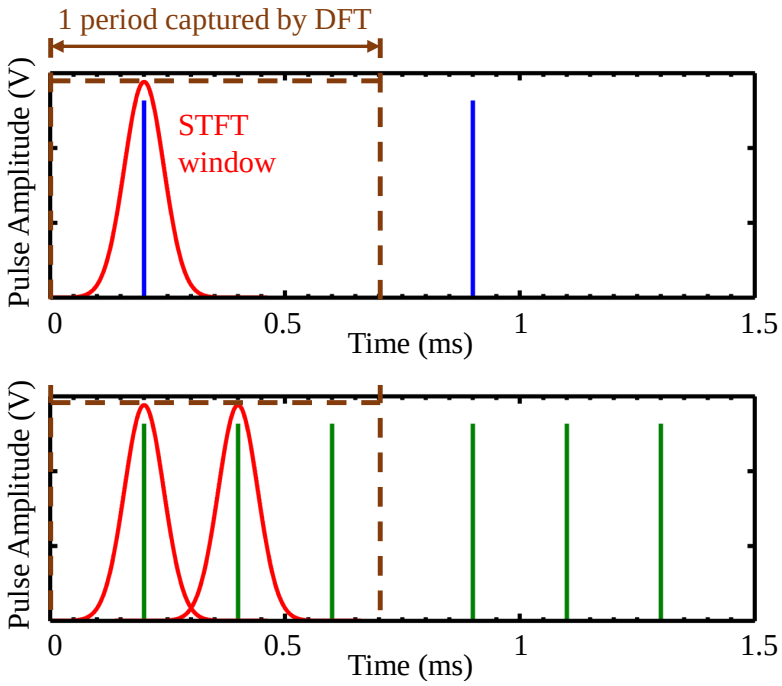

Figure 5.5.: Top (blue signal): A single impulse repeating every 700 μs. In time domain, the STFT window applied by the TD EMI receiver is 444 μs wide [54]. As long as the same signal content falls into the windows applied by TD EMI receiver or DFT (here: Gauss, red, vs. rectangular window, brown), the PK detector reading deviates from the DFT outline only by the coherent gains of the respective windows.
Bottom (green signal): A periodic package of 3 pulses with a separation of 200 μs. Because the PRF is still below the RBW of the PK detector ($1/200\,\mu\text{s} = 5\,\text{kHz}$ vs. $9\,\text{kHz}$), its output is unaffected, while that of the DFT changes.

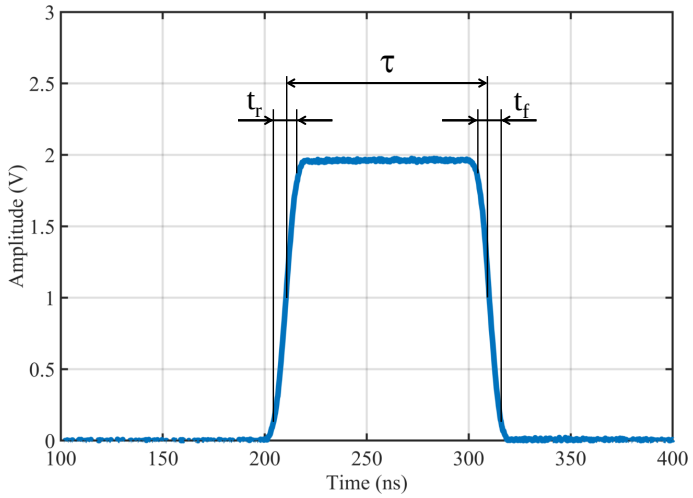

Figure 5.6.: Detailed time domain view of the pulse used for the experiment of Fig. 5.7. Voltage amplitude $A = 2\,\text{V}$, pulse width $\tau = 100\,\text{ns}$, rise and fall times $t_\text{r} = t_\text{f} = 10\,\text{ns}$. Sampling frequency of the oscilloscope was $f_{\text{s, scope}} = 5\,\text{GHz}$.

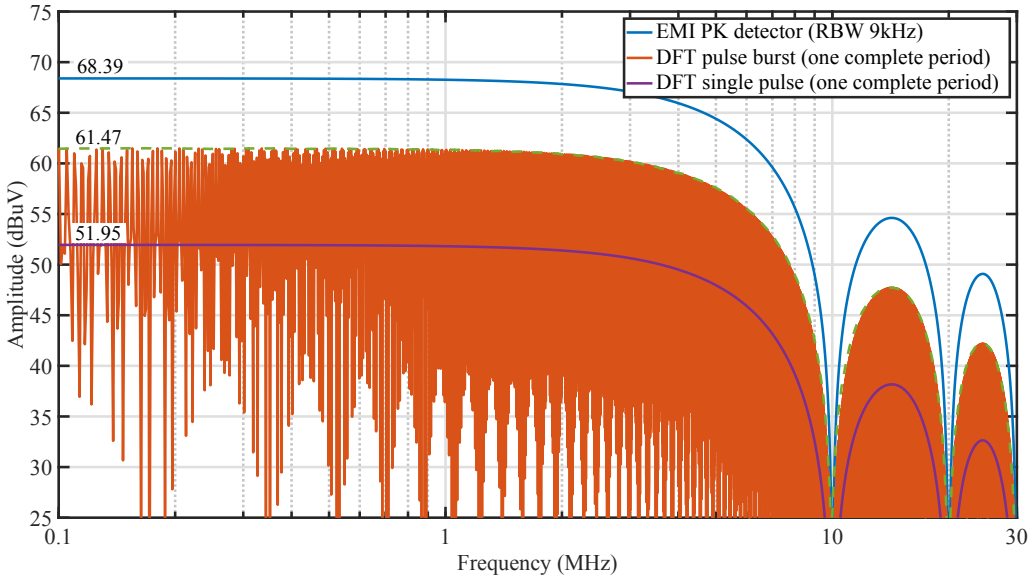

Figure 5.7.: Comparison of DFT results for periodic impulse or impulse package (pattern sketched by Fig. 5.5, using the pulse of Fig. 5.6) and reading of the EMI receiver's PK detector, which is equal for both signal types. For the ease of comparison with (5.14) and (5.13) the DFT outline is traced by the green dashed curve.

spectral impact of that signal content can be evaluated separately, so that the simulation can be limited to the DUT operation during active data transmission.
The adjustment of the Fourier envelope by (5.14) is a rather theoretical approach, because the Fourier envelope itself is a simplification of the DFT outline. Nonetheless, it is useful for instance to investigate basic parameters of a system architecture like the periodicity of data packages (pulse period), ratio of idle and transmission times (duty cycle) and transition times between sleep and active modes.
For a more accurate prediction of the PK detector reading (5.13) is used which takes the DFT result of the actual signal as input. The impact of the real transition shapes can be precisely examined that way, e.g. to check the influence of emission reduction techniques like edge shaping. In Fig. 5.8 the outline of the DFT result of only the trapezoidal on/off content of the CM signal shown in Fig. 5.1 - corrected to respect the RBW of the EMI receiver by applying (5.13) - is compared to an EMI measurement result of the complete signal. As long as the trapezoidal pulse train dominates the emission spectrum by its broadband distortions, the simulation based on the DFT and (5.13) yields the exact PK reading. Only from $3\,\mathrm{MHz}$ onwards the NB distortions introduced by the actual DUT operation, i.e. the data transmission, overtop the BB disturbances.
The NB emission peaks could - in this special case - be predicted by respecting the data package signal content only. An effective way to do this is presented in the next section.

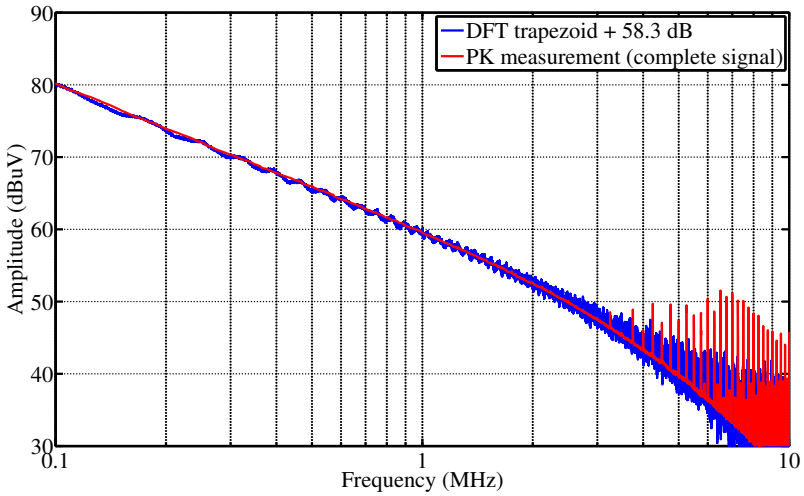

Figure 5.8.: The outline of the DFT result of only the trapezoidal on/off content of the CM signal shown in Fig. 5.1, corrected to respect the RBW of the EMI receiver by applying (5.13), in comparison to the measured PK detector reading of the complete CM signal including the distortions introduced by the data transmission.

5.2. Minimization of Simulation Time for Long Data Transmissions

So far, only the PK detector of the EMI receiver was considered. Often enough this worst-case reading is the only relevant information needed, especially when only the relative change in emissions of different IC designs should be compared.
The readings of the Average (AVG) and Quasi-Peak (QP) detectors are affected by the repetition rate of disturbances, or in other words, by the length of idle times in between disturbances. EMC standards usually define that application typical signals have to be used when performing EMC tests. In the case of a data transmitting device this means a typical transmission protocol which is usually composed of a series of sections of active data transmission and sections of short or long idle times. When the DUT output is simulated, the transient waveform of repetitive signal components, e.g. the output corresponding to digital bits or bit sequences, will always be identical and therefor produce always the same spectral components. Thus, repetitive signal components don't need to be simulated more than once. Idle times will only decrease the emission readings. In this section these properties are exploited to reduce the transient simulation time required to obtain the EMI receiver output. It is assumed that a state-of-the-art EMI receiver software emulator is available, like e.g. [55]. Only the steps to optimize the performance of such emulator are described.
The method presented in the following is applicable for all signals which can be divided into repetitive parts. For the sake of simplicity now only two unique components are considered. However, other signals might be a sequence of more repetitive components, like turn-on and shut-down events. The given equations can easily be extended as needed.
Fig. 5.9 illustrates a chunk of data transmission stream that can be interpreted as set of

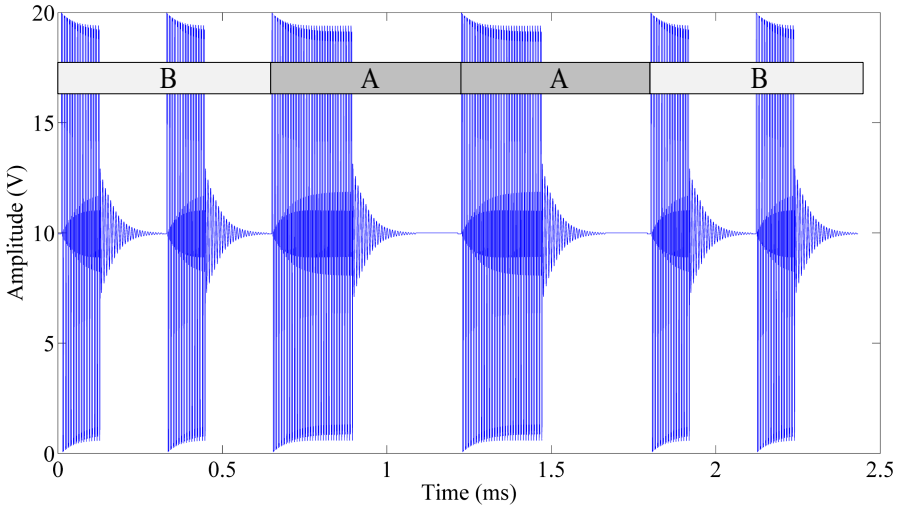

Figure 5.9.: Zoomed view of the data stream under consideration, defining the time domain data corresponding to A and B fraction. Note, that this is a useful but arbitrary definition and does not necessarily correspond to actual digital bits. ©2016 IEEE [76]

two different parts of uniform length t_{fraction}, termed A and B. (This does not necessarily mean that these fractions actually represent digital values.) In order to obtain the detector readings for each fraction separately, two transient signals consisting of either only consecutive A or B fractions are generated. This yields a set of arrays **PK**, **AVG** and **QP** holding one amplitude value for each frequency point of the emission spectrum of the respective fraction and detector type. The emission spectrum of an arbitrary data stream which is a combination of these signal fractions and idle times can be found by combining them in the right manner.

The Peak detector displays the maximum emission which ever appeared during the observation time within the receiver bandwidth, irrespective of the distortion's repetition rate or point in time. Simply taking the maximum spectral components of the two fractions yields the final value.

$$\mathbf{PK} = max(\mathbf{PK}(A), \mathbf{PK}(B)) \tag{5.15}$$

The Average detector builds the arithmetic mean value of all samples during the observation time. Solely the number of occurrences of each fraction is of importance but again not the point in time. The number of fractions $\#A$ and $\#B$ in one period of the data stream yields the detector's output by (5.16) which is weighted by the ratio of transmission time t_{data} and idle time t_{idle}.

$$\mathbf{AVG} = \frac{\mathbf{AVG}(A) \cdot \#A + \mathbf{AVG}(B) \cdot \#B}{\#\text{fractions}} \cdot \frac{t_{\text{data}}}{t_{\text{idle}}} \tag{5.16}$$

The Quasi-Peak detector circuit is respected as analog RC element which is charged or discharged in dependence of the spectral amplitude at the currently processed frequency. The CISPR 16-1-1 standard [53] defines the respective charging and discharging times

τ_{charge} and $\tau_{\text{discharge}}$ in dependence of the considered frequency range. To compute the final detector output value, the appearance of the fractions in chronological order has to be considered. Hereby the QP values induced by a continuous transmission of consecutive A or B fractions, $\mathbf{QP}(A)$ or $\mathbf{QP}(B)$ respectively, is taken as maximum Quasi-Peak reading of the corresponding fractions.
For the calculation of the Quasi-Peak value induced by a data stream, the effect of one fraction after the other is processed with respect of the momentary Quasi-Peak reading. Assume at a (discretized) point in time the QP detector output $\mathbf{QP}_i$ for the currently considered fraction i should be attained. If the maximum possible QP value induced by respective fraction $\mathbf{QP}(A)$ or $\mathbf{QP}(B)$ is higher than the reading $\mathbf{QP}_{i-1}$ before the appearance of that fraction, the QP detector's output will charge for the duration of a fraction t_{fraction} from the old value $\mathbf{QP}_{i-1}$ towards the maximum amplitude by

$$\begin{aligned} \mathbf{QP}_i &= \mathbf{QP}(A) \cdot (1 - e^{-t_{\text{fraction}}/\tau_{\text{charge}}}) + \mathbf{QP}_{i-1} \cdot e^{-t_{\text{fraction}}/\tau_{\text{charge}}} \\ &\text{or} \\ \mathbf{QP}_i &= \mathbf{QP}(B) \cdot (1 - e^{-t_{\text{fraction}}/\tau_{\text{charge}}}) + \mathbf{QP}_{i-1} \cdot e^{-t_{\text{fraction}}/\tau_{\text{charge}}} \end{aligned} \tag{5.17}$$

If the maximum reachable value with the currently considered fraction i is lower than the momentary reading $\mathbf{QP}_{i-1}$, the Quasi-Peak detector output will discharge for the duration of t_{fraction}.

$$\mathbf{QP}_i = \mathbf{QP}_{i-1} \cdot e^{-t_{\text{fraction}}/\tau_{\text{discharge}}} \tag{5.18}$$

As simplifying approximation it is assumed, that the minimum value for discharging is that induced by the current fraction, $\mathbf{QP}(A)$ or $\mathbf{QP}(B)$.
If the same fraction is consecutively transmitted a couple of times, the QP detector will soon settle to the respective maximum value and not change any more until the other fraction appears again. Fig. 5.10 shows the charging and discharging of the detector's output during the transmission of a data block. The effect of the mechanical indicator is simplified as such that neither the maximum nor minimum Quasi-Peak value will be displayed, but the indicated value depends on the idle time t_{idle} between two data blocks, during which the RC element is discharging with the time constant $\tau_{\text{discharge}}$, see (5.19). For this work, the descending behavior of the mechanical indicator is approximated by assuming that the indicated Quasi-Peak reading $\mathbf{QP}_{\text{indicated}}$ is the mean value of the settled maximum and minimum Quasi-Peak values (5.20). The error introduced by this approximation depends on the duration of the idle time but is in the range of a view dB (compare Fig. 5.12).

$$\mathbf{QP}_{\text{min}} = \mathbf{QP}_{\text{max}} \cdot e^{-t_{\text{idle}}/\tau_{\text{discharge}}} \tag{5.19}$$

$$\mathbf{QP}_{\text{indicated}} = \frac{\mathbf{QP}_{\text{max}} + \mathbf{QP}_{\text{min}}}{2} \tag{5.20}$$

5.2.1. Validation

The DUT used for validation of the proposed algorithm was a data transmitter IC operating at a carrier frequency of $125\,\text{kHz}$. The output waveform was similar to the signal shown

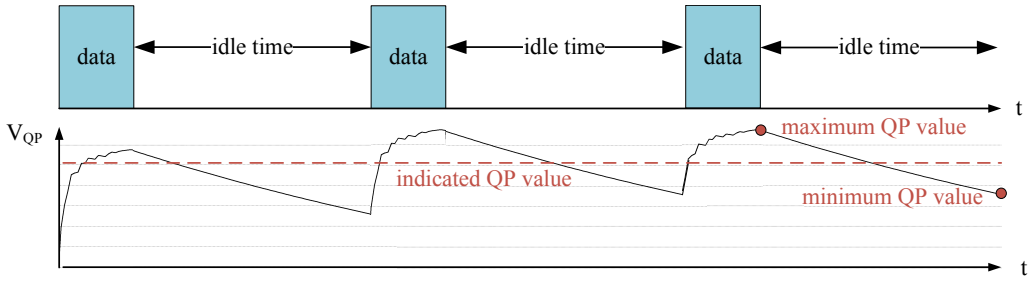

Figure 5.10.: At the end of a complete data block the QP reached its maximum value. During the idle time between two data blocks it is discharging to its minimum value. The indicated reading is simplified to be the mean value of QP_{max} and QP_{min}. ©2016 IEEE [76]

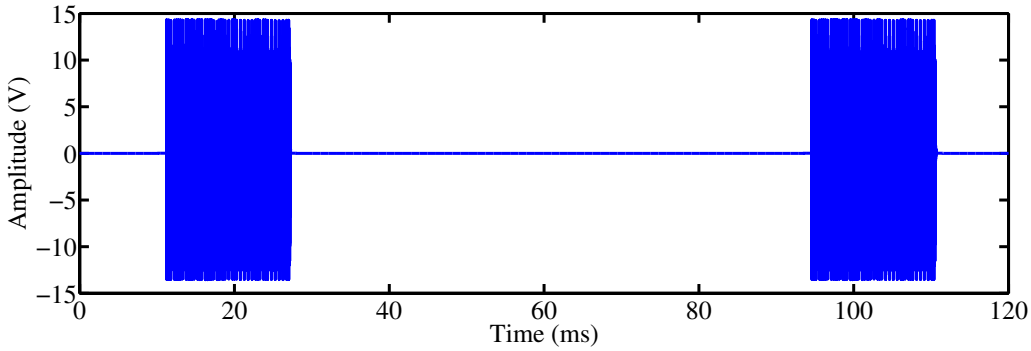

Figure 5.11.: Exemplary signal stream used for validation of the approach to minimize QP simulation time for long data transmissions. The signal was divided in fractions similar to Fig. 5.9. Table 5.2 applies.

Table 5.2.: Parameters of the test signal

number of fractions	24	t_{fraction}	$448\,\mu\text{s}$
number of A	12	t_{data}	$10.752\,\text{ms}$
number of B	12	t_{idle}	$62.9\,\text{ms}$

Table 5.3.: Comparison of simulation time (excluding idle time) and post-processing times of classic EMI receiver model [55] and the model optimized for data transmissions. ©2016 IEEE [76]

EMI receiver model	based on [55]	this work	gain
length of considered signal	$10.752\,\text{ms}$	$896\,\mu\text{s}$	$-92\,\%$
duration of transient IC simulation	$\approx 24\,\text{h}$	$\approx 2\,\text{h}$	
EMI post-processing	$170\,\text{s}$	$3\,\text{s}$	$-98\,\%$

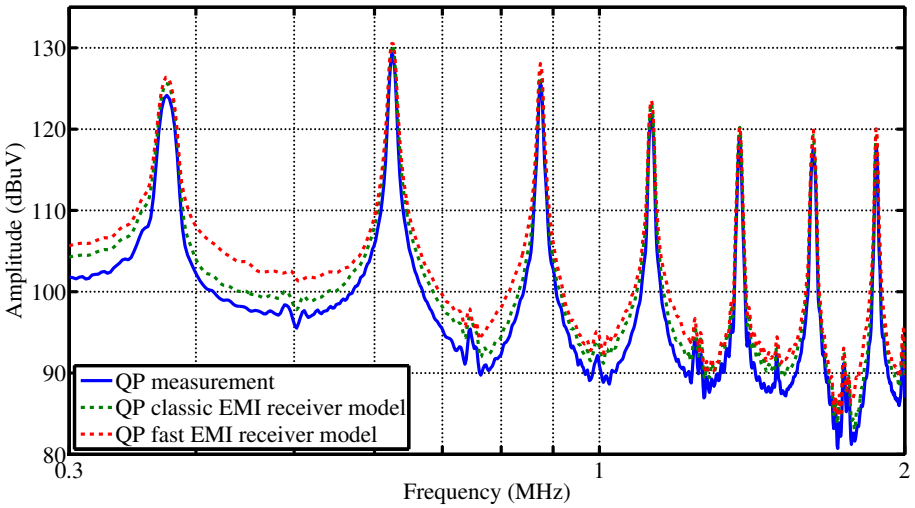

Figure 5.12.: Zoomed views of the QP detector result from 300 kHz to 2 MHz. The results show slight deviations between the proposed fast algorithm and processing the complete signal. 10 periods of the complete data stream were used as input to the 'classic' EMI receiver model which is presented in [55].

in Fig. 5.11. The transmitted test protocol was divided in overall 24 fractions of two kinds, similar to Fig. 5.9, with an idle time of $62.9\,\mathrm{ms}$ between two data blocks. Table 5.2 summarizes the parameters of the test signal.
The emission spectrum of the signal was measured with an EMI receiver directly at the IC's output. Additionally, the time-domain data corresponding to the two data fractions was recorded with an oscilloscope. That sampled data was used as input to the EMI receiver software emulator. Fig. 5.12 compares the measured QP reading to the results obtained with an EMI receiver model based on [55] processing 10 periods of the complete data stream (reproduced by merging the sampled data with idle times in MATLAB) and the proposed model optimized for long data transmissions. The maxima are captured precisely by both models, only the intermediate noise levels deviate slightly from the measurement, because both models use the simplifications for the mechanical indicator discussed above. For the fast model an additional quantization error depending on t_{fraction} is introduced, as this is the minimum time step considered for charging and discharging of the analog RC element which represents the QP detector circuitry.
Table 5.3 compares the signal lengths which are needed for a valid EMI post-processing in dependence of the used EMI receiver model, i.e. the transient data that needs to be simulated, estimated times for transistor level simulation of a complex design, as well as the post-processing times (employing MATLAB). It is assumed that a classic EMI receiver model needs the complete data stream as input, while the presented model optimized for long data transmissions needs only the transient data corresponding to the unique fractions. Idle times do not need to be simulated in any case.

5.3. Chapter Conclusion and Summary of Scientific Content

Often a simple DFT is sufficient to post-process transient simulation data, like the output of the ALSE simulation model presented in Chapter 4, but sometimes it is not. This chapter presented two such issues commonly related to the simulation of emissions produced by data transmitting devices. The original works were published in [73] and [76].
The Fourier envelope of a trapezoidal pulse train is well known. Slew rate limitation or edge shaping will reduce the corresponding electromagnetic emissions [77]. As long as the emission source is narrowband the impact of such methods can directly be shown by Fourier analysis and is in good agreement with the measured EMI spectrum. For broadband sources, however, the receiving instrument's bandwidth and the applied window function has to be considered. The Fourier envelopes found in literature are typically valid for narrowband sources only. Known to the author is merely [78] by Mardiguian to discuss the spectrum from broadband sources. Without derivation he gives a general correction factor for the Fourier envelope to respect a receiver or victim bandwidth, analog to Fig. 5.4(b). However, he does not respect the working principle of an EMI receiver in particular, i.e. the fundamental difference between DFT and STFT. This is the scientifically novel content of Section 5.1, along with the mathematical justification. It enables a circuit designer to estimate the EMI receiver's PK reading based on a DFT result *without* starting an EMI receiver emulator for post-processing. In combination with the pulse weighting characteristics of the EMI receiver according CISPR 16-1-1, illustrated e.g. in [52], also the AVG or QP reading could be found from the PK values, as exemplified in [73]. However, note that if the repetition rate of the pulse is higher than the resolution bandwidth of the used filter window, i.e. $1/T > 9\,\mathrm{kHz}$, only one Fourier harmonic will fall into each window and the DFT peaks itself will equal the PK detector result (narrowband disturber). The presented approach is only useful if $1/T < 9\,\mathrm{kHz}$ (broadband disturber).
During EMC tests the DUT should output an application typical signal. Often this is a combination of repetitive signal components. Then, simulating the whole test signal on circuit level is tiresome. The time-saving approach presented in Section 5.2 is to simulate only the unique signal chunks and merge these to the complete data stream in a post-processing step. It was exhibited how the overall emission reading can be found from the spectra produced by the signal chunks. The proposed algorithm can be understood as application-specific extension to state-of-the-art EMI receiver models, e.g. [55]. Compared to classic general-purpose EMI receiver implementations, it significantly reduces the time needed for transient simulation and for post-processing the time-domain data.

6. Summary

A system supplier has to prove conformity with EMC regulations to be able to sell equipment to vehicle manufacturers. It is common that system suppliers demands the same of their component providers. Hence, it happens that the task of conducting *application and costumer specific* ALSE tests is passed on to IC manufacturers.
In this thesis, the problem of simulating system level RE according the CISPR 25 ALSE test was investigated from an IC designer's perspective, who typically has limited knowledge of the overall system (which might be confidential and/or in development). The task can be divided into three domains:
First, simulation of the device under test (DUT),i.e. the IC's output.
Second, modeling of the propagation path from cable harness attached to the IC output to (rod) receiver antenna.
Third, post-processing of the received signal as well as visualization of the emission spectrum and validation of the results against emission limits.
Given that the environment has negligible impact on the IC's operation, the first part is the daily business of an IC designer, thus it needs no scientific treatment and was not covered in this work. Discussed where the other two parts, with considerations on the integration of the presented findings to native IC design environments. A special attention was paid to applications of data transmitting devices operating at low frequencies of $100\,\mathrm{kHz}$ to $150\,\mathrm{kHz}$.
To ease the following discussion of the scientific findings provided in this thesis and for the reader's convenience, the research questions formulated in Chapter 1 are repeated:

1. For frequencies below $30\,\mathrm{MHz}$, is it possible to simulate the system level emission captured with the vertical rod antenna from component level view, without detailed knowledge of the overall system, specifically without proper definition of cable harness and ALSE?
2. How accurate could such a simulation be? What are the limiting factors?
3. What are the main radiation mechanisms and how does RE relate to output quantities observable by the IC designer?
4. Speaking of data transmitting devices and extremely long transient test data streams, it is in many cases neither feasible nor necessary to simulate the complete transient IC output for EMC analysis. How can circuit simulation times be decreased? How are the outputs of the EMI receiver‘s Peak, Quasi-Peak and Average detectors affected by modifying the transmitted data stream?

As introduction to this work the poor repeatability of the ALSE test due to the vast impact of the chamber and test setup were discussed. The specification by the CISPR 25 standard leaves many degrees of freedom, hence there is no single 'correct' ALSE test result. It is therefor not possible to provide a unique and generally applicable simulation model. Nonetheless, for very low frequencies direct capacitive coupling between the cable harness and the receiver antenna dominates the measured 'radiated' emission. An analytical derivation of the capacitive coupling factor was given in Chapter 3, together with a discussion of

the low-frequency radiation of a harness consisting of multiple cables. The new scientific findings were originally published by the author in [39, 58]. Based the presented analytical calculations, a series of measurements and 3D simulation following rule of thumb could be derived (which gives answer to research questions 1 and 2):

> RE below $3\,\mathrm{MHz}$ is approximately $40\,\mathrm{dB}$ lower than the *common-mode voltage* at the harness.

This is true as long as the harness consists of a small number of unshielded cables, whereas exact conductor diameters, harness length and cable twisting do not falsify the approximation (as long as all three are within automotive-typical ranges). Three things need to be clarified at this point:
First, although this rule is valid only for a very limited frequency range, it is significant and extremely helpful for rapid forecasts of ALSE test results, especially for devices operating in the range of $100\,\mathrm{kHz}$, because it covers the AM radio band ($530\,\mathrm{kHz}$ to $1.8\,\mathrm{MHz}$) where EMC issues are likely to appear.
Second, the fact that the RE reading at very low frequencies is proportional to the common-mode voltage and that the electrostatic coupling factor is constant and approximately $-40\,\mathrm{dB}$ was observed by other authors before, e.g. [24]. However, so far it was only observed by measurement or EM simulation. The novelty of this work is, that the same number was analytically derived. This eventually gives a tangible proof and moreover enables further theoretical approximations on the impact of harness parameters on near-field coupling.
Third, for an (IC) designer, the exact value of the radiation factor is of secondary importance. Accurate (transistor level) simulations are performed late during the product development phase. The knowledge of this factor will help most during the early architecture or concept phase.

In Chapter 4 other radiation mechanisms were taken into account to generate a circuit level model that covers the complete CISPR frequency band B up to $30\,\mathrm{MHz}$. Because of the aforementioned problem of finding *the* correct ALSE test result, the intention of the presented model is rather to educate the circuit designer in how the DUT output might propagate to the receiver, rather than providing a precise prediction of the RE test result. It is critical to understand for a component supplier why different system manufacturers may obtain different ALSE test results although the use the same (IC) product within their systems.
The developed circuit model was validated by comparison of measurement and 3D simulation results published by other authors. Generally, it is not suited to precisely predict or explain ALSE test results. However, it helps to give answer to research questions 2 and 3: Above $3\,\mathrm{MHz}$ - or in other words - as soon as RE is not influenced by direct capacitive coupling alone, forecasting test results with certainty of as roughly as $\pm 6\,\mathrm{dB}$ already needs detailed knowledge of the ALSE where the EMC test will be conducted.

Being able to simulate the transmission factor from DUT output to EMI receiver input does

not already mean that one could predict measurement results. The circuit designer needs to be aware of the significant differences between the spectral appearance of narrowband (NB) and broadband (BB) disturbances when measured with an EMI receiver as well as the used detector types. Only in case of NB signals a straight-forward DFT can yield a spectral outline that visualizes the EMI PK values. Though, most real signals are a mixture of NB and BB components and it might not be able to distinguish which is dominating the emission spectrum. Consequently, to enable useful correlation of simulation data to EMI measurement results, a mandatory part to complete the simulation tool is a model for the EMI receiver which displays the emission spectrum in the frequency domain. The principle is state of the art, but in Chapter 5 two approaches were presented which help to reduce the time needed for the transient circuit level simulation, especially for data transmitting devices. The corresponding original works were published by the author in [73, 76].
Due to long idle times in between data packages (or, generally speaking, low repetition rate of disturbances) the EMI receiver's QP and AVG detector readings can significantly differ from the PK detector result. But the QP detector reading is far more complex and time-consuming to predict. To overcome this issue, a novel QP post-processing technique by interpolation of spectral chunks from parts of the time domain transmission was presented. With its application, research question 4 can be answered to: Long transient data streams with repetitive parts do not need to be simulated completely. Therewith transient simulation time can be decreased significantly and EMC analysis of the overall test protocol becomes feasible.
More than that, by use of the presented correction factor for the well known Fourier envelope of a trapezoidal pulse train, the PK level of BB interferences produced by seldom transmitted data packages can be estimated without simulation at all. This can be a very helpful tool to minimize emissions by right scheduling of data communications.

All in all, this work investigated the practicability and limitations of system-level ALSE RE prediction by component-level simulation. If the cable harness is the sole source of radiation and with a basic knowledge of the overall system, the EMC test result can be predicted with an uncertainty of $6\,\mathrm{dB}$ for frequencies below $3\,\mathrm{MHz}$ and roughly estimated up to $30\,\mathrm{MHz}$. Keeping setup variations and the vast impact of the anechoic chamber itself in mind, a component supplier should be very careful to predict RE results to its costumers. Nonetheless, the presented approach can be a powerful tool to evaluate relative changes in RE due to design iterations, also with respect to the different emission spectra of varying output data streams.
It is the author's opinion that awareness of (system level) EMI root causes and modes of propagation as well as the provision of rules of thumb is more helpful for IC designers than precise but resource-hungry simulation capabilities.

Appendix A.

List of Publications

A.1. Peer-Reviewed Conference Papers

Simulation of Radiated Emission During the Design Phase Based on Scattering Parameter Measurement

Herbert Hackl, Gunter Winkler, and Bernd Deutschmann

Published in: Proceedings of the 10th International Workshop on the Electromagnetic Compatibility of Integrated Circuits (EMC Compo), IEEE

Date of Conference: 10-13 November 2015

Conference Location: Edinburgh, UK

(full paper)

Abstract
There are a number of approaches to predict radiated emissions of automotive components as defined in the CISPR25 standard. However, it can be concluded that none of them are suitable for continuous use by the circuit designer itself because they either need a manufactured prototype and a lab engineer, or lots of simulation time and resources. The designer is normally no EMC expert and does not want to deal with additional, complex simulation tools. This paper presents the generation and use of a simulation model based on S-parameter measurement which can easily be implemented in the design environment (e.g. Cadence Virtuoso) used by the designer and does not notably increase the simulation time. The transient data is post-processed with a Matlab script emulating an EMI test receiver.

Related Chapter(s): 2, 4

Calculation of Very Near Field Radiated Emission of a Straight Cable Harness

Herbert Hackl and Bernhard Auinger

Published in: Proceedings of the 12th Conference on Ph.D. Research in Microelectronics and Electronics (PRIME), IEEE

Date of Conference: 27-30 June 2016

Conference Location: Lisbon, Portugal

(full paper, oral presentation)

Abstract
Radiated emissions generated by an integrated circuit (IC) during operation must not exceed specific limits. For automotive ICs this is verified by the standardized ALSE (Absorber Lined Shielded Enclosure) measurement setup defined in the CISPR 25 standard. This test especially targets the E-field emitted by a long cable harness attached to the device under test. Apart from simulations, analytical calculation models can be applied to quickly estimate the compliance test results. Typically the Hertzian dipole antenna model is used to calculate the electric field radiating from cables. But during the ALSE test radiated emissions from 150 kHz to 1 GHz are measured in 1 m distance. This results in very near field conditions for the lower frequencies, where the common prediction model is at its theoretical limits. As an alternative this paper demonstrates an electrostatic approach. For the frequency range of 100 kHz to 30 MHz constant transmission factors are derived which yield the radiated emission spectrum when applied to the IC's output signal spectrum. The results of both calculation models are compared to measurement data.

Related Chapter(s): 3

An EMI Receiver Model to Minimize Simulation Time of Long Data Transmissions

Herbert Hackl and Bernd Deutschmann

Published in: Proceedings of the 2016 Austrochip Workshop on Microelectronics (Austrochip), IEEE

Date of Conference: 19 October 2016

Conference Location: Villach, Austria

(full paper, oral presentation)

Abstract
For evaluating the electromagnetic emission (EME) of an integrated circuit (IC) during the design phase, a precise transient simulation of the disturbing signal is required. This usually takes a lot of time, so that simulating a signal trace longer than a couple of ms is not feasible. In this paper an extension to an existing electromagnetic interference (EMI) receiver model is introduced, which enables to interpolate the emission spectrum of very long transient data with repetitive contents (like digital data transmissions) while using only short parts of the overall signal as input. Therewith the IC simulation time can be reduced by far without losing accuracy in the EME post-processing stage.

Related Chapter(s): 5

Computing the Electromagnetic Emission Spectrum of Pulses by Convolution in Frequency Domain

Herbert Hackl and Bernd Deutschmann

Published in: Proceedings of the 2017 International Symposium on Electromagnetic Compatibility (EMC EUROPE), IEEE

Date of Conference: 4-7 September 2017

Conference Location: Angers, France

(full paper, oral presentation)

Abstract
To simulate the electromagnetic emission of an electronic system, also the behavior of the measurement instrument, an Electromagnetic Interference (EMI) receiver, needs to be emulated. This requires not only computation capability, but also the processing time is proportional to the length of the time domain input signal. As an alternative, this work investigates the usability of a convolution in frequency domain. Based on this approach a correction factor is derived to obtain the PK detector reading for broadband disturbers directly from the result of an ordinary Fourier transformation. The pulse weighting characteristic of the other detectors is used to gain the corresponding QP and AVG reading. The solution is demonstrated on the example of a pulse train signal and the application of a data transmitter IC.

Related Chapter(s): 5

Survey on Integrated High-Power Low-Emission Output Stages for Drivers of Low-Frequency Resonant Loads

Herbert Hackl, Mario Auer and Ricardo Eckert

Published in: Proceedings of the 2017 Austrochip Workshop on Microelectronics (Austrochip), IEEE

Date of Conference: 12 October 2017

Conference Location: Linz, Austria

(full paper, oral presentation)

Abstract
To drive low-frequency resonant loads with high output power and low emission, Class-AB push-pull stages are state of the art. But their theoretically superior emission performance is often sacrificed for efficiency. A differential Class-D concept is a promising alternative, because it can combine both excellent power efficiency and low missions. This work is a survey on the main sources of distortions for both amplifier topologies with basic considerations to internal power losses and efficiency. The investigations are based on simple circuits and compared to measurement results of two integrated circuits.

Related Chapter(s): -

The Shielding Effect of a Multi-Cable Harness as Function of IC Output Termination Impedance

Herbert Hackl, Bernhard Auinger, Bernd Deutschmann and Anna Gheonjian

Published in: 2018 Joint IEEE International Symposium on Electromagnetic Compatibility & Asia-Pacific Symposium on Electromagnetic Compatibility (2018 Joint IEEE EMC & APEMC), IEEE

Date of Conference: 14-18 May 2018

Conference Location: Singapore, Singapore

(full paper)

Abstract
Integrated circuits for automotive applications must not violate certain limits for maximum electromagnetic emissions. One of many standardized compliance tests is the CISPR 25 ALSE test, where the radiated emission from a straight cable harness attached to a device is evaluated. For devices with multiple outputs this harness may contain multiple cables. It is critical to understand, that non-operated cables have a certain shielding effect, which is a function of their termination impedance. The radiated emission originating from a harness consisting of multiple cables will, in some cases, be drastically lower than that of a single wire. By applying fundamental electrostatic relations this paper demonstrates how to estimate the deviation by simple calculations. The analytical results are compared to measurements and 3D EM simulation.

Related Chapter(s): 3

A.2. Poster

Towards a New Measurement Standard to Evaluate the Audibility of In-Vehicle Interferences

Herbert Hackl

Published in: OVE-Schriftenreihe Band 87, 15. EMV Fachtagung

Date of Conference: 26-27 April 2017

Conference Location: Graz, Austria

Abstract
Numerous legal EMC regulations and measurement standards ensure that devices do not interfere other's functionality or even cause harm to humans. However, no emission limit tells what is finally obvious for the automotive customer: Do I hear the operation of a device in my car's radio? This is an especially important question for the AM radio band (530 kHz - 1.8 MHz) where systems operating at around 100 kHz might interfere, such as Wireless Power Charging (WLPC) or Passive Keyless Entry (PKE). Today, car radio audibility tests are conducted by the car manufacturer late in the design process with complete system prototypes. In this poster sources of audibility are investigated and an objective and reproducible component-level measurement setup is proposed.

Related Chapter(s): -

Bibliography

[1] CISPR 25 Ed.4, *Vehicles, boats and internal combustion engines - Radio disturbance characteristics - Limits and methods of measurement for the protection of on-board receivers*, I.E.Comission Std., November 2016.

[2] IEC 61967, *Integrated Circuits - Measurement of Electromagnetic Emissions, 150 kHz to 1 GHz, various Parts*, I.E.Comission Std., 2002.

[3] C. Panchal, S. Stegen, and J. Lu, "Review of static and dynamic wireless electric vehicle charging system," *Engineering Science and Technology, an International Journal*, vol. 21, no. 5, pp. 922 – 937, 2018.

[4] Microchip Technology Inc. (2014) ATA5279/ATA5279C datasheet. Accessed March 2019. [Online]. Available: www.microchip.com/wwwproducts/en/ATA5279C

[5] Texas Instruments Incorporated. (2010) TMS3705 Transponder Base Station IC datasheet (Rev. E) datasheet. Accessed March 2019. [Online]. Available: www.ti.com/product/TMS3705

[6] MIL-STD-461F, *Requirement of the Control of Electromagnetic Interference Characteristics of Subsystems and Equipment*, US DoD Std., December 2007.

[7] Z. Chen and S. Frei, "Near-field measurement based prediction of antenna test results below 30 MHz in CISPR 25 setups," in *2016 International Symposium on Electromagnetic Compatibility - EMC EUROPE*, Sept 2016, pp. 17–22.

[8] D. Schneider, M. Beltle, M. Siegel, S. Tenbohlen, and W. Köhler, "Radiated emissions of an electric drive system estimated on a bench using disturbance currents and transfer functions," *IEEE Transactions on Electromagnetic Compatibility*, vol. 57, no. 3, June 2015.

[9] J. Jia, D. Rinas, and S. Frei, "An alternative method for measurement of radiated emissions according to CISPR 25," in *Electromagnetic Compatibility (EMC EUROPE), 2013 International Symposium on*, Sept 2013, pp. 304–309.

[10] H. Rebholz and S. Tenbohlen, "A fast radiated emission model for arbitrary cable harness configurations based on measurements and simulations," in *Electromagnetic Compatibility, 2008. EMC 2008. IEEE International Symposium on*, Aug 2008, pp. 1–5.

[11] A. Radchenko, V. V. Khilkevich, N. Bondarenko, D. Pommerenke, M. Gonser, J. Hansen, and C. Keller, "Transfer Function Method for Predicting the Emissions in a CISPR-25 Test-Setup," *IEEE Transactions on Electromagnetic Compatibility*, vol. 56, no. 4, Aug 2014.

[12] G. H. Li, W. Qian, A. Radchenko, G. Hess, R. Hoeckele, P. Jalbert, T. V. Doren, D. Pommerenke, and D. Beetner, "Estimating the radiated emissions from cables attached to a switching power supply in a MIL-STD 461 test," in *2013 IEEE International Symposium on Electromagnetic Compatibility*, Aug 2013.

[13] G. Ergaver and J. Trontelj, “Prediction of Radiated Emissions of Automotive Electronics Early in the Design Phase based on Automotive Component Level Testing,” *Informacije MIDEM Journal of Microelectronics, Electronic Components and Materials*, vol. 46, no. 1, pp. 42–52, 2016. [Online]. Available: http://ojs.midem-drustvo.si/index.php/InfMIDEM/article/view/191

[14] Z. Desheng, C. W. Hoe, and L. C. Kin, “Modeling of radiated electromagnetic emission coming from interface cables of an equipment,” in *Electromagnetic Compatibility, 1996. Symposium Record. IEEE 1996 International Symposium on*, Aug 1996, pp. 230–234.

[15] J. Wang, O. Fujiwara, and K. Sasabe, “A simple method for predicting common-mode radiation from a cable attached to a conducting enclosure,” in *Microwave Conference, 2001. APMC 2001. 2001 Asia-Pacific*, vol. 3, 2001, pp. 1119–1122 vol.3.

[16] J. Jia, F.Kremer, and S.Frei, “Modellierung von CISPR-25 Antennenmessung mittels schneller approximierender Berechnungsverfahren,” in *emv 2012 - Elektromagnetische Verträglichkeit*, Messe Düsseldorf, Feb 2012, pp. 255–262.

[17] C. Ueda, “Low frequency emission simulation using 3D electromagnetic solver based on CISPR25,” in *Antennas and Propagation (ISAP), 2012 International Symposium on*, Oct 2012, pp. 704–707.

[18] T. Uno, K. Maeda, T. Tanaka, Y. Okuda, and O. Wada, “A Study on Characteristics of 10 MHz to 30 MHz in CISPR 25 ALSE Method,” in *2018 Joint IEEE International Symposium on Electromagnetic Compatibility & Asia-Pacific Symposium on Electromagnetic Compatibility (APEMC 2018)*, May 2018.

[19] H. Hackl, G. Winkler, and B. Deutschmann, “Simulation of radiated emission during the design phase based on scattering parameter measurement,” in *Electromagnetic Compatibility of Integrated Circuits (EMC Compo), 2015 10th International Workshop on the*, Nov 2015, pp. 228–231.

[20] L. Dawson and A. C. Marvin, “New screened room techniques for the measurement of RFI,” *Electronic and Radio Engineers, Journal of the Institution of*, vol. 58, no. 1, pp. 28–32, January 1988.

[21] F. Lafon, R. Dupendant, and J. Davalan, “Investigation on dispersions between CISPR25 chambers for radiated emissions below 100 MHz,” in *2014 International Symposium on Electromagnetic Compatibility*, Sept 2014, pp. 29–34.

[22] C. Carobbi, “A Lumped Model of the Rod Antenna Measurement Setup for Automotive and Military Testing,” in *2018 Joint IEEE International Symposium on Electromagnetic Compatibility & Asia-Pacific Symposium on Electromagnetic Compatibility (APEMC 2018)*, May 2018, pp. 57–62.

[23] F. Lafon, J. Davalan, and R. Dupendant, "Inter-laboratory comparison between CISPR25 chambers, identification of influent parameters and analysis by 3D simulation," in *2015 Asia-Pacific Symposium on Electromagnetic Compatibility (APEMC)*, May 2015, pp. 71–74.

[24] L. Turnbull, "The groundplane resonance - problems with radiated emissions measurements below 30 MHz," in *Automotive EMC conference*, 2007. [Online]. Available: www.chan-gen.com:86/specs/below30.pdf

[25] F. Lafon, R. Dupendant, J. Davalan, and C. Chevriau, "Identification and Study of Influential Parameters in CISPR25 Radiated Emissions Test Setup by Interlaboratory Measurements and 3-D Simulation Combined Analysis," *IEEE Transactions on Electromagnetic Compatibility*, vol. 58, no. 5, pp. 1398–1406, Oct 2016.

[26] F. J. Bongartz, J. Deckers, M. Heina, H. Hirsch, J. Mooser, J. C. Nickel, and M. Seiger, "Proposal for the validation of absorber lined shielded enclosures for CISPR 25 emission tests," in *2009 IEEE International Symposium on Electromagnetic Compatibility*, Aug 2009, pp. 116–120.

[27] J. Jia, "Current scan methods to predict radiated emissions of automotive components according to CISPR 25," Ph.D. dissertation, TU Dortmund University, 2015.

[28] C. W. Fanning, "Improving monopole radiated emission measurement accuracy; RF chamber influences, antenna height and counterpoise grounding (CISPR 25 & MIL-STD-461E vs MIL-STD-461F)," in *2009 IEEE International Symposium on Electromagnetic Compatibility*, Aug 2009, pp. 103–18.

[29] D. D. Swanson, "Analysis of MIL-STD-461E and MIL-STD-461F RE102 Test setup configurations below 100 MHz," in *2008 IEEE International Symposium on Electromagnetic Compatibility*, Aug 2008, pp. 1–11.

[30] A. C. Marvin and S. Goodwin, "Field coupling to antennas in screened enclosures," in *IEE Colloquium on Calibration of Antennas for Close Range Measurements*, Jan 1990.

[31] S. Goodwin and A. C. Marvin, "An analysis of the effects of cable layout on cable to antenna coupling inside a screened room," *IEEE Transactions on Electromagnetic Compatibility*, vol. 33, no. 3, pp. 163–171, Aug 1991.

[32] MIL-STD-461G, *Requirement of the Control of Electromagnetic Interference Characteristics of Subsystems and Equipment*, US DoD Std., December 2015.

[33] A. Gandolfo, R. Azaro, and D. Festa, "Improving the accuracy of radiated emission measurements for frequency below 30 MHz by using a fiber optic isolated rod antenna," in *2017 IEEE International Symposium on Electromagnetic Compatibility Signal/Power Integrity (EMCSI)*, Aug 2017, pp. 63–68.

[34] C. F. M. Carobbi and D. Izzo, "Evaluation and Improvement of the Reproducibility of CISPR 25 ALSE Test Method," *IEEE Transactions on Electromagnetic Compatibility*, vol. 60, no. 4, pp. 1069–1077, Aug 2018.

[35] M. Zingarelli and R. Grego, "9 kHz - 30 MHz E-field Measurement by an Innovative ROD antenna embedding a Fully CISPR 16-1-1 receiver," in *2016 Asia-Pacific International Symposium on Electromagnetic Compatibility (APEMC)*, vol. 01, May 2016, pp. 788–790.

[36] narda Safety Test Solutions. (2017) FR-4003 - FFT Full compliance field receiver 9 kHz - 30 MHz. [Online]. Available: www.narda-sts.it/eng/products/receivers/fr4003

[37] cst.com. (2014) Airbus Defence and Space analyzes EMC test chamber using CST Studio Suite. [Online]. Available: www.cst.com

[38] C. R. Paul, "A comparison of the contributions of common-mode and differential-mode currents in radiated emissions," *Electromagnetic Compatibility, IEEE Transactions on*, vol. 31, no. 2, pp. 189–193, May 1989.

[39] H. Hackl and B. Auinger, "Calculation of very near field radiated emission of a straight cable harness," in *2016 12th Conference on Ph.D. Research in Microelectronics and Electronics (PRIME)*, June 2016, pp. 1–4.

[40] J. Jia, D. Rinas, and S. Frei, "Prediction of radiated fields from cable bundles based on current distribution measurements," in *International Symposium on Electromagnetic Compatibility - EMC EUROPE*, Sept 2012, pp. 1–7.

[41] Z. Chen, A. Zeichner, and S. Frei, "Grenzen des stromscan-basierten dipolmodells und erweiterung mit einem quasistatischen ansatz," in *EMV Düsseldorf: Internationale Fachmesse und Kongress für Elektromagnetische Verträglichkeit*, Feb 2018, pp. 537–546.

[42] S. Frei, R. G. Jobava, D. Karkashadze, A. Gheonjian, and E. Yavolovskaya, "Calculation of low frequency EMC problems in large systems with a quasi-static approach," in *2004 International Symposium on Electromagnetic Compatibility (IEEE Cat. No.04CH37559)*, vol. 3, Aug 2004, pp. 798–803 vol.3.

[43] S. Frei, T. Naegel, and R. Jobava, "Bestimmung der Störaussendung im KFZ durch die getrennte Betrachtung der elektrischen und magnetischen Verkopplungen," in *12. Internationale Fachmesse und Kongress für Elektromagnetische Verträglichkeit*, K. Feser, Ed., 2004.

[44] C. Paul, *Analysis of Multiconductor Transmission Lines*, ser. Wiley - IEEE. Wiley, 2008.

[45] C. Poudroux, M. Rifi, and B. Demoulin, "A simplified approach to determine the amplitude of the transient voltage induced on a cable bundle," *IEEE Transactions on Electromagnetic Compatibility*, vol. 37, no. 4, pp. 497–504, Nov 1995.

[46] X. Jun and L. Yinghua, "Analysis of radiated emissions from multiconductor lines," in *2008 8th International Symposium on Antennas, Propagation and EM Theory*, Nov 2008, pp. 1009–1012.

[47] J. Wang, X. Song, D. Su, and B. Li, "Near-field radiation calculation of irregular wiring twisted-wire pairs based on mode decomposition," *IEEE Transactions on Electromagnetic Compatibility*, vol. 59, no. 2, pp. 600–608, April 2017.

[48] G. Andrieu, X. Bunlon, L. Koné, J.-P. Parmantier, B. Démoulin, and A. Reineixl, *The 'Equivalent Cable Bundle Method': an Efficient Multiconductor Reduction Technique to Model Industrial Cable Networks*. InTechOpen, 2011. [Online]. Available: http://cdn.intechweb.org/pdfs/13357.pdf

[49] P. Russer, "EMC Measurements in the Time-Domain," in *Proceedings of the XXXth URSI General Assembly in Istanbul*, Munich, Germany, 2011.

[50] "Spectrum Analysis Basics," Keysight Technologies Inc., Application Note, 2014.

[51] M. Keller, "Comparison of Time Domain Scans and Stepped Frequency Scans in EMI Test Receivers," Rohde&Schwarz, Whitepaper, 2013.

[52] "The EMI-Receiver according to CISPR 16-1-1," Schwarzbeck Mess-Elektronik, Application Note, 2016.

[53] CISPR 16-1-1 Ed.1, *Specification for radio disturbance and immunity measuring apparatus and methods*, I.E.Comission Std., 2003.

[54] T. Karaca, B. Deutschmann, and G. Winkler, "EMI-Receiver Simulation Model with Quasi-Peak Detector," in *Joint IEEE International Symposium on Electromagnetic Compatibility and EMC Europe*, Dresden, Germany, Aug. 2015.

[55] K. Hörmaier, H. Zangl, and H. Zojer, "An EMI receiver model to evaluate electromagnetic emissions by simulation," in *IEEE International Instrumentation and Measurement Technology Conference (I2MTC 2012)*, Graz, Austria, May 2012, pp. 2558–2562.

[56] C. Li, L. Zhang, T. Dong, T. Wang, and H. Chen, "An EMI Receiver Model with Consideration of the Intermediate Frequency Filter," in *Proc. Asia-Pacific International Symposium on Electromagnetic Compatibility (APEMC'16)*, May 2016, pp. 233–236.

[57] F. Krug and P. Russer, "Quasi-peak detector model for a time-domain measurement system," *IEEE Transactions on Electromagnetic Compatibility*, vol. 47, no. 2, pp. 320–326, May 2005.

[58] H. Hackl, B. Auinger, B. Deutschmann, and A.Gheonjian, "The Shielding Effect of a Multi-Cable Harness as Function of IC Output Termination Impedance," in *2018 Joint IEEE International Symposium on Electromagnetic Compatibility & Asia-Pacific Symposium on Electromagnetic Compatibility (APEMC 2018)*, May 2018, pp. 707–712.

[59] E. Philippow and K. Bonfig, *Grundlagen der Elektrotechnik*. Verlag Technik, 2000.

[60] A. Inan, S. Umran, and R. Said, *Electromagnetic Engineering and Waves: Global Edition*. Pearson Education Limited, 2015.

[61] J. Kraus and D. Fleisch, *Electromagnetics With Applications*, ser. McGraw-Hill series in electrical and computer engineering. WCB/McGraw-Hill, 1999.

[62] R. J. Spiegel, C. A. Booth, and E. L. Bronaugh, "A radiation measuring system with potential automotive under-hood application," *IEEE Transactions on Electromagnetic Compatibility*, vol. EMC-25, no. 2, pp. 61–69, May 1983.

[63] B. Li, D. Su, J. Wang, and X. Song, "Common- and Differential-Mode Conversion Induced by Asymmetry and Dielectric Coating in a Transmission Line System," *IEEE Transactions on Electromagnetic Compatibility*, vol. 59, no. 3, pp. 988–991, June 2017.

[64] Tera Analysis Ltd. QuickField. [Online]. Available: www.quickfield.com

[65] ETS-Lindgren L.P., *Model 3301B Active Rod & Field Antenna, Manual*, 2003.

[66] Mayo Foundation. (2004) Transmission Line Electromagnetic Modeling Tool Suite (TNT 1.2.2). [Online]. Available: mmtl.sourceforge.net

[67] P. Kay, "EMC test site validations for 1m automotive and military emissions tests," in *2011 Electromagnetic Compatibility Symposium - Perth*, Nov 2011, pp. 1–6.

[68] A. C. Marvin and L. Steele, "Improved techniques for the measurement of radiated emissions inside a screened room," *Electronics Letters*, vol. 22, no. 2, pp. 94–96, January 1986.

[69] B. Smith and M. Carpentier, *Microwave Engineering Handbook Volume 1: Microwave Components*, ser. Microwave and RF Techniques and Applications. Springer US, 1992.

[70] R. Garg, P. Bhartia, I. Bahl, and A. Ittipiboon, *Microstrip Antenna Design Handbook*. Artech House, 2001.

[71] F. Lafon, R. Dupendant, and J. Davalan, "Analysis and Discussion Regarding Dispersions in CISPR25 Compliant Faraday Cage," July 2014.

[72] S. Goodwin and A. C. Marvin, "A transmission line model of cable to antenna coupling inside a screened room," *IEEE Transactions on Electromagnetic Compatibility*, vol. 31, no. 4, pp. 397–404, Nov 1989.

[73] H. Hackl and B. Deutschmann, "Computing the electromagnetic emission spectrum of pulses by convolution in frequency domain," in *2017 International Symposium on Electromagnetic Compatibility - EMC EUROPE*, Sept 2017, pp. 1–6.

[74] C. Rauscher, V. Janssen, and R. Minihold, *Fundamentals of Spectrum Analysis*. Rohde & Schwarz, 2007.

[75] C. Keller and K. Feser, "A new method of emission measurement," in *2002 IEEE International Symposium on Electromagnetic Compatibility*, vol. 2, Aug 2002, pp. 599–604.

[76] H. Hackl and B. Deutschmann, "An EMI Receiver Model to Minimize Simulation Time of Long Data Transmissions," in *2016 Austrochip Workshop on Microelectronics (Austrochip)*, Oct 2016, pp. 57–62.

[77] B. Deutschmann, R. Illing, and B. Auer, "Edge shaping to reduce the electromagnetic emissions," in *10th International Symposium on Electromagnetic Compatibility*, Sept 2011, pp. 742–745.

[78] M. Mardiguian, *Controlling Radiated Emissions by Design*, ser. SpringerLink : Bücher. Springer International Publishing, 2014.